

**FABRICATION AND CHARACTERIZATION OF HEAT  
FLUX SENSOR USING POLYMER DERIVED CERAMICS**

---

A Dissertation  
Presented to  
The Faculty of the Graduate School  
University of Missouri

---

In Partial Fulfillment  
Of the Requirements for the Degree  
Doctor of Philosophy  
In Mechanical and Aerospace Engineering

---

By

SUNGHOON JUNG

Dr. Frank Z. Feng, Dr. Jinn-Keun Chen, Dissertation Supervisors

December 2011

The undersigned, appointed by the Dean of the Graduate School, have examined the dissertation entitled

**FABRICATION AND CHARACTERIZATION OF HEAT  
FLUX SENSOR USING POLYMER DERIVED CERAMICS**

Presented by SUNGHOON JUNG

A candidate for the degree of Doctor of Philosophy

And hereby certify that in their opinion it is worthy of acceptance

---

Professor Dr. Frank Feng, Dissertation Supervisor

---

Professor Dr. Jinn-Kuen Chen, Dissertation Supervisor

---

Professor Dr. Robert Tzou

---

Professor Dr. Yuwen Zhang

---

Professor Dr. Tushar Ghosh

## ACKNOWLEDGEMENTS

With all my heart, I would like to express big appreciation to my advisors, Dr. Frank Feng and Dr. JK Chen. Throughout our project, they have been supporting me with generosity, patience and kind encouragement. In spite of difficulties encountered, their patience and encouragement were crucial for me to finish my PhD degree successfully.

I am grateful to Dr. Hao Li and his students for their cooperation regarding laboratory sharing. Most of my experiment results are obtained from the equipments in his laboratory. Without his allowing me to use them, our work would have been tougher than it was. I also thank Dr. Lombardo for the journal paper work and technician Richard for his help on my experiment setup.

Also I would like to say “thank you” to my committee members, Dr. Robert Tzou, Dr. Yuwen Zhang, Dr. Tushar Ghosh for their valuable time and efforts as well as their warm advices during dissertation defense. There are special thanks to Dr. Duckbong Seo for his help and good friendship with me as a PostDoc throughout this research.

The biggest appreciation goes to my parents, wife and lovely kids, Sunjae and Yunseo. I really appreciate my wife, Miran for her patience, sacrifice and praying for me. Especially I would like to devote my achievement here to my father who passed away last year. His faith and confidence toward me always made me awakened and go further.

This work is funded by the T&E/S&T Program through the U.S. Army Program Executive Office. Their support is gratefully appreciated.

Above all, all of my accomplishment here were from God. I sincerely would like to thank God.

# TABLE OF CONTENTS

<b>ACKNOWLEDGEMENTS .....</b>	<b>ii</b>
<b>LIST OF FIGURES.....</b>	<b>vii</b>
<b>LIST OF TABLES.....</b>	<b>xiii</b>
<b>ABSTRACT.....</b>	<b>xiv</b>
<b>Chapter 1 INTRODUCTION.....</b>	<b>1</b>
1.1 Ceramic MEMS .....	3
1.1.1. Drawbacks of conventional ceramics for high temperature MEMS.....	4
1.1.2. Polymer Derived Ceramic (PDC) .....	5
1.2. Polymer Derived SiCN .....	9
1.2.1. Advantages of using PDC SiCN for high temperature MEMS .....	11
1.2.2. Fabrication techniques of PDC SiCN .....	12
1.3. Electrical conductivity of amorphous SiCN .....	16
1.4. Heat Flux Sensor (HFS) using SiCN MEMS .....	17
1.5. Literature reviews .....	20
1.5.1. Fabrication of SiCN .....	20
1.5.2. Electrical property of SiCN .....	22
1.5.3. Heat flux sensor and temperature sensor using ceramics .....	23
1.6. Objectives .....	24

## **Chapter 2 FABRICATION OF FREE STANDING PDC SiCNs.....26**

2.1.	Introduction.....	26
2.1.1.	Problems in conventional photo-polymerization .....	27
2.2.	Free-standing PDC SiCNs Fabrication process .....	29
2.2.1.	Precursor preparation .....	29
2.2.2.	A novel direct contact lithography technique for patterning .....	30
2.2.3.	Heat treatments for SiCN structures .....	38
2.3.	Result and conclusions.....	42

## **Chapter 3 CHARACTERIZATION OF PDC SiCN MATERIAL ....44**

3.1.	Introduction.....	44
3.2.	Characterization of SiCN.....	45
3.2.1.	XRD analysis of SiCN .....	45
3.2.2.	Oxidation Test of SiCN .....	47
3.2.3.	Composition analysis by SEM/EDS .....	49
3.2.4.	Depth dependence of composition of PDC SiCN.....	52
3.3.	Electrical resistance of amorphous PDC SiCN.....	54
3.3.1.	Measurement setup of free standing SiCN .....	55
3.3.2.	Analysis on resistance difference between surface and bulk.....	57
3.3.3.	Effect of annealing temperature on electric resistance .....	59
3.4.	RTD Curve.....	61
3.5.	Conclusion .....	65

**Chapter 4 FABRICATION OF PDC RTD ON A SUBSTRATE .....67**

4.1. Introduction..... 67

4.2. Finding filler material ..... 69

    4.2.1. Precursor preparation ..... 69

    4.2.2. Analysis of shrinkage rate..... 72

4.3. Fabrication of a PDC RTD sensor array on quartz wafer ..... 74

    4.3.1. Screen printing technique ..... 74

    4.3.2. Fabrication of a PDC RTD array using cut-out plastic sticker ..... 75

4.4. Patterning electrode for electric connection ..... 81

4.5. Measurement of Resistance with varying temperature ..... 82

    4.5.1. Measurement of PDC RTD with Al filler..... 82

    4.5.2. Measurement of PDC RTD with TiB<sub>2</sub> filler ..... 88

4.6. Characterization of PDC RTDs with filler material ..... 90

    4.6.1. Characterization of Al filled RTD ..... 90

    4.6.2. Characterization of TiB<sub>2</sub> filled RTD..... 95

4.7. Summary and conclusion..... 98

**Chapter 5 FABRICATION AND MEASUREMENT OF HEAT FLUX  
SENSOR (HFS) .....100**

5.1. Introduction..... 100

5.2. HFS made of free standing SiCN PDC..... 100

    5.2.1. DAQ configuration for Heat Flux measurement ..... 102

5.2.2.	Measurement result.....	103
5.3.	HFS made of filler used PDC RTDs.....	104
5.3.1.	DAQ configuration for HFS array .....	105
5.3.2.	Measurement of output voltage of 4 HFSs .....	109
5.3.3.	Measurement of Temperature and Heat Flux of 4 HFSs .....	112
5.4.	Summary and Conclusion .....	121
<b>Chapter 6 DISCUSSION AND FUTURE WORK.....</b>		<b>122</b>
6.1.	Discussions .....	122
6.1.1.	Electric connections .....	122
6.1.2.	DAQ configuration for high resistance RTDs .....	124
6.2.	Future works .....	125
<b>REFERENCES .....</b>		<b>128</b>
<b>VITA .....</b>		<b>134</b>

# LIST OF FIGURES

<b>Figure</b>	<b>Page</b>
Figure 1.1 General sintering process from powder based ceramic material.....	5
Figure 1.2 Examples of Si based preceramic polymers (Source: Colombo et al. [3]).....	6
Figure 1.3 Chemical formation route of PDC.....	7
Figure 1.4 Applications of PDCs ; a) MEMS Ratchet, b) PDC coating, c) PDC micro fibers, d) PDC-metal composites .....	8
Figure 1.5 Applications of PDC SiCN; a) SiCN electrostatic actuator, b) SiCN micro gripper, c) Micro gear .....	11
Figure 1.6 Two major fabrication techniques for SiCN (Source: Liew et al [1]).....	12
Figure 1.7 General Micro-Casting process for PDC SiCN ; (a) the photoresist is spun onto a substrate; (b) UV-lithography, producing desired shapes; (c) liquid precursor; thermal setting; solidification; (d) polish off the top layer on the wafer; (e) cross-linking under isostatic pressure; (f) pyrolysis; photoresist decomposes; SiCN part forms .....	13
Figure 1.8 General fabrication process of Photo-Polymerization ; (a) spin precursor onto substrate; (b) UV exposure through a mask; (c) solidified polymer with remaining liquid; (d) remove remaining liquid; (e) remove polymer structures from substrate; (f) crosslink and pyrolysis to obtain SiCN .....	14
Figure 1.9 Other techniques for PDC SiCN fabrication; (a) MIMIC, (b) Imprinting, (c) stereolithography techniques (Source: Lee et al [30]) .....	15

Figure 2.1 Conventional photo-polymerization method.....	27
Figure 2.2 Schematic of pore wall definition by UV dispersion and diffraction .....	28
Figure 2.3 (a) Polymer (Polyureasilazane) and Photo initiator and (b) UV exposure box .....	29
Figure 2.4 The schematic of the direct contact fabrication process.....	31
Figure 2.5 The schematic of direct contact fabrication process using Teflon film; (a) place transparent Teflon film on the patterned mask; (b) apply liquid precursor drops on the transparent Teflon film; (c) apply UV exposure from bottom of patterned mask; (d) etch out the unexposed area by acetone; (e) perform UV cure from top to solidify upper part of patterns; (f) remove the patterned structures from Teflon film.....	32
Figure 2.6 Completed polymer patterns of precursor on the glass substrate .....	33
Figure 2.7 Removing precursor patterns using a razor blade; (a) without additional UV- exposure (b) with additional UV-exposure.....	35
Figure 2.8 Comparison of fabrication process of non-contact lithography and novel contact lithography.....	36
Figure 2.9 Thickness of the precursor patterns as a function of UV exposure time .....	37
Figure 2.10 Gas Tube Furnace for heat treatment (a) and Mass flow controller (b).....	39
Figure 2.11 Heat treatment processes .....	40
Figure 2.12 Effect of the state of solidity before heat treatment .....	41
Figure 2.13 Completed free standing SiCNs .....	42
Figure 3.1 XRD patterns of polyureasilazane pyrolyzed to: (A) 1200°C, (B) 1300°C, (C) 1400°C, (D) 1500°C, (E) 1600°C under Nitrogen	46

Figure 3.2 XRD patterns of RTDs annealed at 1200 °C, 1300 °C, and 1400 °C for 25 hours respectively .....	47
Figure 3.3 SEM image showing the location points used for EDS analysis.....	48
Figure 3.4 Composition of RTDs by EDS after annealing and after oxidation.....	49
Figure 3.5 SEM images of RTD (a) surface and (b) bulk.....	50
Figure 3.6 The result of EDS analysis for the two targeted points; (a) surface (target #1 and (b) bulk (target #2) .....	51
Figure 3.7 Plots from EDS Linescaning over cross-section of samples .....	53
Figure 3.8 Electrical conductivity of amorphous SiCN depending on annealing time and temperature (Source : Haluschka et al [16]) .....	54
Figure 3.9 The process and picture of making electric connection .....	56
Figure 3.10 The system for measuring electrical resistance of SiCN RTD.....	56
Figure 3.11 Resistance difference depending on connection conditions, surface and bulk connections. ....	58
Figure 3.12 Resistance vs. Temperature for three different RTDs; (a) 1200°C, (b) 1300°C, (c) 1400°C for annealing temperature. ....	60
Figure 3.13 In one plot after taking log for resistance .....	61
Figure 3.14 Typical curve of Steinhart-Hart equation .....	62
Figure 3.15 Steinhart-hart coefficients of three types of SiCN RTD .....	64
Figure 4.1 Pictures of (a) shrinkage rate and (b) failure on substrate	67
Figure 4.2 Process of expansion of filler particle .....	68
Figure 4.3 Comparison of shrinkage rate with different filler materials .....	74
Figure 4.4 Illustration of screen printing technique (Source : Shaheen et al [53]).....	75

Figure 4.5 Designs of RTD array drawn by AutoCAD .....	76
Figure 4.6 Process of printing screen for patterning pre-ceramic precursor on quartz wafer .....	77
Figure 4.7 Array of pre-ceramic precursor on quartz wafer before heat treatment; (a) Al filler precursor, (b) TiB <sub>2</sub> filler precursor.....	78
Figure 4.8 4x4 of filler used PDC RTD on quartz wafer; (a) photo-lithography only, (b) photo-lithography and screen printing .....	79
Figure 4.9 Process of heat treatment.....	80
Figure 4.10 The picture of resulting PDC RTD array on quartz wafer: (a) before, (b) after .....	81
Figure 4.11 Electrode patterning by RF sputtering using the shadow mask method .....	82
Figure 4.12 Three Resistance measurements out of RTD array .....	83
Figure 4.13 Picture of 4 X 4 Al filled PDC RTD array with Au electrode .....	84
Figure 4.14 The output voltages as a functions of temperature in 4 groups.....	86
Figure 4.15 Comparisons of output voltages during heating up and cooling down for temperature between 250 and 290°C .....	87
Figure 4.16 Plot of resistance change of TiB <sub>2</sub> filled PDC with temperature.....	88
Figure 4.17 Comparision of curve smoothness between Al filled and TiB <sub>2</sub> filled RTDs: (a) Al filled RTD (b) TiB <sub>2</sub> filled RTD .....	89
Figure 4.18 EDS result for 8 RTDs in array; (a) before, (b) after heat treatment.....	91
Figure 4.19 SEM images of RTDs' surface (a) 2 X 4mm size (b) 1 X 2 mm size .....	92
Figure 4.20 SEM images of the surface of TiB <sub>2</sub> filled RTDs of 1 X 2 mm size.....	93
Figure 4.21 XRD results of Al filled RTDs pyrolyzed at : (a) 800°C, (b) 1100°C .....	95

Figure 4.22 EDS results on TiB <sub>2</sub> filled RTDs: (a) before and (b) after pyrolyzing.....	96
Figure 4.23 XRD results of TiB <sub>2</sub> filled RTDs: (a) pyrolyzed at 800°C; (b) at 1100°C....	98
Figure 5.1 Process of fabrication of HFS and attaching on coupon.....	101
Figure 5.2 Picture of HFS made by free standing SiCN RTDs .....	101
Figure 5.3 Circuit diagram of Wheatstone bridge for free standing SiCN HFS.....	102
Figure 5.4 Picture of Mounted HFS on sample and wheatstone bridge circuit board ....	103
Figure 5.5 Output voltage measurement result for 4 HFSs .....	104
Figure 5.6 Picture of RTD arrays on two sides of substrate .....	105
Figure 5.7 Pictures of PCB attached with wafers; (a) front, (b) back.....	106
Figure 5.8 Circuit configuration of voltage divider network.....	107
Figure 5.9 Configuration of data acquisition system .....	108
Figure 5.10 (a) Locations of HFSs, (b) After gold electrodes are deposited .....	109
Figure 5.11 Picture of DAQ system for output voltage measurement from RTDs .....	109
Figure 5.12 Output voltage measurement results (a) from top RTDs, (b) from bottom RTDs.....	111
Figure 5.13 Comparison of output voltage of RTDs at HFS locations.....	112
Figure 5.14 The schematic of completed RTD array assembly (a) cross-sectional view with constituents, (b) completed RTD array assembly.....	113
Figure 5.15 Output voltage results of 20 RTDs (a) RTD 1~16 and (b) output voltage results of paired RTDs (1 and 17, 4 and 18, 13 and 18, 16 and 20) for heat flux measurements .....	114
Figure 5.16 Circuit diagram of voltage divider configuration.....	115

Figure 5.17 Normalization results: (a) RTD 1~16 and (b) output voltage results of paired RTDs (1 and 17, 4 and 18, 13 and 18, 16 and 20) for heat flux measurements .....	117
Figure 5.18 Relationship between normalized value and temperature .....	118
Figure 5.19 Calibrated temperature of 20 RTDs (a) RTD 1~16 and (b) results of paired RTDs (1 and 17, 4 and 18, 13 and 18, 16 and 20 ) for heat flux measurements .....	119
Figure 5.20 Heat flux results using calibrated temperature .....	120
Figure 6.1 Resistance rise at room temperature when using high temperature paste .....	123
Figure 6.2 Schematic of influence of RTD resistance on other RTDs .....	124
Figure 6.3 No cross coupling effect after using the voltage follower.....	125

## LIST OF TABLES

<b>Table</b>	<b>Page</b>
Table 1.1 Properties of SiCN vs those of other Si-based materials .....	10
Table 1.2 Specifications of several commercially available heat flux sensors .....	18
Table 4.1 Volume expansion coefficient over the filler materials under Nitrogen .....	70
Table 4.2 The ratios of filler material to CERASET® for each precursor sample.....	72

# **FABRICATION AND CHARACTERIZATION OF HEAT FLUX SENSOR USING POLYMER DERIVED CERAMICS**

SUNGHOON JUNG

Dr. Frank Z. Feng, Dr. Jinn-Keun Chen, Dissertation Supervisors

## **ABSTRACT**

In this study, a free standing Resistance Temperature Detector (RTD) sensor made from Polymer Derived Ceramics (PDCs) for high temperature application (above 1000°C) is fabricated. A newly developed fabrication method to polymerize the precursor into RTD patterns is employed, which is called direct contact polymerization method. The patterns are photo-polymerized directly on the photo mask material by a UV light source.

In addition to the free standing RTD sensor, RTD sensor arrays are also fabricated on sapphire and quartz substrate. To overcome about 35% of shrinkage rate of polysilazane polymer, Active Filler Controlled Pyrolysis (AFCP) method has been used. With the fillers of Al powder and TiB<sub>2</sub>, the shrinkage rate of our pattern after pyrolyzing at 800°C is reduced to about 3-5%, which makes the patterning of an RTD array on substrate possible. These RTD sensors on quartz and sapphire wafers are connected to the data acquisition system to find the relation between the temperature and resistance.

Furthermore, various characterization studies are conducted on fabricated RTD samples such as SEM/EDS, XRD for elemental analysis and crystallinity tests. For use as an RTD sensor, resistance of the RTD sensor is related to temperature.

To get a robust electrical connection between sensor and electrode, various methods are tested such as Printed Circuit Board (PCB) and gold sputtering on wafer. Wheatstone bridge circuit and voltage divider configuration are used for Data Acquisition System (DAQ) to obtain the temperature difference between two RTDs. From the resulting PDC RTD sensors, a Heat Flux Sensor (HFS) for high temperature application is fabricated and investigated.

# Chapter 1

## INTRODUCTION

After the techniques of Micro-Electro-Mechanical Systems (MEMS) emerged in the 1980's, there have been many accomplishments in the field of MEMS sensors such as pressure sensor, accelerometer and etc. These days, they are commercialized by many companies and employed in various applications of our daily life.

However, the field of high temperature MEMS (exceeding 1000°C), MEMS devices for gas turbine engines, high power laser systems, micro scale combustion chambers and etc., demands more effort until reliable and economical application because of material problems. As a candidate material, the current source material, silicon wafer is limited to low operating temperature [1]. Therefore, a new material for high temperature MEMS needs to be introduced. One of the most outstanding candidates for high temperature MEMS material is ceramics due to its high resistance to oxidation and thermal stability at high temperatures. However, in spite of the superior properties of ceramic material, conventional ceramics also has some drawbacks for micro sized devices. For instance, making the sintering mold needed for micro shapes is not only complex but expensive. In addition, shaping the sintered ceramic into micro scales requires very accurate machining tools and strong efforts to accomplish the delicate requirements of micro structures [2].

Polymer Derived Ceramics (PDCs) is an alternative way to obtain a ceramic material using a specially synthesized polymer. By using the PDCs, the above problems

such as: 1) choosing a suitable source material for high temperature MEMS devices and 2) shaping the ceramic material into micro structures can be avoided. By using PDC to make MEMS devices, we can not only use ceramic materials for high temperature MEMS, but also apply some MEMS techniques for shaping the PDC material into micro parts. Micro-nano size structures can be fabricated easily using micro-machining techniques such as photo-lithography and microcasting if we use preceramic polymer as a source material [2], [3],[5].

Another strong advantage of the PDC is its tailorable material properties. Especially, regarding electrical property, the final electrical conductivity varies depending on the conditions of the polymer precursor and heat treatment during polymer to ceramic conversion. Therefore, in the application of Resistance Temperature Detector (RTD) sensor, we can choose the optimal electrical conductivity to provide the sensor with good sensitivity.

So in this study, we first report fabrication of free standing RTD sensors made from Polyureasilazane polymer for high temperature application. A newly developed fabrication method for shaping the PDC into RTD patterns, which is called direct contact polymerization method is also introduced. Furthermore, PDC RTD sensors are characterized in terms of various traits such as crystallinity, oxidation and electrical conductivity to find the optimal conditions for their use as a sensor.

In addition to the free standing RTD sensor, RTD sensor arrays are also fabricated on a substrate. Generally when the synthesized polymer precursor is converted to a ceramic material, there is a significant decrease in mass and volume. For the polymer precursor that we use in this study, CERASET (KiON Defense, PA), it is reported that

there is about 35% of shrinkage rate. To get some pattern on a substrate, this shrinkage problem should be resolved. Based on the previous work by Greil et al [41], the Active Filler Controlled Pyrolysis (AFCOP) method has been used to reduce the shrinkage rate. It was found that with Al or TiB<sub>2</sub> filler powders, the shrinkage rate of our pattern after heat treatment at 800°C decreases significantly, to 3-5%, which makes the patterning of an RTD array on a substrate possible. These RTD sensors on quartz and sapphire wafers are connected to the data acquisition system to find the relation between the temperature and resistance.

## **1.1 Ceramic MEMS**

The reason for the emergence of ceramic material for high temperature MEMS is because of the limitations of the conventional silicon wafer, which is the primary source of MEMS structures. Conventional MEMS components made with silicon bulk/surface micromachining or LIGA-like techniques are not capable of long term operation at high temperatures because silicon wafers have low fracture toughness ( $\sim 0.7\text{MPa}\cdot\text{m}^{1/2}$ ), low softening temperature (600°C) and also they are highly reactive with oxygen and water, according to the nature of silicon. Furthermore, we found that the silicon wafer tends to be highly conductive under the high temperature above 300°C from our conductivity test of silicon wafer. All these factors make the use of silicon as a structural material unsuitable for high temperature environment.

Ceramic materials have drawn much attention as a high temperature MEMS material owing to their unique characteristics compared with other materials like metals,

alloys, etc. Generally, ceramics possess the properties of chemical inertness, resistance to corrosion, oxidation and abrasion, low density and superior high-temperature mechanical properties. All of these advantages make it possible to use ceramic material in many fields, especially in high temperature Micro-Electro-Mechanical system (MEMS). [1]

### **1.1.1. Drawbacks of conventional ceramics for high temperature MEMS**

However, there are several drawbacks preventing ceramics from being a good candidate material for high temperature MEMS applications. The first one is due to the nature of ceramics: brittleness, therefore it is easy to cause large stress within the body of materials, which restricts complex shape products.

The second drawback is that it is almost impossible to make the complex micro/nano-scale pattern from its fabrication process. As shown in Figure 1.1, generally, conventional ceramics are made using the sintering method. According to this general fabrication process, after ceramic powder is mixed with some binder and metals to enhance densification, some shaping process, such as casting, injection and extrusion is carried out. And then it is sintered at high temperature. This sintering process generally is used to fabricate bulk ceramic material, but it is not used for micro/nano scale ceramics since making sintering mold for micro/nano scale is very complex and expensive work..

The third drawback is that sintering is conducted under extremely high temperatures of between 1700°C ~ 2100°C and high pressure, which makes fabrication difficult and expensive.

Lastly, with conventional fabrication methods, it is almost impossible to use the MEMS fabrication techniques. Since the shaping process of conventional ceramics is

limited to molding and extrusion, the bulk/surface micromachining techniques such as etching, deposition and etc. cannot be used. [2]

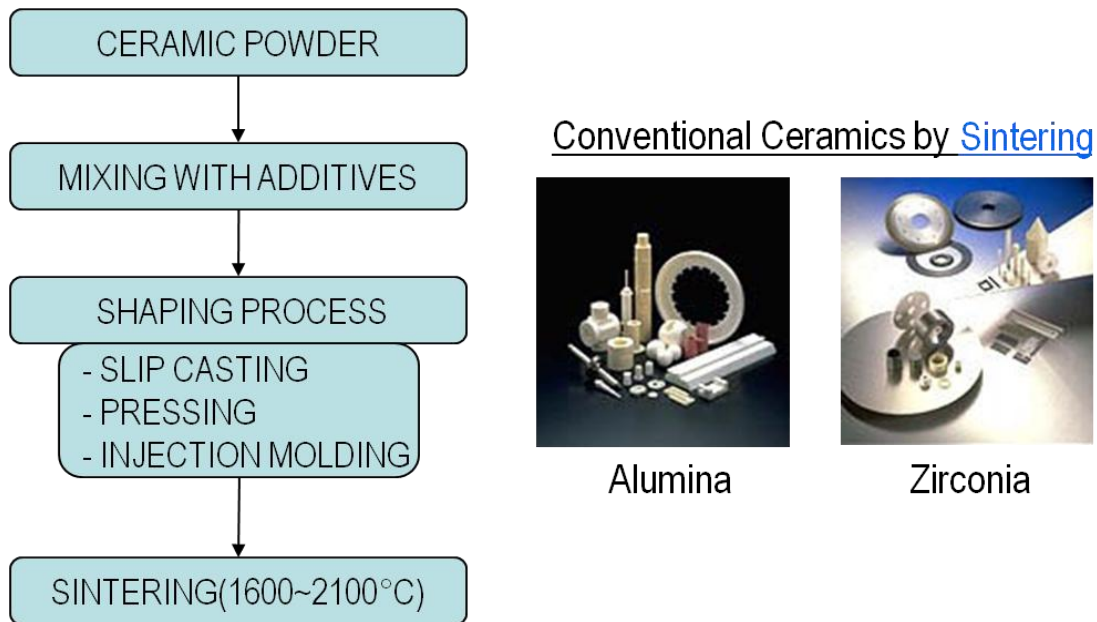


**Figure 1.1 General sintering process from powder based ceramic material**

### 1.1.2. Polymer Derived Ceramic (PDC)

These drawbacks of conventional ceramics have led to the idea of providing another route for making ceramics, which is the polymer pyrolysis route, a chemical synthesis method. Actually, several techniques have been introduced before PDC, such as chemical vapor deposition (CVD) and sol-gel processing. However, these techniques also have some disadvantages. For example, SiC can be made from the CVD method and patterned, using surface micromachining techniques such as deposition and etching. However, this process is known as difficult, time-consuming, complex and expensive procedure. In addition, the 3C-SiC thin film resulting from the CVD method has a large

residual stress caused by about 8% thermal expansion difference and over 20 % lattice mismatch that happens during high temperature 3C-SiC thin film growth on Si substrate [6]. Furthermore, it is difficult with the CVD technique to fabricate complex structures such as three dimensional components with high aspect ratios due to its planar nature.

The polymer based ceramic fabrication method was introduced in the late 1960's, by Chantrell et al. They conducted some initial work on converting preceramic polymers to ceramics [7]. However, polymer derived ceramics did not draw much-attention from researchers until the late 1970's. Verbeek *et al* [8] in Germany, as well as Yajima *et al* [9] in Japan reported their success in producing Si-based non-oxide ceramics using appropriate organosilicon preceramic polymers.

The process of making PDC starts with the synthesis of preceramic polymers. The compounds of synthesized preceramic polymers consist of structural elements that are desirable in the final product of ceramic. As shown in figure 1.2, a silicon based polymer is the most widely used source of preceramic polymers. For sure, the composition and microstructure of the final ceramic product is affected by the type and molecular structure of preceramic polymers.

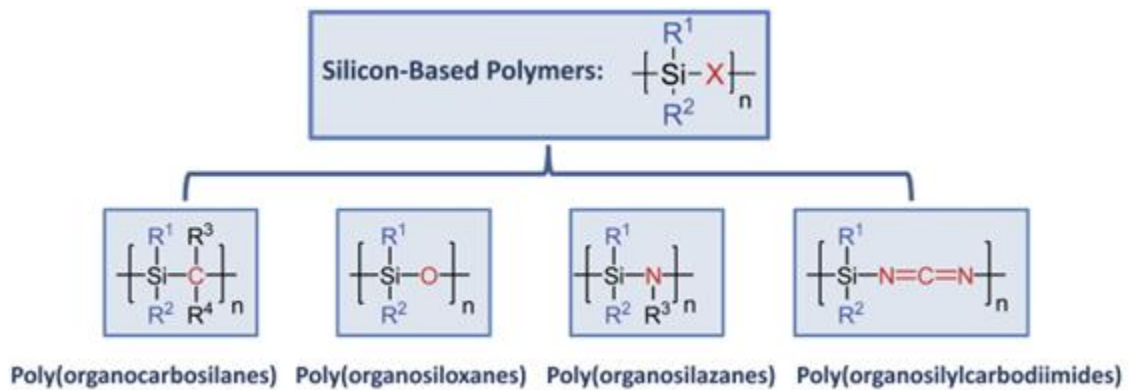


**Figure 1.2 Examples of Si based preceramic polymers (Source: Colombo et al. [3])**

Then, the preceramic polymer goes through two more steps: 1) Crosslinking and 2) Pyrolysis. During crosslinking, bonds are formed that link one polymer structure in the precursor to another polymer structure so that they can be converted into ceramics with high yields. This process can be initiated in the preceramic polymer by various triggers such as heat, pressure, radiation, agent or change in pH. In most cases of Si based preceramic polymers, after crosslinking, the resulting condition of the polymer becomes solidified. Therefore, the preceramic polymer can be shaped to a desired pattern by employing various surface micromachining techniques on the MEMS after crosslinking.

The crosslinking process is followed by pyrolysis. Pyrolysis is a thermo-chemical decomposition of organic material at high temperatures. During this thermal decomposition, the polymer structure undergoes the transition from polymer to ceramic. The desired final ceramics can be obtained in the condition of an amorphous solid after this process. The temperature range of this pyrolysis is from 800°F to 3000°F [4].

The chemical formation route of polymer derived ceramics can be summarized into three main steps described by Reidel et al. [10] as follows,

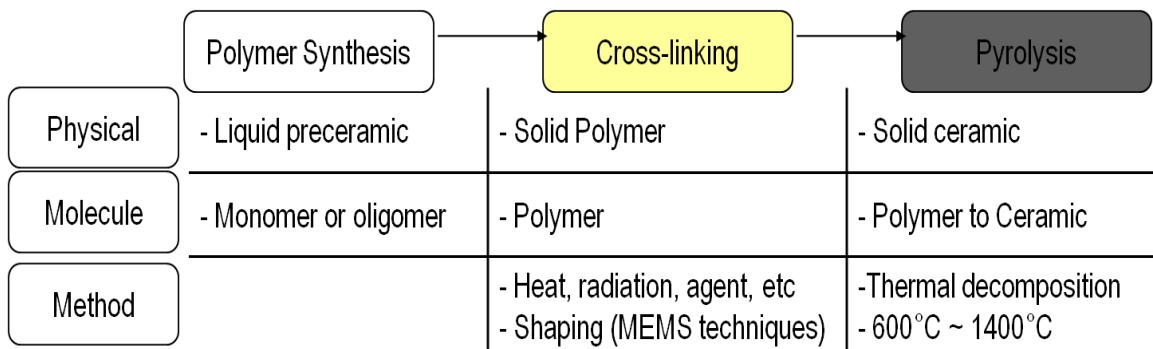


**Figure 1.3 Chemical formation route of PDC**

There are some advantages of polymer derived ceramics over conventional ceramics. In terms of impurity, for PDCs, additive metal oxides are no longer necessary due to different starting materials, the polymer precursors. Therefore, the impurities contained in the final product can be largely reduced, making it possible to achieve a highly pure ceramic material. In terms of heat treatment temperature, the pyrolysis temperatures can be lowered to 800 ~ 1500°C from 1500 ~ 2100°C using the sintering method. Also, this method is capable of generating crystalline, amorphous and metastable materials by adjusting the heat treatment cycle. Additionally, by adding the annealing step after pyrolysis, the final structure of the ceramic can contain crystalline. In terms of shapes and scales of the final products, more complex shapes and micro/nano scales of ceramics can be produced from the PDC route. Lastly, the property of the final product can be controlled by the synthesis of a precursor and also by adjusting the heat treatment process. Especially, regarding electrical properties, heat treatment has a significant effect on electric conductivity.

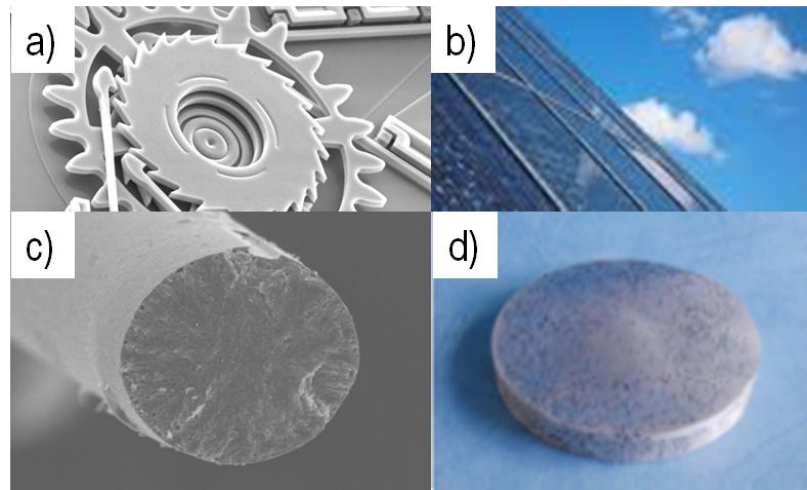


**Figure 1.4 Applications of PDCs ; a) MEMS Ratchet, b) PDC coating, c) PDC micro fibers, d) PDC-metal composites**

These advantages over conventional processing methods allow PDCs to be used for a variety of applications requiring corrosion-, oxidation-, creep- and abrasion-resistance properties. A variety of applications are shown in Figure 1.4 such as protective coatings, ceramic matrix composites; ceramic binders and joining materials; high temperature micro-electromechanical systems (MEMS).

There are, however, several limitations. In most Si based polymers, one encounters a significant amount of shrinkage rate, which is up to about 30~40%. This is a significant obstacle when one tries to make a PDC on certain substrates. This can be a noticeable limitation when placing a coating of PDC and a sensing element on a surface. The other limitations are pore formation after pyrolysis and some defects and cracks found when used in coating applications.

## **1.2. Polymer Derived SiCN**

Among some candidates for possible polymer-derived ceramics (PDCs), silicon carbon-nitride (SiCN), consisting of amorphous alloys of silicon, carbon and nitrogen was chosen as material for our RTD sensor. SiCN has proved to be one of the more feasible materials due to its excellent mechanical and thermal stabilities [5], [15] at high temperature environments. Basically, SiCN has excellent material properties at extreme environments, more flexible properties for high temperature than other materials and exhibits good creep resistance at high temperatures. Also it is durable up to 1400°C in vacuum conditions and thermally stable up to 1700°C as well as having oxidation resistance up to 1600°C in air.

As Liew et al [18], [20], [21] pointed out, the SiCN system is more feasible and suitable for high temperature application compared with some other Si-based materials shown in Table 1.1. Especially, its strength and its ability to withstand thermal shock are far superior to those of SiC fabricated by the CVD method. Therefore, it is known that SiCN would be an excellent substitute for conventional MEMS materials such as Si, SiC for high temperature applications.

**Table 1.1 Properties of SiCN vs those of other Si-based materials**

<b>Property</b>	<b>Si-C-N</b>	<b>SiC</b>	<b>Si<sub>3</sub>N<sub>4</sub></b>
Density [g/cm <sup>3</sup> ]	<b>2.35</b>	3.17	3.19
E Modulus [GPa]	<b>80-225</b>	405	314
Poisson's ratio	<b>0.17</b>	0.14	0.24
CTE [ $\times 10^{-6}/K$ ]	<b>~3</b>	3.8	2.5
Hardness [GPa]	<b>25</b>	30	28
Strength [MPa]	<b>500-1200</b>	418	700
Toughness [MPa.m <sup>1/2</sup> ]	<b>3.5</b>	4-6	5-8
Thermal shock FOM	<b>1100-5000</b>	270	890

Several examples of applications are shown in Figure 1.5, which are the electrostatic actuator, the SiCN micro gripper and a micro gear. In the prospective of MEMS sensor, these are all fabricated at the university laboratory level. So far there is no SiCN MEMS sensor reported to be commercially used. Also SiCN thick and thin pressure sensors were fabricated for high temperature applications by Leo et al [23].

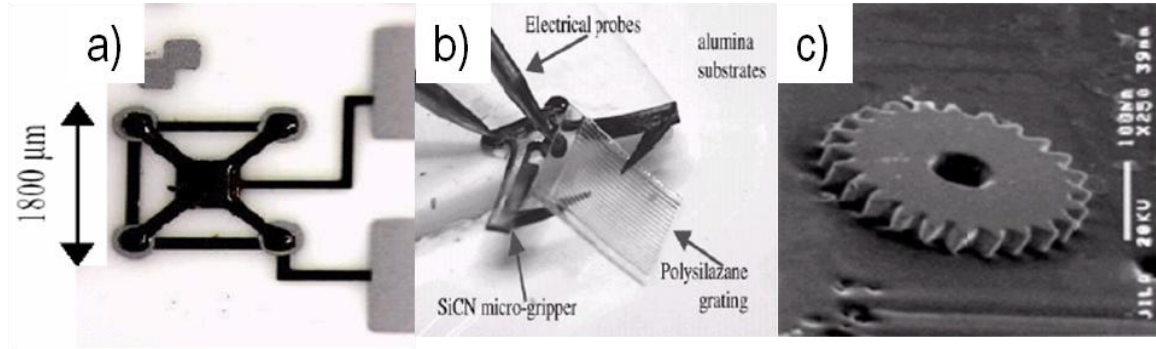


**Figure 1.5 Applications of PDC SiCN; a) SiCN electrostatic actuator, b) SiCN micro gripper, c) Micro gear**

### 1.2.1. Advantages of using PDC SiCN for high temperature MEMS

First of all, microfabrication process of PDC SiCN is much easier compared to that of Si or SiC [22]. For example, in case of 4H- or 6H-SiC and 3C-SiC, it is hard not only to perform microfabrication but also to grow those SiC thin films on Si substrate by Chemical Vapor Deposition (CVD). However, in the process of making SiCN, desired pattern can be made by UV lithography process without any etching and deposition process. As second advantage, it is possible to fabricate easily 3-D microstructures using attachment of structures and multi-layers from combination of solidification and liquid coating. With Si or SiC, making 3-D structures is very complex and time-demanding work. The third is that it is very economical because the source polymer, liquid polyureasilazane or polysilazane is inexpensive. Lastly, the amorphous nature of PDC SiCN also has advantage over Si and SiC ceramics which has crystal microstructure. Amorphous material does not contain defects such as grain interface which is often the source of failure in crystalline materials.

### 1.2.2. Fabrication techniques of PDC SiCN

In addition to its outstanding high temperature properties, various micro-fabrication techniques for PDC SiCN have been introduced over the decades including micro-powder-injection-molding [18], micro-extrusion [13], micro-casting [14], photo-polymerization [20], etc. The powder based fabrication method such as micro-powder injection molding was widely used during the early stages of PDC. However it generally has inherent limitations. For example, PDCs made from cross-linked powders are not acceptable for MEMS devices because of low strength and poor hardness resulting from high porosity.

Currently, as shown in Figure 1.6, two major methods, photo-polymerization and microcasting, are thought to be most frequently used in the micro-fabrication process for PDC SiCN. The polymer precursor is solidified after these two methods and then followed by some processes for complex structures before pyrolysis.

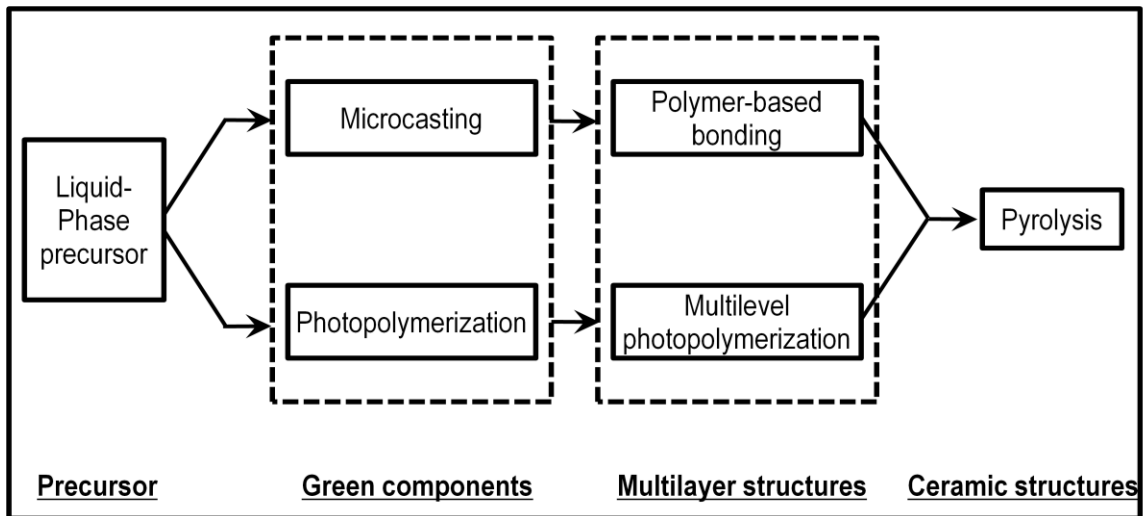
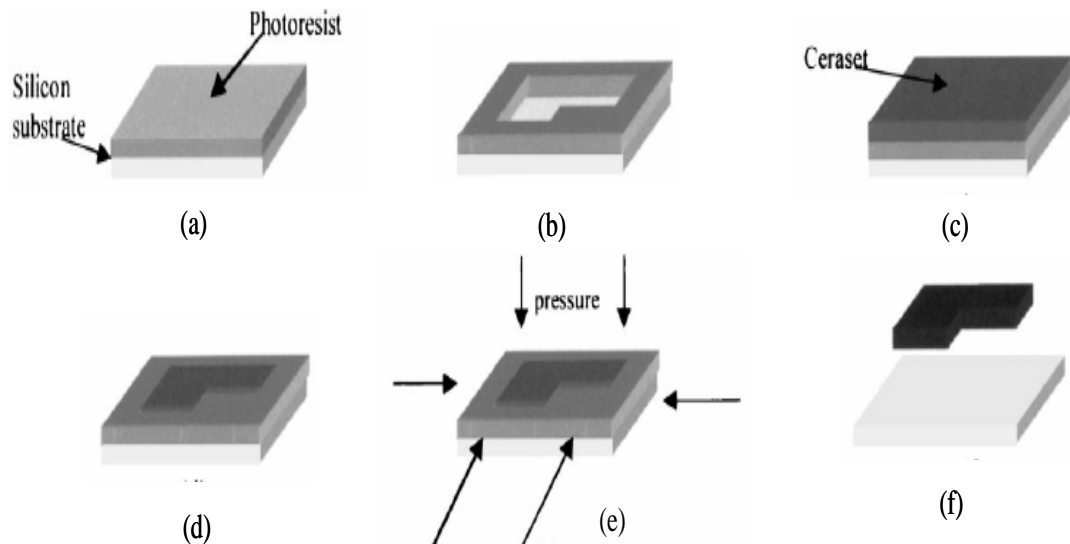


Figure 1.6 Two major fabrication techniques for SiCN (Source: Liew et al [1])

### 1.2.2.1. Micro-Casting

A general process flow for this method, as shown in Figure 1.7, starts from the fabrication of a mold using photoresist material such as SU-8 which enables high aspect ratio structures and low absorption in near-UV range. The standard photolithographic technique is applied to make the mold. Then the polymer precursor is cast into the mold followed by thermosetting and crosslinking at isostatic pressure which solidifies the UV exposed area. The unexposed portion of precursor is removed by spin-rinsing of acetone. The completed polymer structure is removed from the substrate by using a thin razor and then the free standing structure is placed into a high temperature furnace for subsequent pyrolysis. The structure is conducted to convert it to a ceramic during pyrolysis.



**Figure 1.7 General Micro-Casting process for PDC SiCN ;** (a) the photoresist is spun onto a substrate; (b) UV-lithography, producing desired shapes; (c) liquid precursor; thermal setting; solidification; (d) polish off the top layer on the wafer; (e) cross-linking under isostatic pressure; (f) pyrolysis; photoresist decomposes; SiCN part forms

### 1.2.2.2. Photo-Polymerization

In 2001, Liew et al. [18] introduced a novel fabrication technique by which one can fabricate micro-scale devices using photo-polymerization of liquid poly (urea-methyl-vinyl) silazane, commercially known as CERASET (KION Corporation, USA). According to this method, the polymerization process is started by solidifying liquid polymer under UV lights after adding a photo-initiator and followed by wet etching ending up with a pattern on substrate. After a step of heat treatment for this polymer pattern on substrate in a high temperature furnace, the PDC SiCN can be obtained. The general process is illustrated in Figure 1.8.

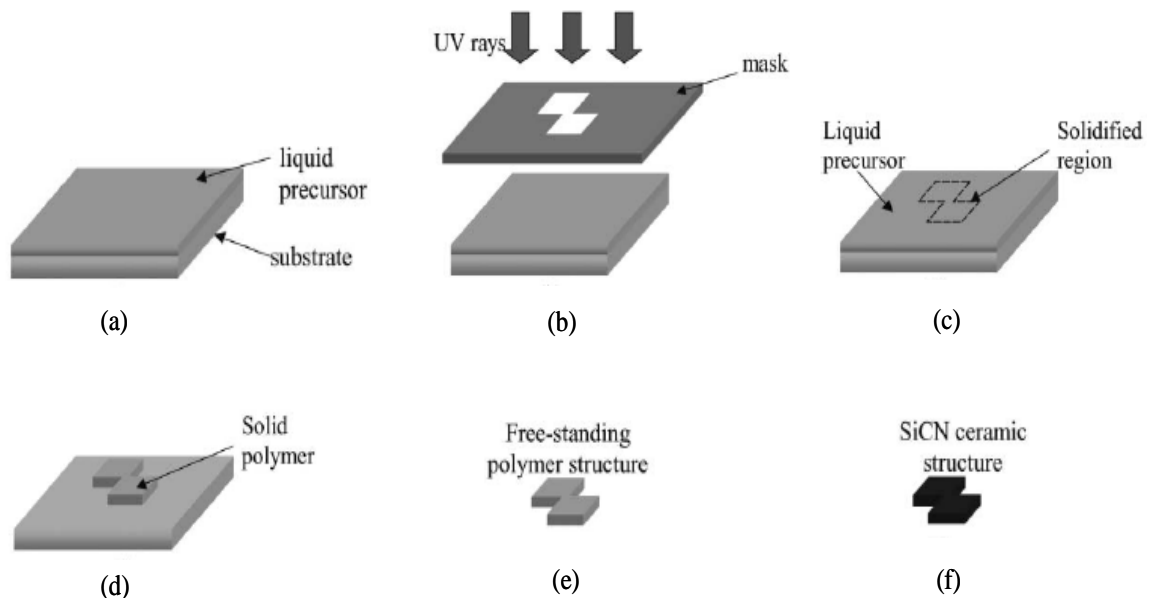


**Figure 1.8 General fabrication process of Photo-Polymerization** ; (a) spin precursor onto substrate; (b) UV exposure through a mask; (c) solidified polymer with remaining liquid; (d) remove remaining liquid; (e) remove polymer structures from substrate; (f) crosslink and pyrolysis to obtain SiCN

Besides these two major methods, other improved techniques such as micromolding in capillaries (MIMIC) and imprint lithography methods to pattern on substrate, and the micro and nano-stereolithography ( $\mu$ SL) techniques also have been introduced by researchers [17], [30], [31], as shown in Figure 1. 9. It is thought that MIMIC and imprint techniques are upgraded techniques of microcasting and photo-polymerization respectively. The MIMIC technique uses PDMS for casting mold material. Stereolithography, a similar method to photo-polymerization, which uses a laser system instead of UV to solidify the precursor, was recently introduced to fabricate complex 3D ceramic parts. A complex geometry can be created by multiple patterning processes on one substrate after the system is programmed with complex structures.

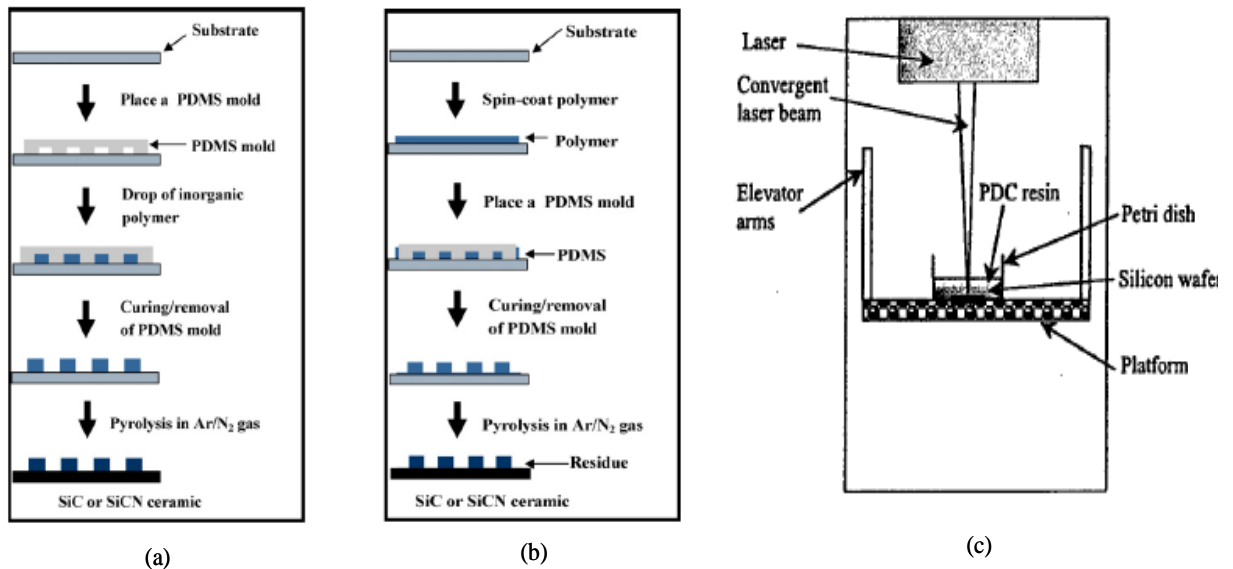


**Figure 1.9 Other techniques for PDC SiCN fabrication; (a) MIMIC, (b) Imprinting, (c) stereolithography techniques (Source: Lee et al [30])**

Although prototypes of PDC parts have been developed after heat treatment, obtaining a part with a well defined geometry and sufficient mechanical strength remains

a challenge. Also, existing fabrication techniques are still relatively expensive due to the spin coating of precursor which requires some skillfulness. Moreover, since the UV exposure usually performed is a non-contact method, it requires a precisely controlled gap between photolithographic mask and the precursor to produce clear patterns. To improve wall definition, an SU-8 photoresist mold [20] and PDMS mold [30], [33] are used. Although wall definition could be improved by PDMS or SU-8 photoresist molds, additional processes are still required to prepare those molds. Furthermore, these processes are time consuming and waste the bulk of the CERASET precursor during the spin coating process.

### **1.3. Electrical conductivity of amorphous SiCN**

Besides the thermal and chemical stability in harsh environments, PDC SiCN has an attractive feature of controllable electrical conductivities. Early studies [16], [21] have shown that SiCN can be imparted with electrical properties by changing its microstructure through altering the material synthesis conditions such as pyrolysis temperature, atmosphere and annealing time applied during synthesis. Because of the relative newness of SiCN materials, presently there are few existing studies on SiCN, and fewer still on its semi conductive properties. One such study on electrical properties was done by Haluschka et al. [16] in which it is reported that when annealed at temperatures above the pyrolysis temperature, SiCN can be made electrically conductive. It was found that three main conducting material phases developed; hence there are three temperature regimes for annealing which correspond to micro-structural changes and hence electrical

transport mechanism. Also, in this study, the a.c. and d.c. conductivity of annealed SiCN specimens was measured, and it was found that the higher the annealing temperature, the more the d.c. conductivity dominates. Another study on SiCN electrical properties was done by Hermann et al. [36]. It was found that adding boron to SiCN—thus forming SiBCN—enhances electrical conductivity at all temperatures. However, this increase in conductivity cannot be thought of as due to boron doping alone, since adding boron also changes the ratio of Si:C:N in the final ceramic. Also, if annealing is carried out above 1300°C, crystalline impurities of SiC may form. Consequently, the increased conductivity cannot be thought of as an intrinsic property of SiCN alone. Furthermore, annealing increases a material's conductivity through a loss of hydrogen. This leads to an increase in the sp<sup>2</sup>/sp<sup>3</sup> ratio of the carbon atoms lowering the energy barrier for the transport of charge carriers.

Another important feature of amorphous PDC SiCN is the fact that its electrical conductivity changes with the temperature. Previous study reported that its resistance decreases when the temperature increases, a trait that can be seen in semi-conducting materials such as silicon. This property is very critical in our study since we have used this property of temperature-dependent resistance in making our SiCN RTD which will be employed for our heat flux sensor.

#### **1.4. Heat Flux Sensor (HFS) using SiCN MEMS**

The measurement of heat flux is based on the measurement of the temperature. There are two basic configurations in measuring heat flux [58]. In the first configuration, heat flux is obtained through measuring the rate of temperature rise of a heat-receiving

mass, temperature sensor. In the second configuration, heat flux is obtained by measuring the temperature gradient between two temperature sensors. For more accurate heat flux measurement, the measurement of small temperature differences over small spatial separation is required.

Commonly used temperature measurement method is based on the Seebeck effect, which is the principle of thermocouples: a Seebeck voltage is generated between two ends of the conductor that depends on the temperature difference of the ends and material property [59]. The Seebeck effect is the opposite of the Peltier effect found in thermoelectric materials. Many thermocouples arranged in a thermopile are often used to obtain adequate sensitivity, which is increased Seebeck voltage. However, there is a limitation to use these thermocouples as temperature sensor for high temperature application (above 1500°C), which is operating temperature. Generally, thermocouple of type E, J, K, T, N has the operating temperature range of -250°C to +800°C and although type B, S, R has higher working temperature of up to about 1200°C, but it has cost problem due to the source material, which is platinum and rhodium.

**Table 1.2 Specifications of several commercially available heat flux sensors**

Vendor	Vendor Info	Max Temperature	Response Time
Wuntronic	wuntronic@wundronic.de	549°C	8 sec
Omega	Omega.com	150°C	0.62 sec
RdF Corporation	<a href="http://www.rdfcorp.com">www.rdfcorp.com</a>	260°C	0.05 sec

Heat flux sensors based on microfabrication technologies have been developed [60], [62], [63], [65]. These sensors have the advantage of small size and low cost. Unfortunately, commercially available heat flux sensors are limited in temperature range. Table 1.2 lists a few important specifications of several commercially available heat flux sensors.

These sensors are inadequate for sensing during laser irradiation. The low temperature limit prevents us from placing the sensor too close to the intense heating spot. Moreover, the physical sizes of these sensors are usually too large to imbed them inside the materials for the actual application.

With regard to operating temperature, our PDC material has higher limit than ordinary thermocouples and much inexpensive cost since pre-ceramic polymer is used as a source material and the final product of ceramic has extraordinary thermal and mechanical property. As Nagaiah et al. (2006) [26] suggested, the polyureasilazane based PDC material has proven semiconducting property for the use of Resistance Temperature Detector (RTD). Therefore, our PDC RTD is used for the temperature sensing element for Heat Flux Sensor that has thermal resistance layer between PDC RTDs. After the measurement of temperature gradient of two RTDs, the heat flux can be calculated by the Fourier's law,

$$Q = -k\nabla u = -k \frac{\Delta T}{\Delta x} \quad (1.1)$$

There will be two types of PDC RTD introduced in this study. One is free standing SiCN RTD. After obtaining the desired resistance and temperature relationship, they are attached to middle layer of OMEGABOND 400 (Omega, USA) for both sides.

Then, the RTD elements were configured in a Wheatstone bridge to obtain the temperature differences between two points with a small spatial separation. The bridge arrangement has proven to be very sensitive in detecting small temperature differences. The middle layer serves both for electric isolation and for thermal isolation.

The other types of PDC RTD is doped PDC RTD. To use a ceramic based substrate such as quartz ( $\text{SiO}_2$ ) and sapphire ( $\text{Al}_2\text{O}_3$ ), the PDC should survive after heat treatment. However, it is very hard due to its large shrinkage rate (30 ~ 40%). To avoid this problem, doped PDC RTD is used for Heat Flux Sensor. The fabricated heat flux sensor will be investigated under controlled temperature range.

## **1.5. Literature reviews**

### **1.5.1. Fabrication of SiCN**

As mentioned in the introduction, over the last decade, a variety of PDC SiCN fabrication techniques were presented. The first attempt was made by using the sintering of the powder obtained from a crosslinked polymer (polyureasilazane). However due to not only its higher porosity but also poor hardness, the powder based method became a rarely used technique. These days, it seems that photopolymerization and microcasting are the most frequently used techniques among the researchers.

Liew et al [18] demonstrated a novel processing technique for the fabrication of SiCN involving four steps: (1) casting a liquid polymer into molds; (2) thermosetting the polymer; (3) bonding the different solid polymer parts for complex structure; (4) thermal

decomposition. They also implemented MEMS components with complex three dimensional, multi-layer structures.

Another study done by Liew et al [20] described the use of photopolymerization of a liquid polysilazane as a novel, versatile and cost-efficient means of fabricating SiCN ceramic MEMS. They patterned a polymer precursor on substrate using UV exposure after adding a photoinitiator followed by heat treatment in a high temperature furnace. Also, three SiCN MEMS devices have been fabricated: an electrostatic actuator, a pressure transducer and a combustion chamber.

Cross et al. [39] presented a new process using contact lithography of aqueous photopolymers. It showed substantial improvement in resolution, flatness of structures and aspect ratios compared to microcasting and proximity printing for polysilazane-derived MEMS.

Liu et al. [24] suggested an application of microforging to SiCN fabrication to overcome the shrinkage mismatch problem between the SiCN structure and mold during thermal processes.

Lee et al. [30] fabricated highly stable SiCN ceramic patterns on Si substrates with dimensions of sub-micron scale after pyrolysis at 800°C. Two soft lithography techniques were used: modified imprint lithography and micromolding in capillaries.

Haluschka et al [15] reported on the compositional and structural properties of ceramics in the SiCN system. From their experiments, they knew that chemical composition, solid state structure, microstructure as well as crystallization behavior depended on: (1) the synthesis conditions; (2) the pyrolysis atmosphere; and (3) the time and temperature of a final heat treatment.

Schulz et al [28] presented the direct manufacturing of SiCN microstructures by using ceramic precursor in combination with X-ray lithography.

### **1.5.2. Electrical property of SiCN**

Much research has also been conducted on the electrical properties of amorphous SiCN materials. It turned out that the conductivity of SiCN can be tuned through the synthesis conditions in process and it has a semiconductor-like conductivity change: the conductivity increases as temperature goes up.

Haluschka et al. [16] showed from their measurement of the electrical properties that the d.c.-conductivity can be controlled within 15 orders of magnitude by applying a different temperature, atmosphere and annealing time during synthesis. They claimed that the main mechanism is tunneling of large polarons.

Xu et al [38] measured the electrical conductivity of PDC SiCN with varied composition as a function of temperature from room temperature up to 700°C. Also they implemented Al doping in the precursor, resulting in a higher electrical conductivity.

Liew et al [21] also completed a SiCN heat treatment process that was conducted in a hot isostatic press (HIP). In their work, they showed the room temperature electrical conductivity of SiCN using four linear probes. And they fabricated an SiCN lateral thermal actuator and micro-grippers for moving chip-sized objects to demonstrate an application of this functionalized material.

### 1.5.3. Heat flux sensor and temperature sensor using ceramics

Nagaiah et al [26] attempted to prove the feasibility of a novel high temperature heat flux sensor made by thin SiCN and SiAlCN layers for a gas turbine environment. They proposed a design and fabrication process and schematic showing the structure of the heat flux sensor.

Volklein et al [59] presented a micro heat flux sensor using thin  $\text{Bi}_{1-x}\text{Sb}_x$  films created by photolithography. The sensor consists of ten membranes with 889 thermocouples on each membranes showing higher sensitivity. The sensor was calibrated using an integrated thin film heater.

Oh et al [63] designed a micro heat flux sensor that could measure the thermal energy transfer per unit area. The sensor based on a circular foil gage is composed of thermal paths and a thermopile. The sensitivity of the heat flux sensor of Ni-Cr or Al0Cr pairs is in the range of 0.1~2.0 and 0.4~2.0  $\mu\text{V}\text{mW}^{-1}\text{cm}^{-2}$  respectively.

Wrbanek et al [66] investigated the feasibility of ceramics as thin film thermocouples for extremely high temperature applications. They selected  $\text{CrSi}_2$  and TaC as ceramic materials for thermocouples and measured thermoelectric power, an option that proved to be quite successful.

Gregory et al [34] developed a ceramic thermocouple based on indium-tin-oxide thin films to measure the surface temperature. The thermoelectric power of the sensor was  $6.0\mu\text{V}/^\circ\text{C}$ . And they conducted thermal cycling of ITO films in various oxygen partial pressures showing that the temperature coefficient of resistance was nearly independent of oxygen partial pressure at temperatures above  $800^\circ\text{C}$ .

## 1.6. Objectives

In this study, our goal is to contribute to recent research of polymer derived ceramic MEMS in terms of the fabrication process of amorphous SiCN, and to investigate characteristics, especially the resistance-temperature relation of Resistance Temperature detector (RTD) made by PDC SiCN material. Lastly, heat flux sensor made by those PDC RTDs is fabricated and the heat flux is calculated.

First, even though many fabrication techniques such as micro-casting, photopolymerization, etc., have been presented, researchers are still trying to find a better fabrication method which is easier and less time-consuming as well as economical. Therefore, one of our objectives will be related to finding an alternative approach to fabricating a free standing SiCN and SiCN on a specific substrate.

Second, to obtain the robust RTD, i.e. ceramic temperature sensor is the pre-step for fabricating a high temperature heat flux sensor. Much effort will be devoted to getting the data on the temperature dependency of the electrical conductivity of SiCN after an appropriate heat treatment process in a high temperature furnace. More effort is needed to obtain the electrical conductivity data for PDC SiCN since current studies performed so far are just showing the limitation on maximum temperature which is around 2~300°C. After trials and errors based fabrication of PDC SiCN RTDs with different heat treatment conditions followed by an investigation of the electrical conductivity of both materials, the optimal one will be selected as an RTD materials based on the sensitivity and repeatability of the resistance value with the temperature cycling.

Third, a prototype of a high temperature heat flux sensor which has an amorphous SiCN as an RTDs component will be fabricated after an appropriate middle layer is found. Sensors are subjected to a configuration of circuits to find the resistance difference between two RTDs by which heat flux is calculated.

## Chapter 2

### FABRICATION OF FREE STANDING PDC SiCNs

#### 2.1. Introduction

The recent development of a new class of polymer-derived ceramics consisting of amorphous alloys of silicon, carbon, and nitrogen suggested a number of possibilities for the high temperature MEMS field. After this new material and fabrication method were introduced, several attempts to fabricate MEMS sensors have been tried such as micro-gripper, electrostatic actuator, pressure sensor by [20], [21] etc. However, still numerous applications in the field of gas turbine and high power generation provide an interesting and ongoing challenge.

One of those challenges, the fabrication of a heat flux sensor using SiCN ceramic, is investigated in this thesis. To reach that final goal, the fabrication of a PDC SiCN is executed as a first step in this chapter. As described in the introduction, for the fabrication of PDC SiCN, there are two major methods that are most frequently used. Those are photo-polymerization and microcasting. The former is employed in our experiment to make our own SiCN ceramic in a newly modified way.

The method of photolithography (or photopolymerization) is a well known technique to fabricate polymer structures. It is favored because of its relatively easy processes and its low cost as compared to the microcasting method. The advantages of this method are that liquid precursors such as CERASET (Kion cop. USA) can easily be

solidified from UV exposure by adding a photo initiator. Therefore, one can make a desired structure by using UV exposure with a photomask. And also, there is no need to make a mold for casting as with microcasting or micoforging [18], [24].

### 2.1.1. Problems in conventional photo-polymerization

Figure 2.1 shows a typical setup for conventional photo-polymerization. First, a preceramic precursor is spincoated over the whole wafer area. The spacer and photomask are placed on top of the precursor. UV light goes through the mask and makes a pattern in the precursor layer.

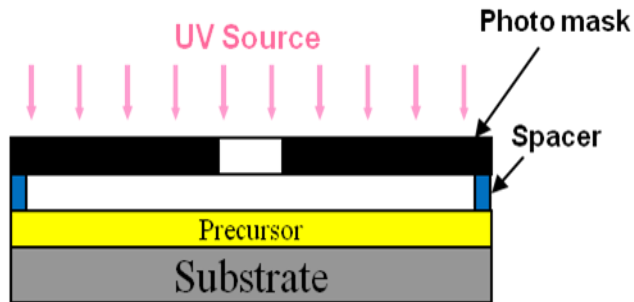


**Figure 2.1 Conventional photo-polymerization method**

However, there are some problems considered as shortcomings in conventional photo-polymerization. These include: (1) a waste of polymer precursor, which is caused by the spincoating of the polymer precursor to get a certain amount of thickness over the whole surface of substrate, (2) poor wall definition, caused by UV light diffraction in the space of the gap between mask and the spincoated precursor. Generally the UV exposure performed is a non-contact method to keep the mask from sticking to the polymer precursor. However, there should be a gap between mask and substrate, which causes an

extension of the shapes of the photomask in the form of residue at the bottom of the wall because of the UV dispersion and diffraction phenomenon. As shown in Figure 2.2, due to the diffraction, unexpected UV exposure occurs near the edge of the actual shape.

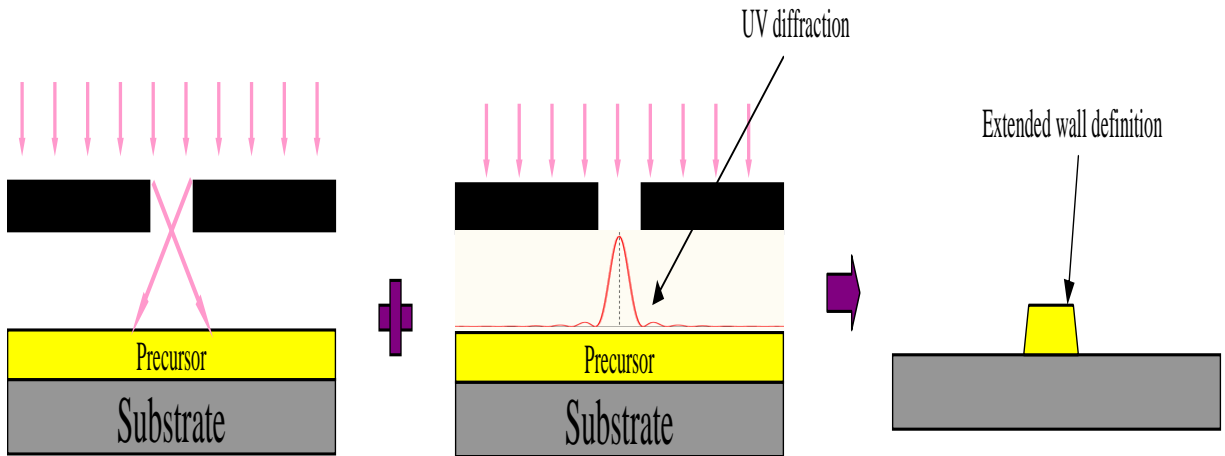


**Figure 2.2 Schematic of poor wall definition by UV dispersion and diffraction**

Therefore, the actual shape of a polymerized precursor on substrate is affected by UV dispersion and diffraction resulting in some amount of enlargement of polymerized pattern and poor wall definition. One can resolve this problem by making the gap as small as possible using instruments such as spacer etc. However, the mask and the precursor tend to make contact with each other due to the uneven surface of the spincoated precursor when the gap becomes really small, which ruins the setup.

In this chapter, a modified photo-lithography technique for PDC SiCN fabrication is introduced, which is called direct contact lithography. In order to overcome the problem with resolution of the patterning and also to get rid of unnecessary processes required in the previous non-contact lithography technique, a novel direct contact lithography technique has been developed. There is a direct contact between the liquid

precursor and the plate glass substrate or photomask which can result in higher resolution patterns. Also, the process is easier compared to non-contact lithography because we can skip the spincoating process of the polymer precursor before UV exposure.

## 2.2. Free-standing PDC SiCNs Fabrication process

### 2.2.1. Precursor preparation

The fabrication of SiCN patterns starts with the preparation of a liquid precursor. The commercially available CERASET™ (Polyureasilazane, KiON Defense Technologies, Inc., PA, USA) and 2,2-dimethoxy-2-phenyl acetophenone (Irgacure 651 from Aldrich Chemical, WI, USA) as shown in Figure 2.3 (a) are used as a UV sensitive monomer (or oligomer) and photo initiator.



**Figure 2.3 (a) Polymer (Polyureasilazane) and Photo initiator and (b) UV exposure box**

The precursor is prepared by adding 5 wt% photo initiator to CERASET then mixed using magnetic stirring at 70~80°C for 12 hours. During magnetic stirring, the

dark vial or transparent vial with cover-up is used to protect the precursor from exposure to light from outside. After that, the transparent yellowish liquid precursor is placed in a vacuum oven in 30in Hg for 10 hours to eliminate bubbles in the precursor which create pores and weaken the hardness of PDCs.

## **2.2.2. A novel direct contact lithography technique for patterning**

### **2.2.2.1. *Process of direct contact lithography***

The idea for our direct contact lithography starts with removing the gap between mask and precursor as shown in Figure 2.1. To do that, instead of putting a photomask over the polymer precursor, the precursor is dropped onto the photomask itself so that the precursor is in direct contact with the photomask. By placing the UV light source (KVB – 30, KINSTEN, 55mW/cm<sup>2</sup>) as shown in Figure 2.3 (b) directly under the photomask, the precursor is exposed and polymerized by UV light from the bottom. Therefore, no gap between mask and precursor prevents the UV light source from diffracting light in the liquid precursor. Figure 2.4 shows the general photo-lithography process used to fabricate a free standing polymer structure using our novel direct contact lithography technique. In this technique, several drops of the liquid precursor are placed on a photomask followed by UV light exposure at the bottom of the photomask. Polymerized structures then remain right on the photomask after an acetone rinsing of the unexposed region of the liquid precursor. Free standing polymer structures are obtained after removing them from photomask.

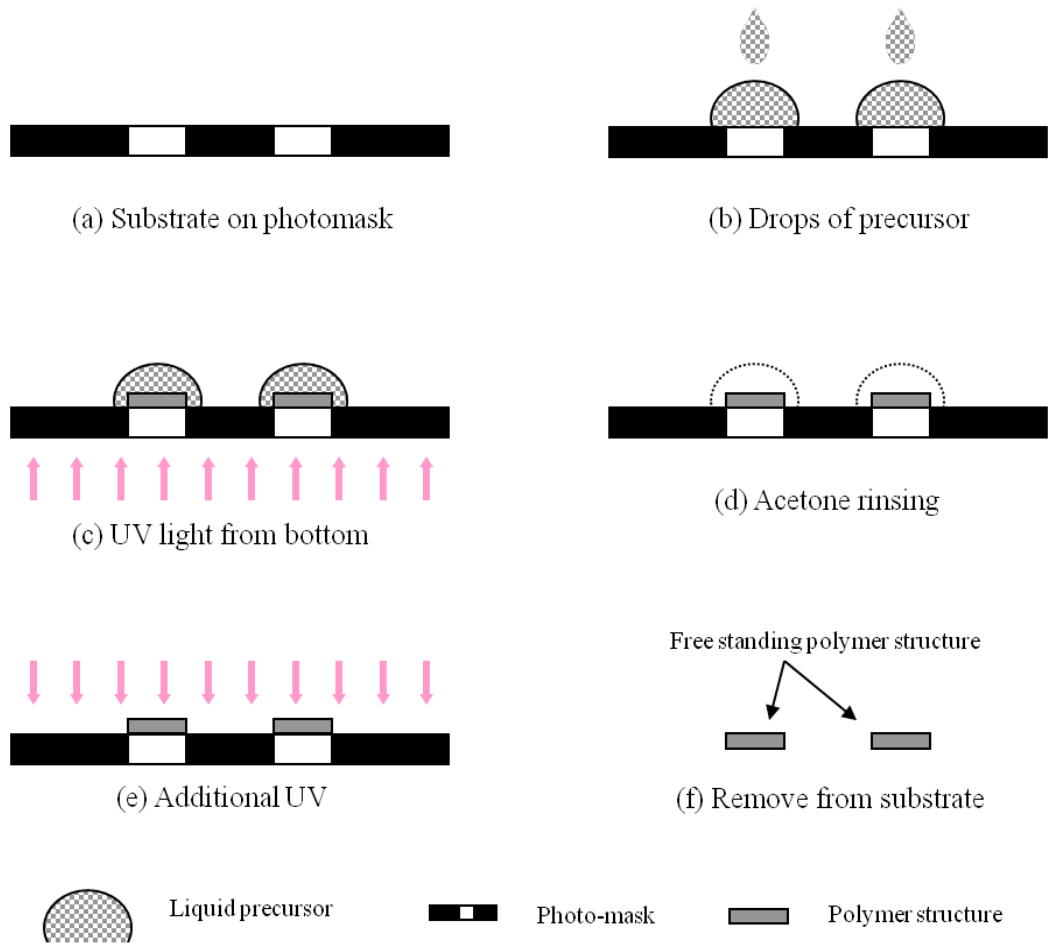


**Figure 2.4** The schematic of the direct contact fabrication process

**2.2.2.2. Process of direct contact lithography using Teflon film**

Another novel feature of this method is the usage of a very thin (~0.001”) transparent Teflon film as a separation layer. It is placed on the photomask so that in fact the precursor is dropped on the Teflon film. Teflon film is so thin that the dispersion and diffraction effect of UV caused by Teflon film is negligible. The Teflon film will help not only remove the polymer structure much easier after developing the pattern, but will also

protect the photomask from being damaged by the polymer precursor, making the photomask reusable. After developing the pattern on Teflon film, the polymer structure can be removed easily from the film. In addition, because the film is very thin, the pattern will not be affected as much by the diffraction phenomenon as in conventional photo-polymerization.

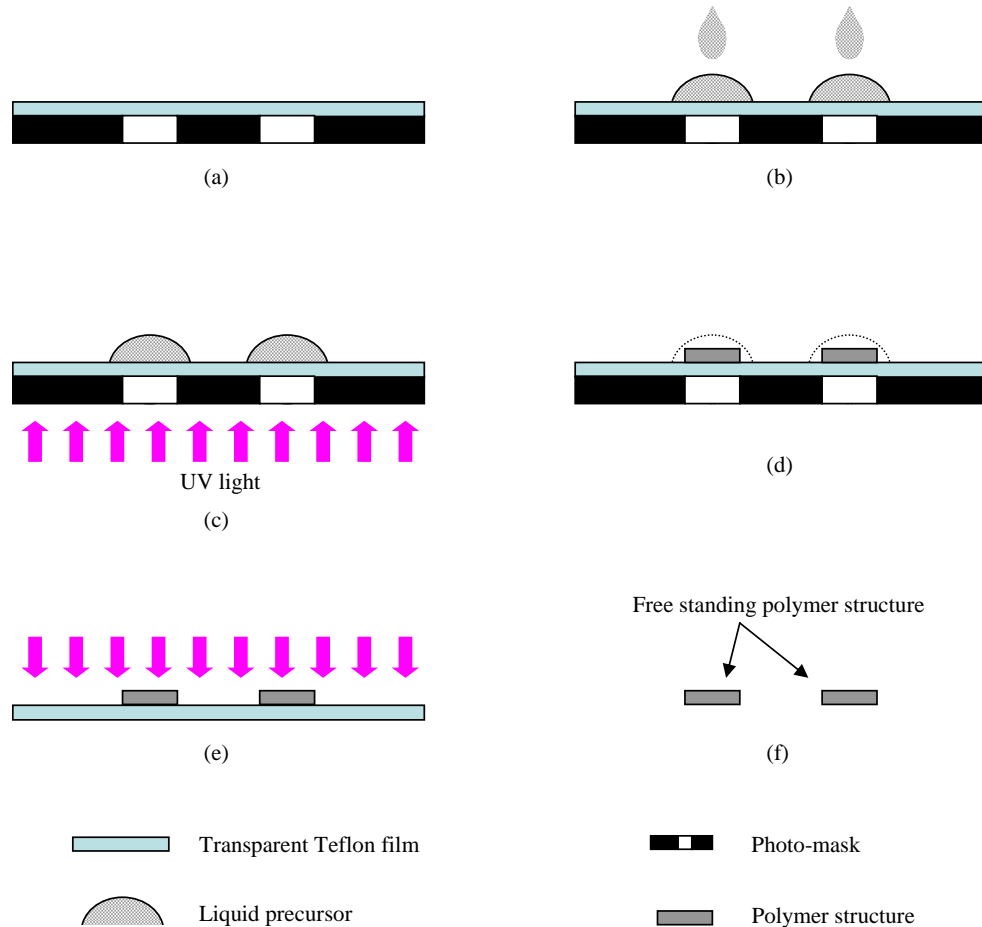


**Figure 2.5** The schematic of direct contact fabrication process using Teflon film; (a) place transparent Teflon film on the patterned mask; (b) apply liquid precursor drops on the transparent Teflon film; (c) apply UV exposure from bottom of patterned mask; (d) etch out the unexposed area by acetone; (e) perform UV cure from top to solidify upper part of patterns; (f) remove the patterned structures from Teflon film

Figure 2.5 shows the direct contact lithography process to fabricate a free standing polymer structure using Teflon that is described below.

First, after precursor preparation, the transparent Teflon film, measuring 0.001” thickness, is placed on the photomask. It is used as practical layer to prevent adhesion between the photomask and the liquid precursor, an adhesion that makes the photomask unusable. Then, several drops of the precursor are applied to the transparent Teflon film. After that, the precursor is subjected to UV exposure (KVB 30, KINSTEN, 55mW/cm<sup>2</sup>) from the bottom of the photomask. The unexposed areas are then removed by acetone solution rinsing.

After removing the unexposed areas, only the patterns remain attached on the transparent Teflon film as shown in Figure 2.5 (e). The developed polymer structures can be easily removed from the Teflon film due to its low coefficient of friction (second-lowest of any known solid material) and finally free standing polymer structures are obtained.

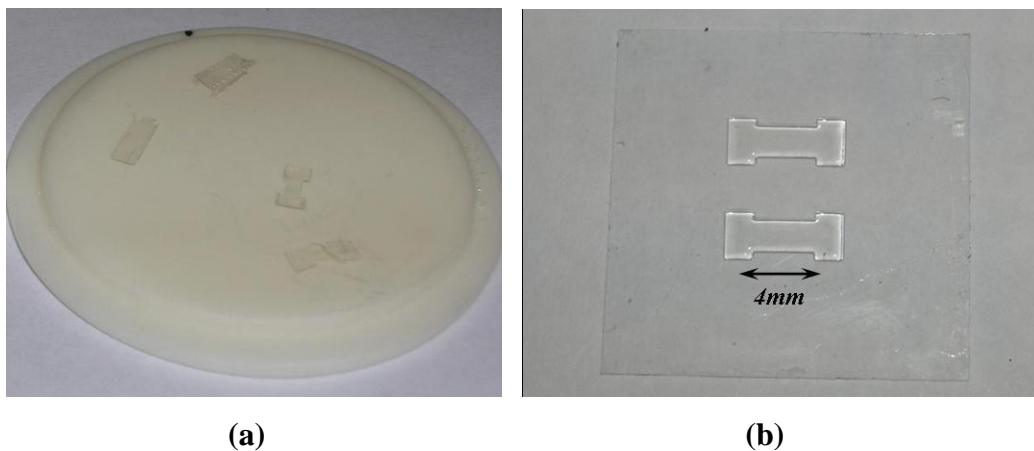


**Figure 2.6 Completed polymer patterns of precursor on the glass substrate**

In Figure 2.6, completed patterns made by direct contact lithography are shown. In the Figure 2.6 (a), removed polymer structures are put on alumina plate and in Figure 2.6 (b), a micro thin glass wafer is used as a transparent substrate and the patterns are not yet removed.

### **2.2.2.3. Additional UV exposure**

In our method, after developing the patterns by etching with acetone solution, additional UV exposure is performed to solidify whole patterns. Such additional exposure facilitates the removal of the patterns from the transparent Teflon film or photo mask. Basically, quite good resolution can be obtained after acetone rinsing. However, the top parts of the patterns still remain in a gel-like solid state because UV rays are from the bottom of the substrate and the upper parts are more exposed to acetone during the rinsing process which results in less solidification compared to the bottom part of the developed precursor. Therefore, additional UV exposure is applied to solidify the whole patterns. Without this additional exposure, the patterns cannot be easily peeled off from the substrate as shown in Figure 2.7 (a). When the removing process is performed without additional exposure, the patterned precursor tends to stick to the razor blade and collapse because of the poor hardness of the top part of the pattern. However, after additional exposure, a well defined shape of the developed precursor can be obtained by using a razor blade as shown in Figure 2.7 (b). Obviously, the time for additional exposure depends on the thickness of the developed precursor. After numerous trials, it was found that approximately 100 seconds of additional UV exposure time is necessary to get the appropriate hardness of the top part of pattern.

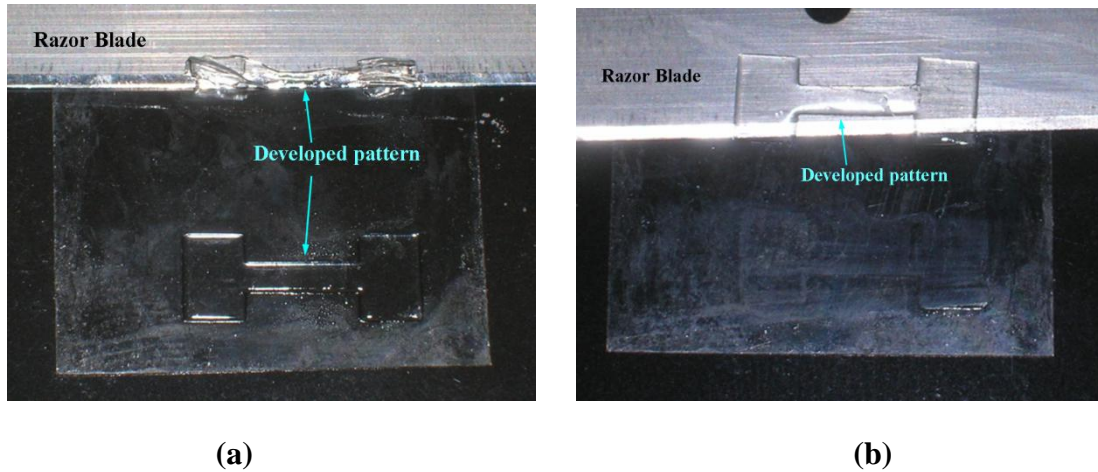


**Figure 2.7 Removing precursor patterns using a razor blade; (a) without additional UV-exposure (b) with additional UV-exposure**

#### **2.2.2.4. Removal of patterns from substrate**

After additional UV exposure, the solid patterns are easily removed from the transparent photo mask or Teflon film. In the case of Teflon film, it is very easy to detach the pattern by simply bending the Teflon film due to its non-sticky property. However, in the photo mask case, as demonstrated by Liew et al [20], [21], a razor blade is a very useful tool for detaching when silicon oil is used as a lubricant. With just a small amount of silicon oil on the razor blade, the pattern is removed easily from the photomask. Unfortunately, using the razor blade sometimes causes mechanical damage on the pattern such as cracks and/or breaking of the polymer pattern.

Before placing the transparent free standing patterns of polymer precursor in the high temperature furnace, those patterns need to stay exposed in the air at room temperature for about 20 hours. Because right after the acetone solution rinsing, acetone remains in the patterned precursor, this will cause cracks in the pattern if they are put in

the furnace. Therefore, they need to stay in the open air for a while until all of the acetone in the patterns dissipates and they acquire solidity.

#### 2.2.2.5. Advantages of direct contact lithography

In short, there are two main differences between non-contact and direct contact UV exposure methods. In the latter method, there is (1) direct contact between photomask and the polymer precursor; (2) a UV light source comes from the bottom. Besides those main differences, more specific differences include the use of a very thin transparent Teflon film as a practical layer which allows us to provide additional UV exposure to facilitate easy removal of the patterned precursor structures. Thus, the direct contact lithography method has several advantages over the conventional non contact method.

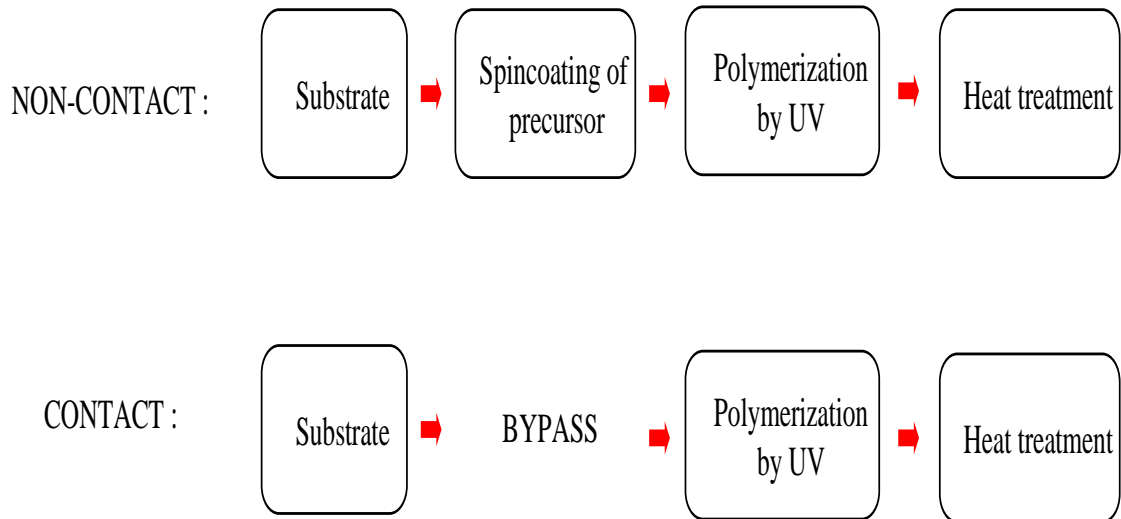


**Figure 2.8 Comparison of fabrication process of non-contact lithography and novel contact lithography**

First, it will be noted that in the direct contact method, the polymer patterns can be completed with very simple processes. As shown in Figure 2.8, using our method, the spincoating process doesn't need to be conducted. Instead of spincoating whole area of wafer, properly measured drops of the precursor need to be placed directly on the Teflon film or photomask.

Second, our method can reduce the dispersion and diffraction effect during UV exposure. This allows the final dimensions of the polymer patterns to be more precisely duplicated from the transparency mask; even better dimensions of polymer patterns can be obtained if a chrome coated hard mask is used.

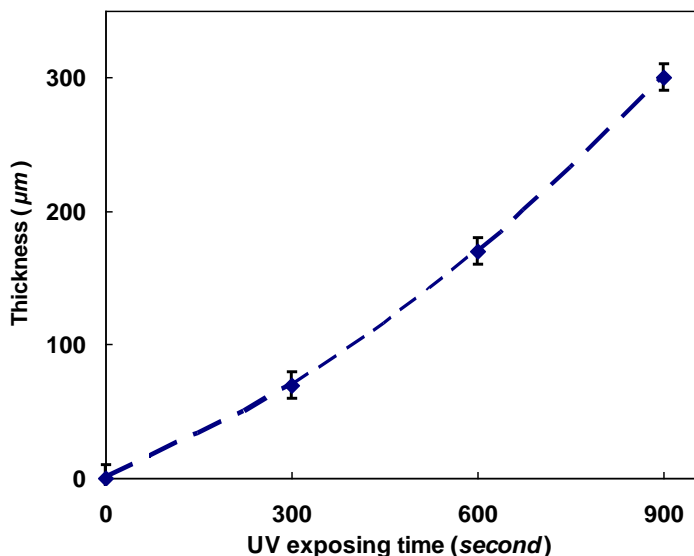


**Figure 2.9 Thickness of the precursor patterns as a function of UV exposure time**

Third, the thickness of patterns can be controlled by controlling UV exposure time as shown in Figure 2.9. It shows that when the intensity of UV light is  $55 \text{ mW/cm}^2$ , the thickness of the polymer structure increases with the UV exposure time.

Fourth, the direct contact method reduces the liquid precursor usage because it does not need to spread the precursor on a substrate by spin-coating. This is very important for cost effectiveness and good for the environment; it reduces a significant amount of precursor usage.

### **2.2.3. Heat treatments for SiCN structures**

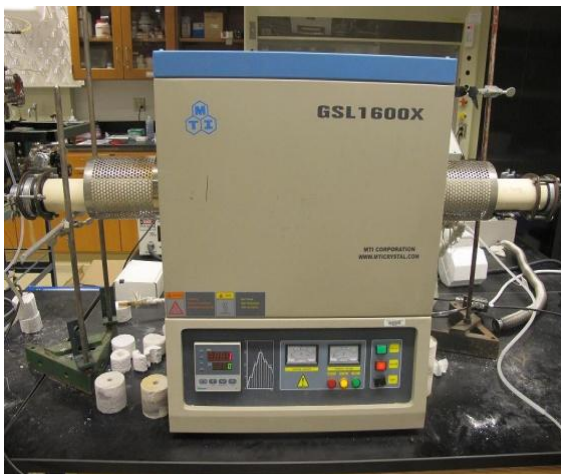
The polymerized patterns are converted to amorphous SiCN ceramic materials by heat treatment in a furnace according to the three chemical formation routes described in the introduction. The fundamental processes for this conversion are crosslinking and pyrolysis. Also from other study and from the data sheet of CERASET provided by the manufacturer (KiON, USA), those two processes will be fundamental for the precursor to be converted to amorphous SiCN ceramics. Also, as is well known, pyrolyzed amorphous SiCN shows that some patterns of conductivity increase with a rise in temperature similar to the semi-conductors [16]. Because of this property, this PDC forms the RTD and finally the high temperature heat flux sensor.

However, its electrical conductivity, when using only the pyrolysis process, is too low to be used as an RTD sensor. Its electrical conductivity at room temperature is about  $10^{-10} \sim 10^{-7}$  /ohm\*cm. For better conductivity, an additional annealing process needs to be conducted. As reported [16], the electrical conductivity of SiCN material changes drastically with annealing conditioning. Therefore, in our heat treatment, to obtain the proper conductivity of SiCN for RTD application, the annealing process is regarded as a crucial step. Early studies also have shown that the SiCN can have various electrical conductivities depending on the annealing temperature, time, and atmosphere during heat

treatment [20], [21]. As an atmosphere, nitrogen ( $N_2$ ) gas, an inert gas, is the most frequently used gas during the heat treatment to obtain a desired electrical conductivity of PDC SiCN.

### 2.2.3.1. *Process of heat treatments*

Hence, our heat treatments consist of three steps: cross-linking, pyrolyzing, and annealing. The treatments are performed in a GSL1600X Vacuum and Gas Tube Furnace (MTI Corporation, USA) shown in Figure 2.10 (a) which is able to program the temperature and time for heat treatment. The nitrogen gas ( $N_2$ ) flows during the entire heat treatment processes. The flow rate of nitrogen gas in the tube is also programmed by the Mass Flow Controller (MKS Instruments Inc. USA) as shown in Figure 2.10 (b). For this study, the atmosphere and the flow rate are fixed as nitrogen and at the rate of 150 sccm.



(a)



(b)

**Figure 2.10 Gas Tube Furnace for heat treatment (a) and Mass flow controller (b)**

Figure 2.11 shows the entire temperature change and process duration of the heat treatments. The heat treatments start by placing the shaped polymer structures on an alumina plate, and then the plate is inserted into the furnace. The temperature is first raised to 400°C at the rate of 2.5°C/min for cross-linking. The crosslinking was performed for 3 hours. Following the cross-linking, the temperature is increased up to 1100 °C at the rate of 2.5°C/min, and kept stable for 3 hours for pyrolyzing. After the pyrolyzing, the temperature is increased up to 1400 °C at the rate of 2.5°C/min, and kept stable for 25 hours for annealing. Finally, the temperature is cooled down to 0°C at the rate of 2.5°C/min.

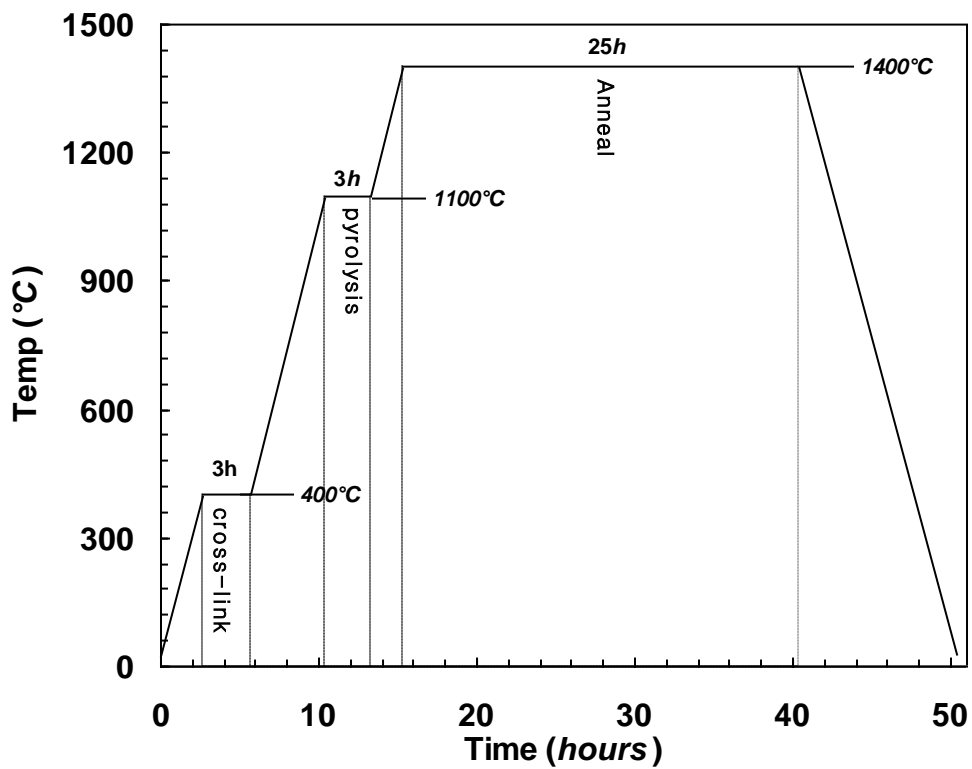


**Figure 2.11 Heat treatment processes**

As reported in previous work [1], [2], [5], [11], the polymer structures are thermally decomposed into amorphous SiCN during the pyrolyzing process. The annealing process is the most important stage for the already pyrolyzed SiCN to obtain more electrical conductivity. As shown in an early study, one can control the electrical

conductivity by changing the annealing time and temperature. Therefore, we chose the annealing time of 25 hours to provide sufficient conductivity to our sensors. We must make sure that the highly pure nitrogen gas flows throughout these heat treatments. Following the heat treatment in the furnace, conductive amorphous SiCN samples are taken out of the furnace.

### ***2.2.3.2. Effect of the state of solidity before heat treatment***

One must make sure that the patterns have completely solidified before applying heat treatments. If the PDCs are not completely solidified before the heat treatments, the PDCs can be easily broken during the heat treatments as shown in Figure 2.12. The patterned precursors are completely solidified by additional UV exposure after developing the PDC patterns. Besides additional UV exposure, the patterned precursors are placed overnight at room temperature before starting the heat treatments.

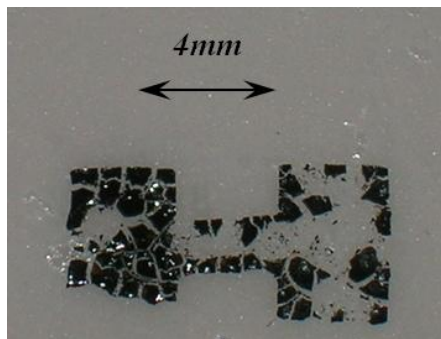


**Figure 2.12 Effect of the state of solidity before heat treatment**

Figure 2.13 shows the successfully heat-treated PDC SiCN taken from the furnace. Various sizes and shapes of PDC SiCN can be successfully obtained from the direct

contact lithography and the configurations for the heat treatment. In appearance, it has a shiny and slippery surface as well as black in color.

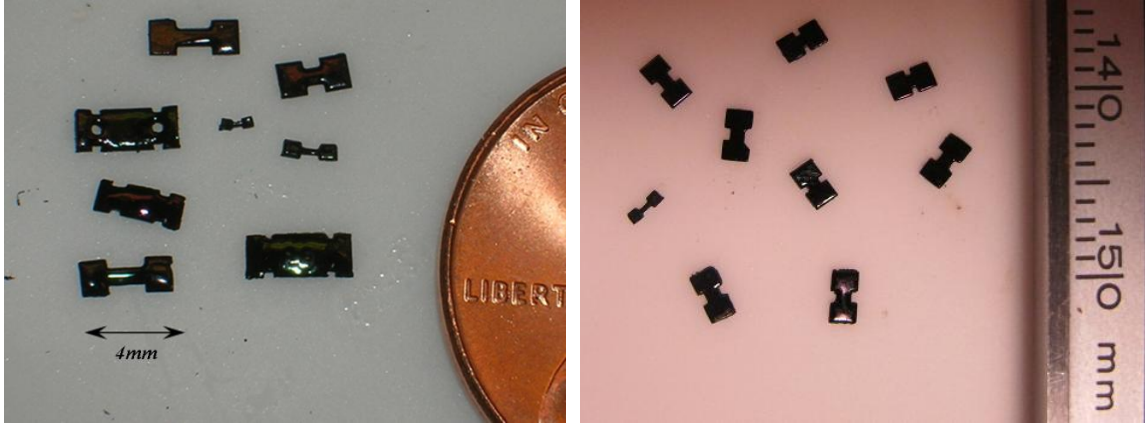


**Figure 2.13 Completed free standing SiCNs**

### **2.3. Result and conclusions**

In this chapter, a fabrication process for free standing amorphous SiCN ceramics was described. A novel direct contact lithography technique has been introduced to make a well defined pattern directly on a transparent Teflon film or photo mask. In our photolithography, the direct-contact method of UV exposure between photomask and precursor was employed to obtain a pattern with high quality resolution. Using the direct contact method, we can simplify the PDC fabrication process of photo-polymerization, a process that usually omits the spincoating process of the polymer precursor. In addition, the thickness of the patterns can be adjusted by the exposure time since the thickness of the pattern shows a predictable relation to UV exposure time. To facilitate the peeling-off of the pattern from the substrates, additional UV exposure, which results in a hardening

of both the upper and bottom part of the pattern, was conducted in our experiment after the acetone etching.

A heat treatment process was performed in a tube furnace with pure nitrogen gas flow. Besides pyrolyzing the samples for making SiCN, an annealing process was added, which imparts the proper electrical conductivity to amorphous SiCN and it will be used for the next step of our experiment for high temperature RTDs and heat flux sensors. The characterization of a fabricated SiCN RTD is described in the next chapter.

## Chapter 3

### CHARACTERIZATION OF PDC SiCN MATERIAL

#### 3.1. Introduction

In previous studies on the characteristics of PDC SiCN, various mechanical and electrical characteristics of PDC SiCN such as shear strength, insulation resistance and breakdown voltages were measured under various heat treatment conditions [33]. Additionally, some oxidation experiments on SiAlCN were performed [37]. For sure, these experiments can provide helpful information for our own PDC SiCN study. However, the characteristics of SiCN are basically dependent on the fabrication conditions such as polymer synthesis, a high temperature furnace and heat treatment processing. Our atmosphere and fabrication conditions are different from those in other experiments. Therefore, the characteristics of our own SiCN material need to be investigated.

In this chapter, we investigate the characteristics of the amorphous SiCN material that we fabricated as described in the previous chapter. We examine the following issues: 1) crystallinity and oxidation, 2) composition and elemental analysis, 3) the electrical conductivity over the elevated temperature. The X-ray Diffraction (XRD) analysis is carried out to determine the degree of crystallinity of the SiCN, which eventually shows if the sample SiCN material is really amorphous or not. Some Scanning Electron Microscope (SEM) images are taken to view the surface and cross-section of the SiCN

material. EDS analysis is also conducted to distinguish the elemental difference from the cross-section of the SiCN sample and to compare the elemental composition before and after oxidation. Besides these observations, the most important part of the characterization of our SiCN material is to get electrical conductivity at different temperature because ultimately SiCN material will be used to make RTD temperature sensors and Heat Flux Sensors. To do that, an RTD sensor with an electric connection will be fabricated first and then a measurement of resistance during the temperature increase will be done to determine the relation between temperature and resistance for each free standing SiCN RTD sensor.

## **3.2. Characterization of SiCN**

### **3.2.1. XRD analysis of SiCN**

#### ***3.2.1.1. Experiment preparation***

X-ray Diffraction (XRD) analysis was used in order to see if our SiCN samples were amorphous or not. XRD (Phillips X-pert, USA) is the most common method for determining the arrangement of atoms within a crystal. Three different SiCN RTDs samples were prepared. They were annealed at different temperatures, which were 1200°C, 1300°C and 1400°C respectively. Other than annealing temperature, the other conditions are identical. Our goal was to see if there was any difference in crystallization in those samples compared to the results of previous study.

### 3.2.1.2. Results

According to previous studies [15], [21] and the data sheet from the manufacturer, KiON company regarding the characteristics of SiCN, there is almost no crystallization up to 1400°C after annealing or pyrolysis in the range of 1100°C ~ 1400°C as shown in Figure 3.1. So when it is heat-treated at temperatures less than 1400°C, SiCN is mostly amorphous even though the sample undergoes the annealing process.

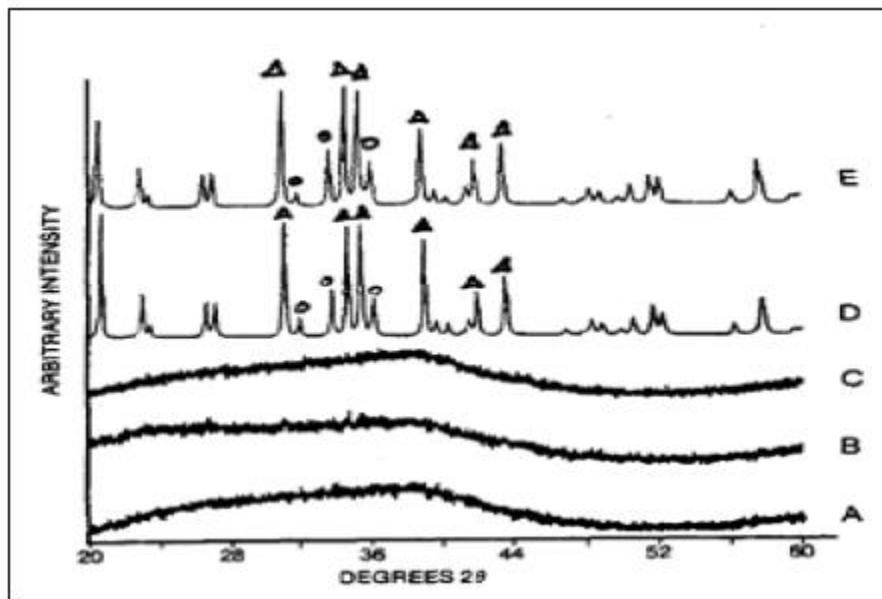


**Figure 3.1 XRD patterns of polyureasilazane pyrolyzed to: (A) 1200°C, (B) 1300°C, (C) 1400°C, (D) 1500°C, (E) 1600°C under Nitrogen  
(Source: Data sheet from KiON)**

Figure 3.2 shows the results from our analysis. It was observed that for 1200°C and 1300°C samples, no peak was found. But in case of the RTD annealed at 1400°C, the peak was found in one place with a small amount of intensity. That means there is initiation of crystallization at 1400°C in the annealed sample. But for the larger part of

the graph, it can be considered to be an amorphous material. These behaviors indicate that our SiCN PDC sensors are generally amorphous.

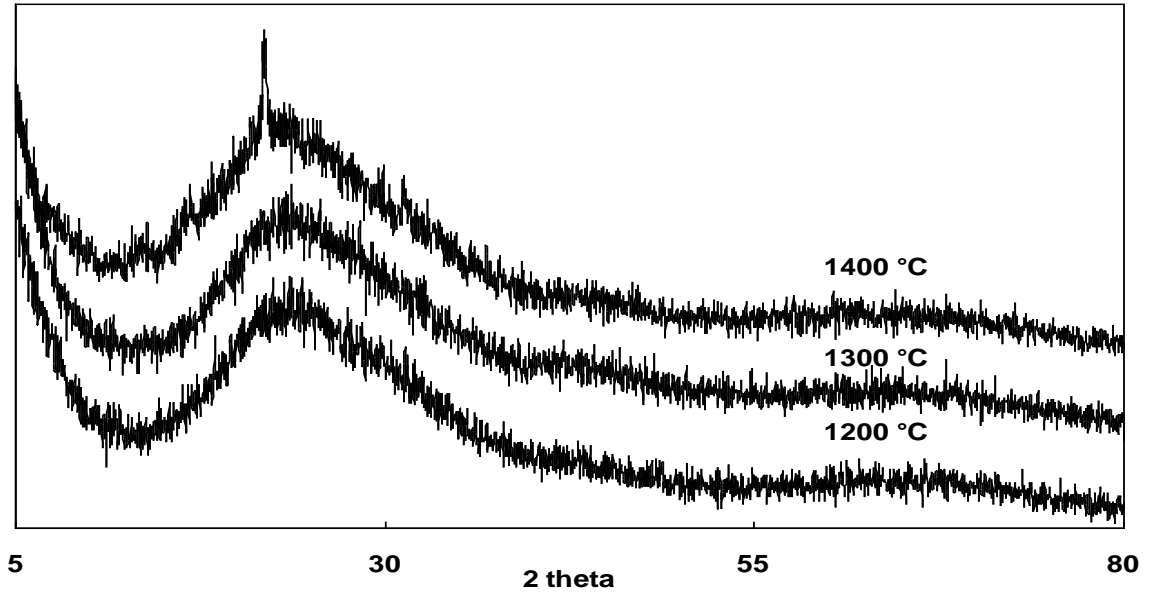


**Figure 3.2 XRD patterns of RTDs annealed at 1200 °C, 1300 °C, and 1400 °C for 25 hours respectively**

### **3.2.2. Oxidation Test of SiCN**

#### **3.2.2.1. Sample preparation**

Three SiCN samples are randomly taken from a group of our SiCNs which are fabricated under the same conditions. Annealing temperature and time are 1400°C and 25 hours respectively. The samples are cut into two pieces and then they are placed in a high temperature furnace at 1000°C for 4 hours and in the open air of the laboratory to oxidize the samples. To compare the elemental difference between before and after the oxidation, the EDS analysis was employed for each sample. As shown in Figure 3.3, three points

along the depth in sample are selected, and the weight percent of each element is measured for each point.

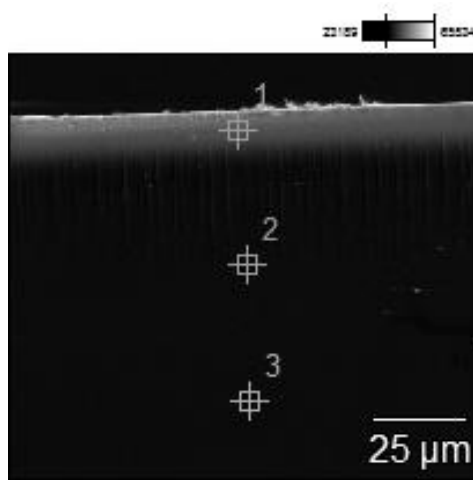
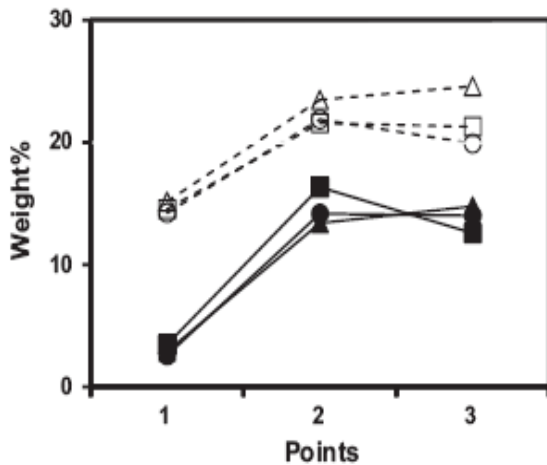


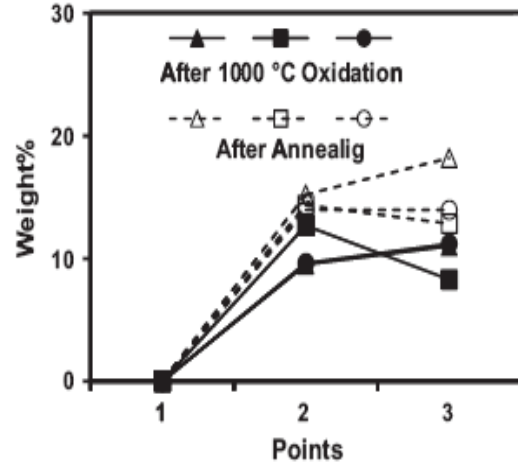
**Figure 3.3 SEM image showing the location points used for EDS analysis.**

#### **3.2.2.2. Results**

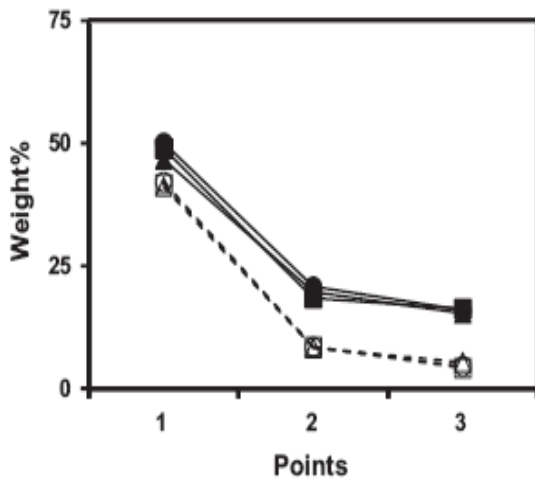
The change of weight percent of 4 primary elements, carbon, nitrogen, oxygen and silicon, are plotted for our just annealed samples and oxidized samples in Figure 3.4. It shows that just after annealing, the surface of the samples (Point 1) is rich in oxygen and depleted in carbon, nitrogen, and silicon as compared to the deeper part of the samples (Points 2 and 3). After oxidation at 1000°C for 4 hours, both the surface and bulk of the sample exhibits an increase in oxygen as compared to the annealed sample. The concentrations of carbon and nitrogen get lower after oxidation, whereas the concentration of silicon exhibits less change after oxidation. It was found that the weight percent of oxygen at the surface was higher than that of the inside bulk, and after oxidation, the weight percent of oxygen increased by the amount of about 5~10 % over the point #1, #2, #3 in the sample.



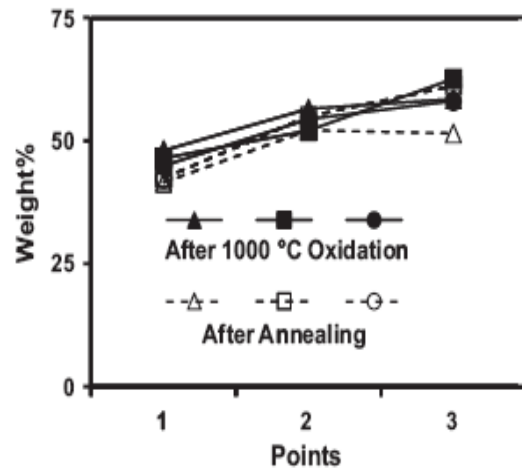
(a) Carbon



(b) Nitrogen



(c) Oxygen



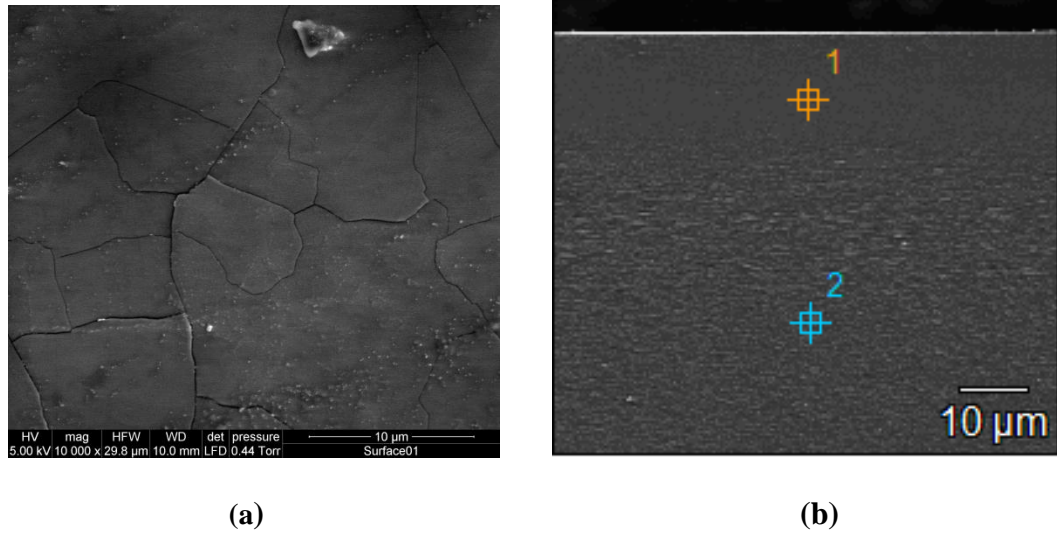
(d) Silicon

Figure 3.4 Composition of RTDs by EDS after annealing and after oxidation

### 3.2.3. Composition analysis by SEM/EDS

From the SEM images of surface and bulk images of SiCN shown in Figure 3.5 (a), the surface of SiCN looks very rough and has cracks on it, which are caused by the shrinkage of the surface owing to the high shrinkage rate of polyureasilazane after heat treatment. Also from the cross-section image in Figure 3.5 (b), it was observed that there

is a thin layer of about 20 $\mu\text{m}$  right under the surface of SiCN RTD, which is thought to be an oxygen-rich layer because of oxygen possibly leaking into the tube furnace during heat treatment.

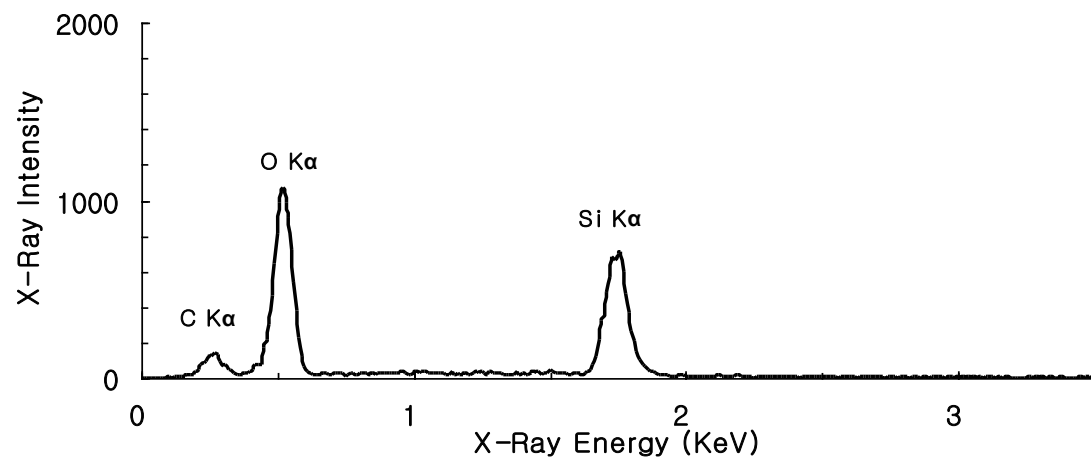


**Figure 3.5 SEM images of RTD (a) surface and (b) bulk**

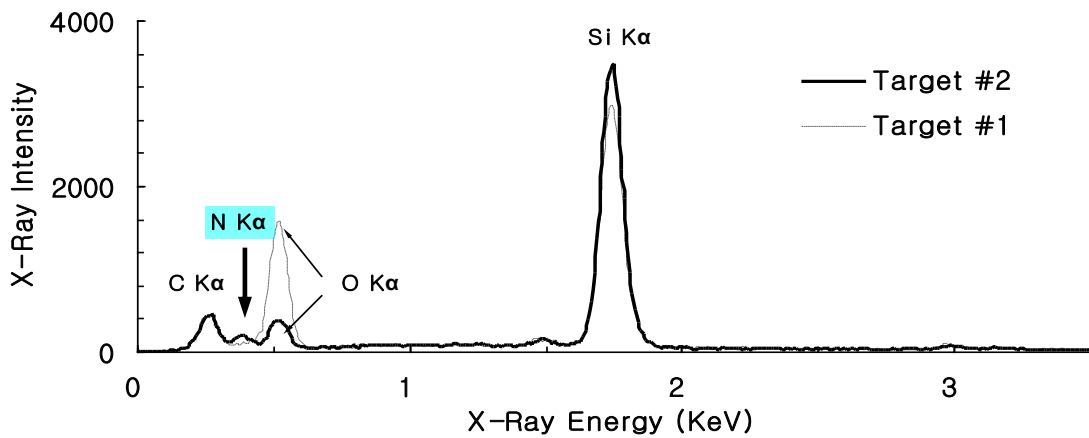
To detect the elemental difference between the surface and interior layer, further analysis of EDS was conducted. From the result shown in Figure 3.6, an elemental difference can be seen in two different areas, the surface layer (target #1) and the bulk layer (target #2). Figure 3.6 (a) shows that the amount of oxygen is largest among the elements comprising the amorphous SiCN ceramic material and that nitrogen was not detected at the surface of SiCN RTD.

On the other hand, the amount of oxygen in the bulk is significantly reduced. Additionally, the amount of nitrogen and silicon is increased noticeably as shown in Figure 3.6 (b), and the amount of carbon remains the same as that of the surface. Therefore it can be presumed that at the surface, there is a significant amount of oxidation

because of the leakage of the atmosphere containing oxygen into the gas tube. The element of silicon also decreased due to some sort of chemical reaction during heat treatment. However, the bulk part under 20um from the surface, considered as amorphous SiCN, contains all the elements comprising SiCN material. Hence for the measurement of electrical conductivity of our amorphous SiCN, the bulk part should be considered as the primary part for the electric connection rather than surface layer.



(a)



(b)

**Figure 3.6** The result of EDS analysis for the two targeted points; (a) surface (target #1 and (b) bulk (target #2)

### **3.2.4. Depth dependence of composition of PDC SiCN**

Further composition analyses of our SiCN were conducted. An EDS linescanning method was employed. From the linescanning method, a continuing distribution of elements in the sample can be obtained in the form of a line over the cross section in the sample. We conducted EDS linescanning for three different SiCN RTDs to examine if the elemental difference over the cross-section is still identical to other places in the cross section and if the pattern of element distribution is similar to other SiCN RTDs.

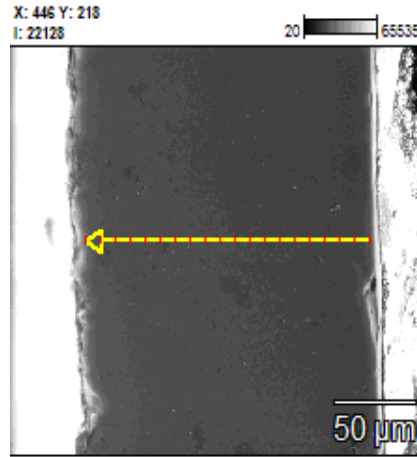
#### **3.2.4.1. *Sample preparation***

Three different types of samples were prepared. They were annealed at different temperatures, which are 1200°C, 1300°C and 1400°C. One sample was picked from three types of samples. Selected samples were cut into half and then the cross-section area was polished for EDS linescanning.

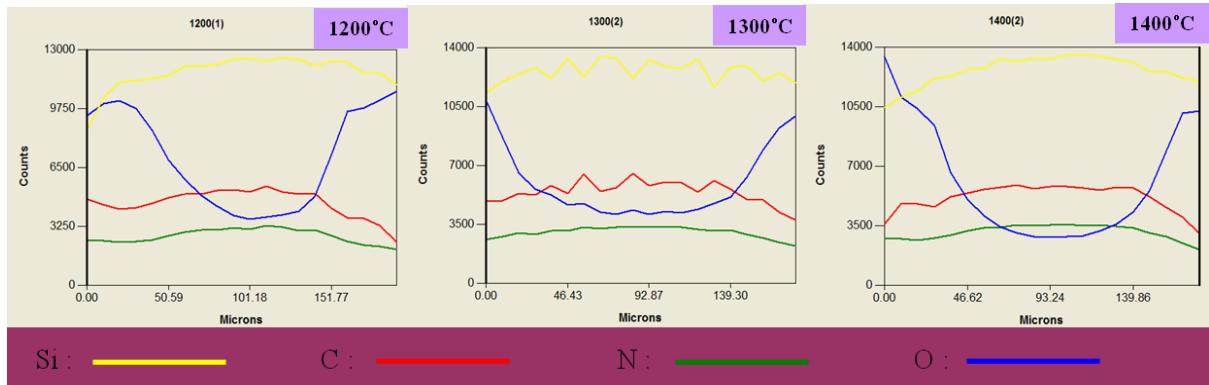
#### **3.2.4.2. *Results***

The linescanning over the 200  $\mu\text{m}$  thickness for each sample is shown in Figure 3.7. Basically all samples showed the same pattern as we expected from the result of EDS point analysis. The amount of oxygen is highest at both surface regions having “U” shape and is lowest at the center. There are several reasons for the high concentration of oxygen at the surface. It comes from oxidation of the surface area due to a very small amount of atmosphere leakage into the furnace during heat treatment as mentioned in the composition analysis section. Another possibility is oxidization during photolithography since Si tends to be oxidized easily in an ambient atmosphere. However, as it enters the

sample, the amount of oxygen decreases due to the extremely low exposure to oxygen in the center of our SiCN RTD.



(a)



(b)

**Figure 3.7 Plots from EDS Linescanning over cross-section of samples**

Another noticeable point in these results is that the SiCN RTD of 1400°C annealing temperature has the highest concentration of oxygen at the surface layer among the three different SiCN RTDs while the other three major elements which are nitrogen, carbon, silicon stay almost the same over the three different SiCN RTDs. Also the amount of oxygen at the surface of the 1300°C sample is higher than that of the 1200°C

sample. This is because more oxidation takes place when SiCN RTD is exposed to the higher temperature during heat treatment.

### 3.3. Electrical resistance of amorphous PDC SiCN

According to Haluschka et al [16], annealing temperature, time and atmosphere during the heat treatment are three major factors that affect the electrical conductivity of the final SiCN material. Figure 3.8 shows the dependency of electrical conductivity on annealing temperature and time [16].

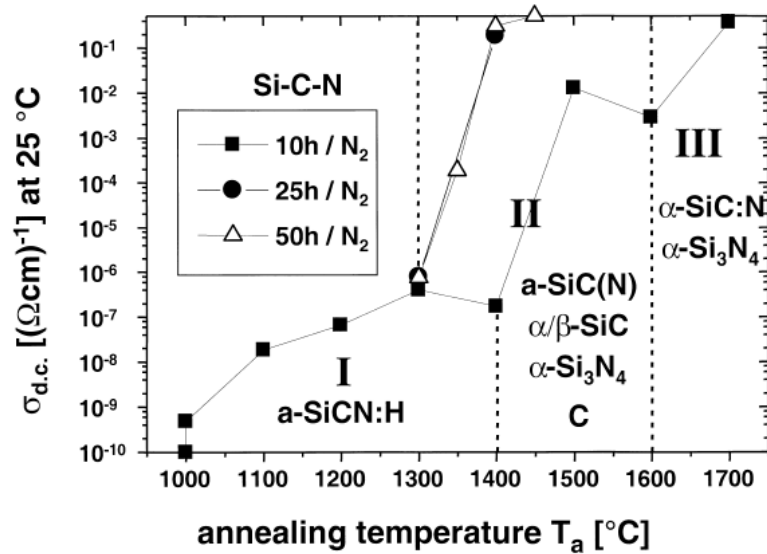


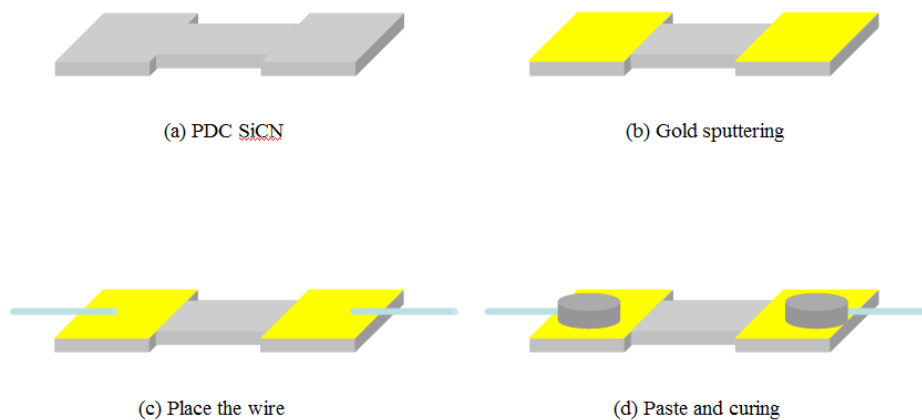
**Figure 3.8 Electrical conductivity of amorphous SiCN depending on annealing time and temperature (Source : Haluschka et al [16])**

Without annealing, it is impractical to use amorphous SiCN as an RTD sensor due to its very high resistance at room temperature. Therefore, it needs to go through the annealing process to find the optimal electrical conductivity for our RTD sensor. During

annealing, we fixed annealing time and atmosphere, but instead, changed the annealing temperature. Three different annealing temperatures were chosen for our investigation, which are 1200°C, 1300°C and 1400°C. Thus, the SiCN samples going through these three different annealing temperatures were investigated to obtain the relationship between temperature and electrical resistance so that we could see the effect of annealing temperature and electrical conductivity on SiCN material.

### 3.3.1. Measurement setup of free standing SiCN

For the measurement of electrical resistance of the free standing SiCN RTD, first the electric connection between both ends of dog-bone shaped SiCN RTD and copper wire needs to be solid and robust. The process of making the connection is shown in Figure 3.9. The sputtering of gold on both ends of SiCN is conducted by sputtering machine to the thickness of 150nm and then a silver paste (Conductive Silver paint, SPI) and the electric wire are placed on both ends of SiCN RTD followed by the cure of the conductive adhesive at 80°C for 2 hours. The pictures of gold sputtering and connection are shown in Figure 3.9 (b), (c).



(a)

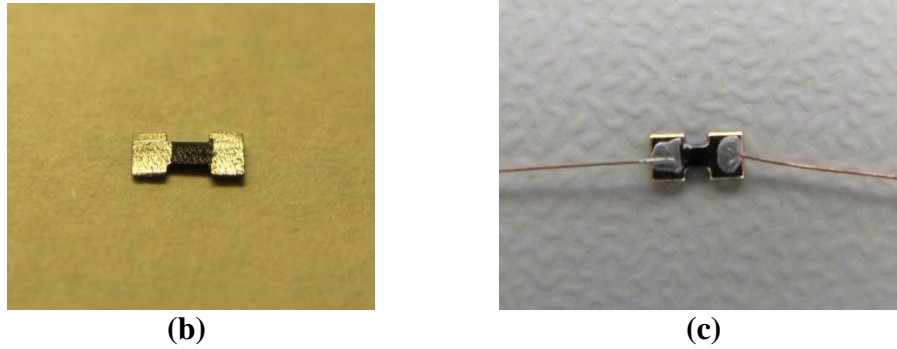


**Figure 3.9 The process and picture of making electric connection**

To measure electrical resistance for SiCN RTD, the fabricated SiCN RTD is placed on a hot plate, as shown in Figure 3.10. The copper wires from both ends of SiCN RTD were connected to the Fluke 45 multi-meter to measure the value of resistance. Then, the thermocouple was placed as close as possible to the SiCN RTD and connected to the data acquisition system (NI, USA) to obtain the temperature of the RTD sensor. The resistance value from Fluke 45 and the temperature value from the data acquisition system were combined with the software program which is Lab View. Therefore simultaneous values of resistance and temperature, which is the relation between resistance and temperature, could be recorded in the Lab View program automatically as the temperature of the hot plate increased.

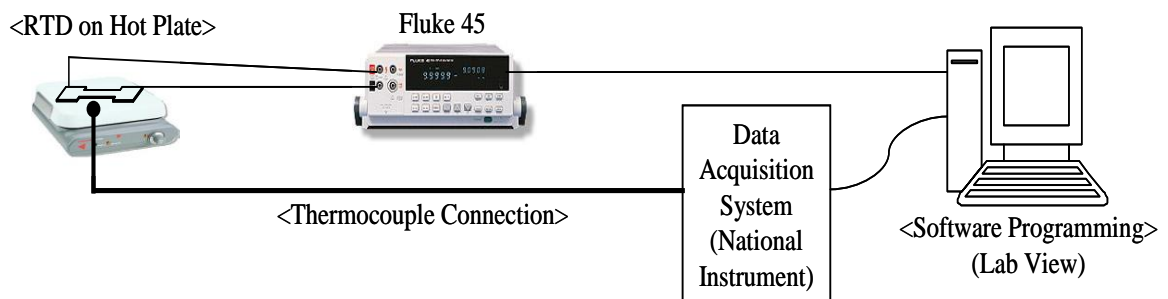


**Figure 3.10 The system for measuring electrical resistance of SiCN RTD**

The resistance change of SiCN RTD with temperature changes was measured for three different RTDs fabricated from three different annealing temperatures, 1200°C, 1300°C, 1400°C respectively. Other conditions of fabrication were identical. 4 SiCN RTDs were fabricated for each annealing temperature and measured in the configuration of Figure 3.10.

### **3.3.2. Analysis on resistance difference between surface and bulk**

Through a number of measurements of the electrical resistance of PDC SiCN, we found that the electrical resistivity of surface of SiCN is significantly different from that of bulk SiCN. It seemed that the resistance of the surface was always much higher than that of bulk area of SiCN RTD. As we expected from the result of our composition analysis over the cross section of SiCN RTD, it is because of the composition difference between the surface and bulk area. To verify the electrical resistance difference, additional experiments were as follows.

#### **3.3.2.1. *Sample preparation***

Two groups of SiCN RTDs are prepared after both groups went through same heat treatment process with 1400°C and 25 hrs of annealing temperature and time. Each group has 3 different samples. First group is connected with copper wires directly to the surface of RTD and the other is connected to the bulk area, after grinding both edges, to make contact with bulk region of RTD. Then resistance of RTD was measured from room temperature to about 400°C after it is placed on hot plate and connected to data acquisition system.

### 3.3.2.2. Results

The results are shown in Figure 3.11. The resistance changes in terms of temperature are quite different depending on the connecting location of the wires. It can be seen that in case where wires are connected at the surface of the RTD, the values of resistance are 35.8 ~ 64 K $\Omega$  at room temperature. However, the values of resistance drop to 3.5 ~ 6.1 K $\Omega$  when the wires are connected to the bulk area of the RTD, which is much smaller than surface contact by an order of magnitude. In addition, the bulk connection shows a much smaller range of the resistance over the three samples, while samples with the bulk connection have a wider range of resistance. The drop-down pattern of resistance of the surface contact RTD looks rough, which means it is hard to calibrate the temperature with resistance and is not suitable for an RTD sensor. In consequence, for the RTD use of our amorphous SiCN, an interior connection is recommended for an electrical connection rather than a surface connection.

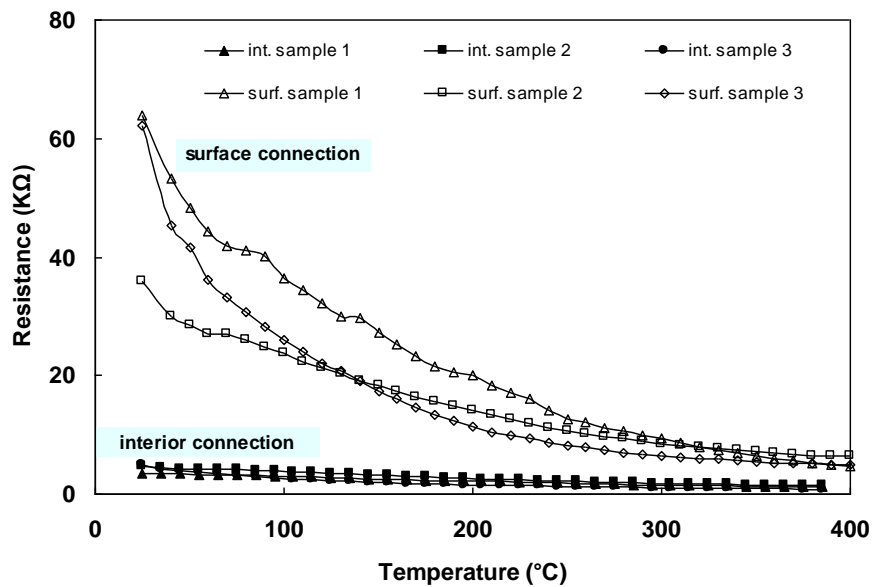


**Figure 3.11 Resistance difference depending on connection conditions, surface and bulk connections.**

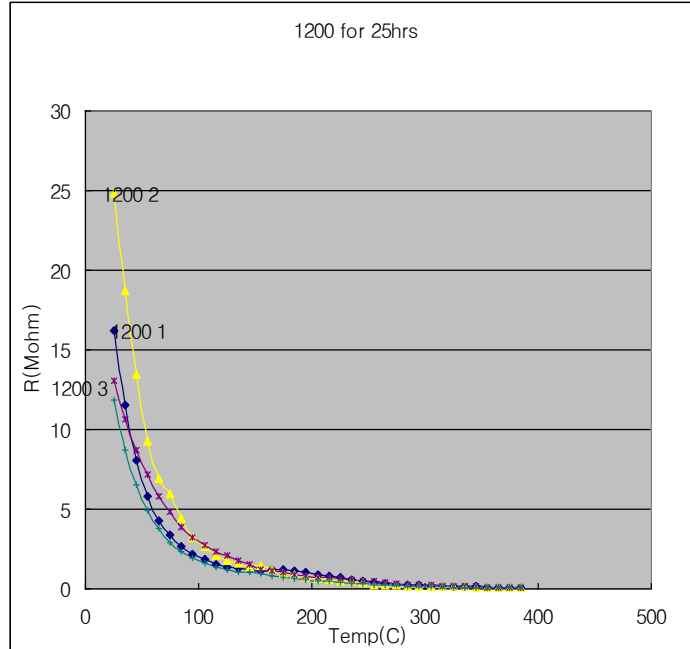
### 3.3.3. Effect of annealing temperature on electric resistance

#### 3.3.3.1. *Sample preparation*

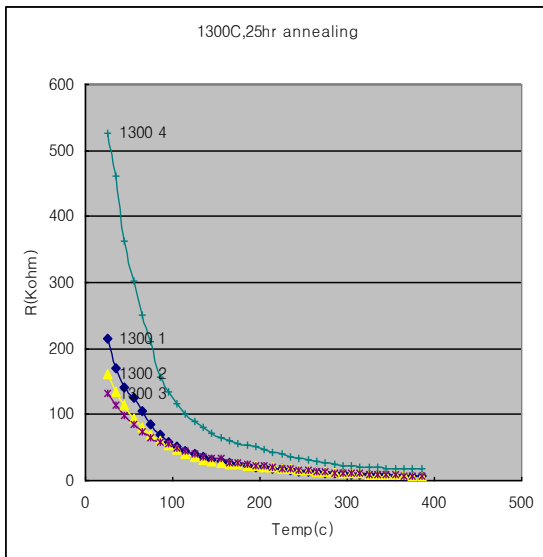
Three groups of SiCN RTDs were prepared after each group went through a different heat treatment process. They were annealed at different temperatures of 1200°C, 1300°C and 1400°C and for a period of 25 annealing hours. Each group had 4 different samples. And then the resistance of the RTD was measured from room temperature to about 400°C after it was placed on a hot plate and connected to the data acquisition system.

#### 3.3.3.2. *Results*

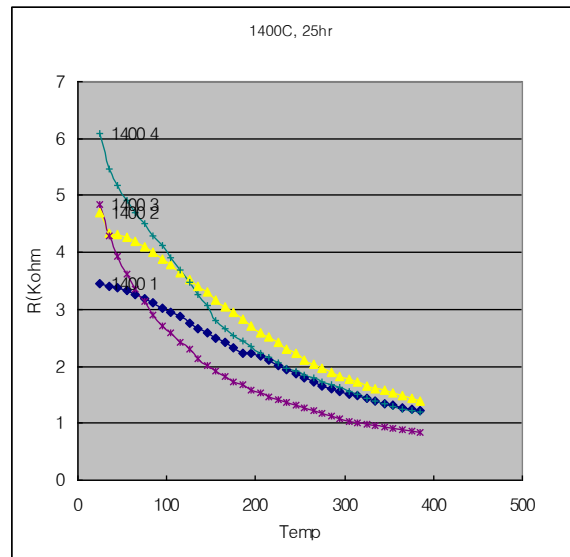
Figure 3.12 shows the results of the electrical resistance of our RTD with the increasing temperature on the hot plate. The resistance value of SiCN RTD from 1200°C, 25 hrs annealing ranges from 11 to 24Mohms ( $2.81E-6 \text{ (ohm*cm)}^{-1} \sim 1.34E-6 \text{ (ohm*cm)}^{-1}$  in resistivity) at room temperature. As the temperature rises to 400°C, the resistance of SiCN RTD decreases significantly. All 4 SiCN RTD show a similar pattern of decreased resistance with higher temperatures. The 4 SiCN RTDs were heated to 1300°C, for 25hrs and the range of resistance was 131Kohm  $\sim$  527Kohm ( $6.33E-5 \text{ (ohm*cm)}^{-1} \sim 1.56E-4 \text{ (ohm*cm)}^{-1}$  in resistivity) at room temperature. Also 4 SiCN RTDs from 1400°C annealing temperature were measured resulting in 3Kohm  $\sim$  6Kohm ( $9.63E-3 \text{ (ohm*cm)}^{-1} \sim 5.47E-4 \text{ (ohm*cm)}^{-1}$  in resistivity) at room temperature and showed a similar drop-down pattern as other RTDs.



(a)



(b)



(c)

**Figure 3.12 Resistance vs. Temperature for three different RTDs; (a) 1200°C, (b) 1300°C, (c) 1400°C for annealing temperature.**

When the electrical resistances of 3 different SiCN RTDs are compared, it is clearly found that the resistivity decreases with an annealing temperature from 1200°C to

1400°C. As shown in Figure 3.13, one can see by simply looking at the resistances in common logarithm over the elevating temperature to about 400°C of 3 different groups that there is clear distinction among the three groups. Our experiment results reveal that the electrical conductivity of SiCN significantly depends on the annealing temperature in some patterns just as in a previous experiment by Haluschka et al [16]. And it turned out that our amorphous SiCN can be used as a successful material for use as an RTD sensor.

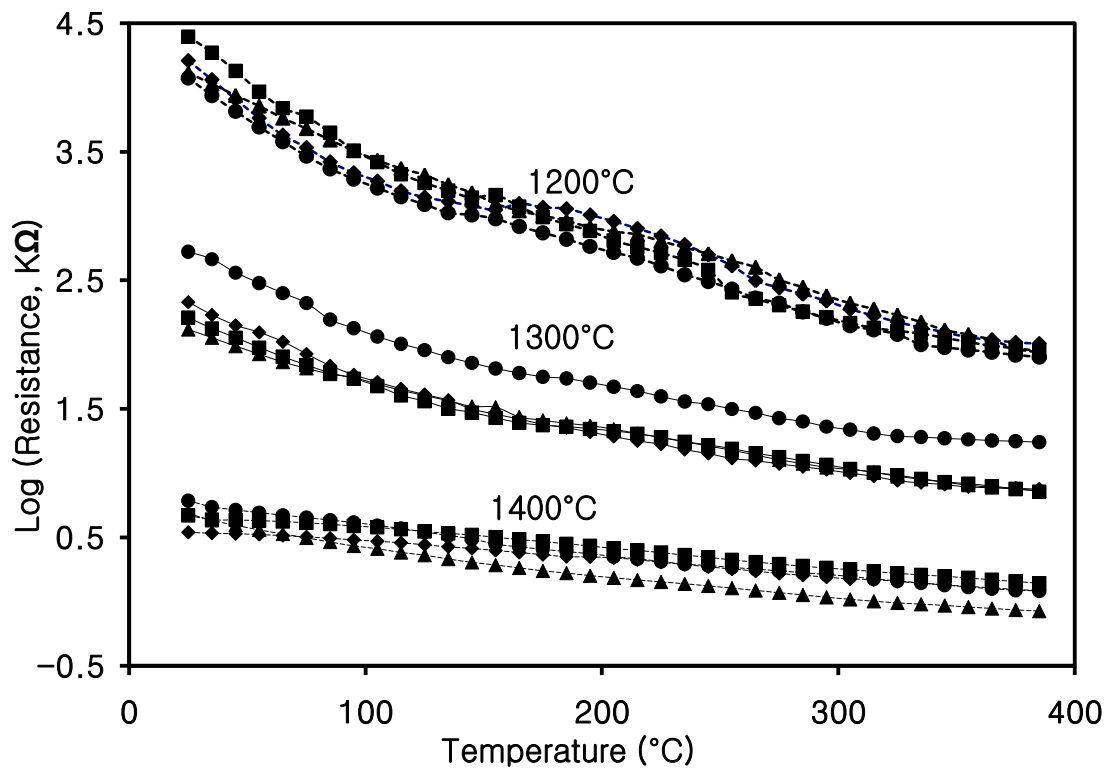


Figure 3.13 In one plot after taking log for resistance

### 3.4. RTD Curve

The Steinhart-Hart equation is a widely used third order approximation of the resistance of a semiconductor at different temperatures [40]. Since our amorphous SiCN

RTD also shows semiconducting electrical properties, it is possible to express our plots in Figure 3.13 in the form of Steinhart-Hart equation:

$$\frac{1}{T} = a + b \ln(R) + c \ln^3(R) \quad (3.1)$$

where T is temperature in Kelvin, R is resistance at T in ohms. And a, b, c are Steinhart-Hart coefficients.

For sure, Steinhart-Hart coefficients vary depending on the type and model of the RTD or thermistor and the temperature range of interest. Figure 3.14 shows the typical curve of a Steinhart-Hart equation with the coefficient of  $a = 1.40 \times 10^{-3}$ ,  $b = 2.37 \times 10^{-4}$ ,  $c = 9.90 \times 10^{-8}$ .

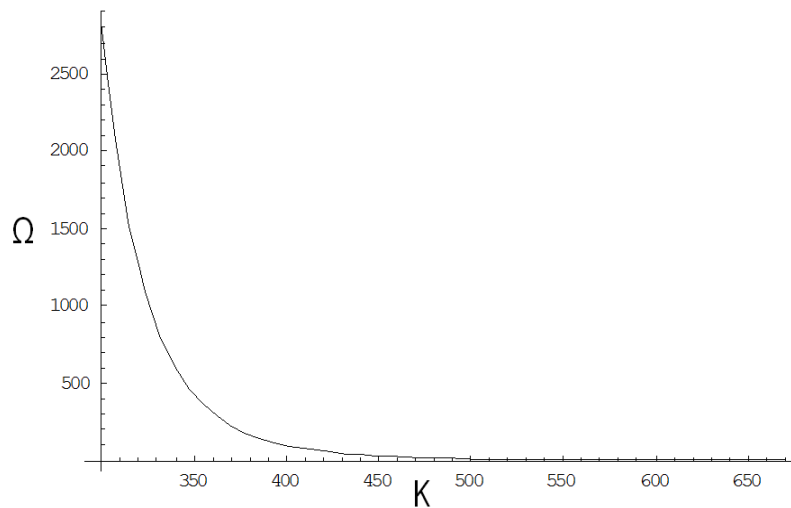


**Figure 3.14 Typical curve of Steinhart-Hart equation**

Generally, the coefficients a, b, c are decided for individual thermistors or RTDs in a particular range. To get the coefficients, three different temperature points are selected to apply to the equation; usually at the lower end, the middle and high end of the curve. These three points ensure the best fit in the temperature range. Actually the smaller

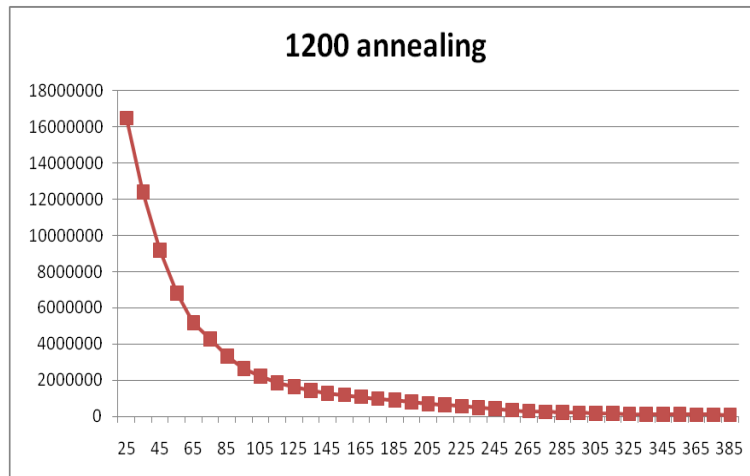
the range is, the better the Steinhart-Hart equation will match the measured data. These three accurately measured data of temperature and associated resistance are substituted into the equation to establish these three equations having coefficients a, b, c as follows:

$$\frac{1}{T_1} = a + b(\ln(R_1)) + c(\ln(R_1))^3 \quad (3.2)$$

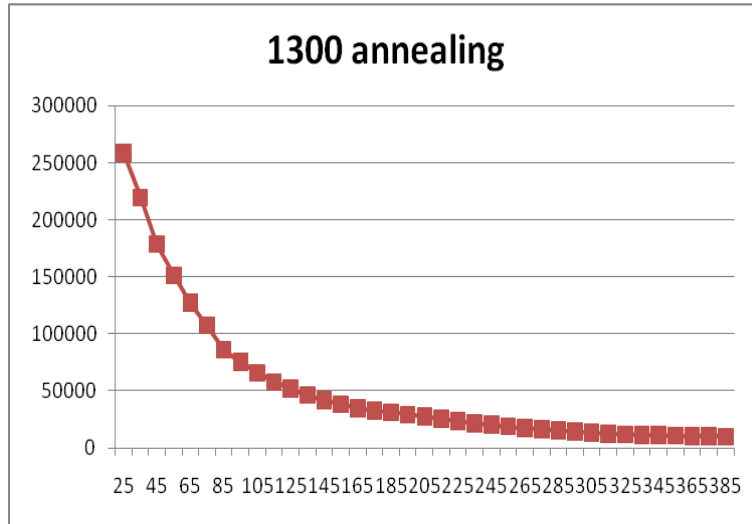
$$\frac{1}{T_2} = a + b(\ln(R_2)) + c(\ln(R_2))^3 \quad (3.3)$$

$$\frac{1}{T_3} = a + b(\ln(R_3)) + c(\ln(R_3))^3 \quad (3.4)$$

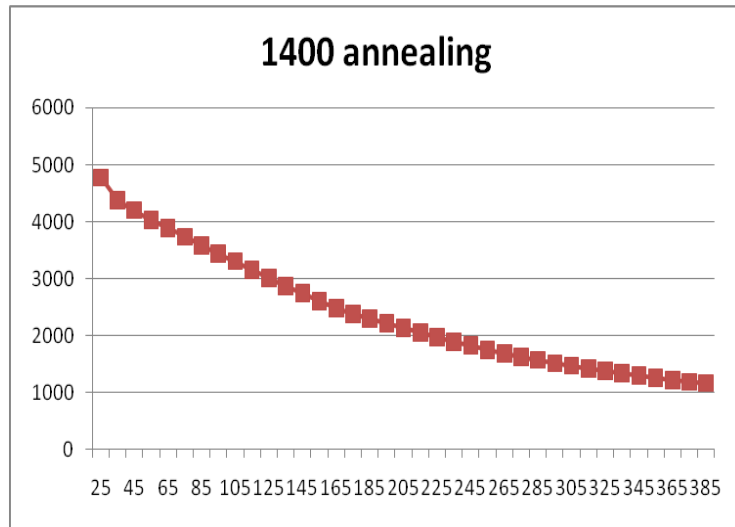
As shown in Figure 3.13, there are three different types of curves which are from 1200°C, 1300°C and 1400°C annealing temperatures. In each type, 4 individual RTDs show the relation between temperature and associated resistance. Therefore, each annealing temperature has to get 4 different Steinhart-Hart equations. However, in this chapter, just one measurement data is used to get one set of a, b, c coefficients of the Steinhart-Hart equation. So, the data from 4 individual SiCN RTD are combined into one data entry after one average resistance value is calculated over the temperature range.



(a)  $a = -4.28 \times 10^{-3}$ ,  $b = 5.28 \times 10^{-4}$ ,  $c = -2.56 \times 10^{-7}$



(b)  $a = -7.07 \times 10^{-3}$ ,  $b = 1.04 \times 10^{-3}$ ,  $c = -1.38 \times 10^{-6}$



(c)  $a = 3.38 \times 10^{-2}$ ,  $b = -6.69 \times 10^{-3}$ ,  $c = -4.33 \times 10^{-5}$

**Figure 3.15 Steinhart-hart coefficients of three types of SiCN RTD**

Three different points are selected from points in each curve (the lower end, middle end and high end) followed by substitution into the equation. Figure 3.15 shows the results of the calculation of coefficients and the plots over three different annealing temperatures.

### 3.5. Conclusion

The characterization studies which have been done in this chapter can be summarized as following:

- From the X-ray diffraction test, our SiCN samples turned out to be amorphous material and started to be crystallized from the 1400°C annealing temperature.
- From the oxidation test, both the surface and bulk of the sample exhibited an increase in oxygen as compared to the annealed sample. The concentrations of carbon and nitrogen got lower after oxidation, whereas the concentration of silicon exhibited less change after oxidation.
- The relation of resistance and temperature for the 3 SiCN RTDs that have different annealing temperatures was measured. It revealed that the higher annealing temperature produces more conductive SiCN material than other research results.
- The resistance difference between the surface and bulk area of SiCN RTD was investigated using SEM and EDS analysis showing that the bulk area makes it more conductive and gives a stable resistance-temperature relation at elevating temperatures.
- For the calibration of our measurement of temperature and resistance, the Steinhart-Hart equation was employed and the coefficients of the equation were calculated from the three data points.

Based on these characterization studies, we have good reference material for making an optimal SiCN RTD sensor that will be used for our Heat Flux Sensor (HFS) in a later chapter. Obviously rather than a surface contact with the wire, the bulk connection will be chosen for our SiCN RTD sensor. Also an optimal annealing temperature will be selected for the RTD sensor as well.

## Chapter 4

### FABRICATION OF PDC RTD ON A SUBSTRATE

#### 4.1. Introduction

The Si based pre-ceramic precursors such as Polysilazanes, polycarbosilanes, and polysiloxanes have been good source materials for PDC products such as ceramic fibers, coatings, and matrixes for ceramic composites. However, the basic limitation of polymer derived ceramics is the extraordinary high shrinkage rate of up to 40% shown in Figure 4.1 (a) and porosity during polymer to ceramic conversion. The significant shrinkage restricts the usability of this material's application. Especially, when one tries to make a SiCN structure on some substrates, it is almost impossible to keep it in the same shape after high temperature pyrolysis or the annealing process due to the high stress between substrate and SiCN film [11], [24], [25] as shown in Figure 4.1 (b).

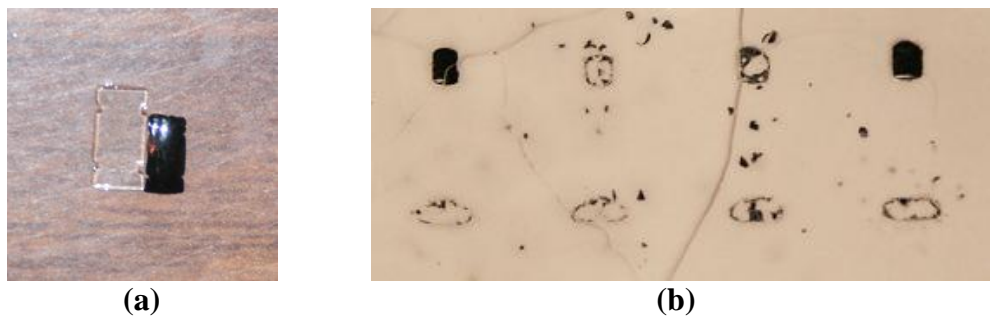


**Figure 4.1 Pictures of (a) shrinkage rate and (b) failure on substrate**

It was reported by Greil et al [41], [42] that the shrinkage problem of SiCN can be pronouncedly eliminated by adding active fillers (B, Si, Al, Ti, Mo, etc) into the polymer

precursor. According to this Active Filler Controlled Pyrolysis (AFCOP) method, during pyrolysis, active filler powders react with the decomposition products or a reactive atmosphere to form a new phase shown in Figure 4.2 (b). There exists a volume expansion from this reaction, which leads to compensation for the polymer shrinkage. In some studies, it was found that a near-net-shape polymer to ceramic conversion can be achieved by this active filler pyrolysis method.

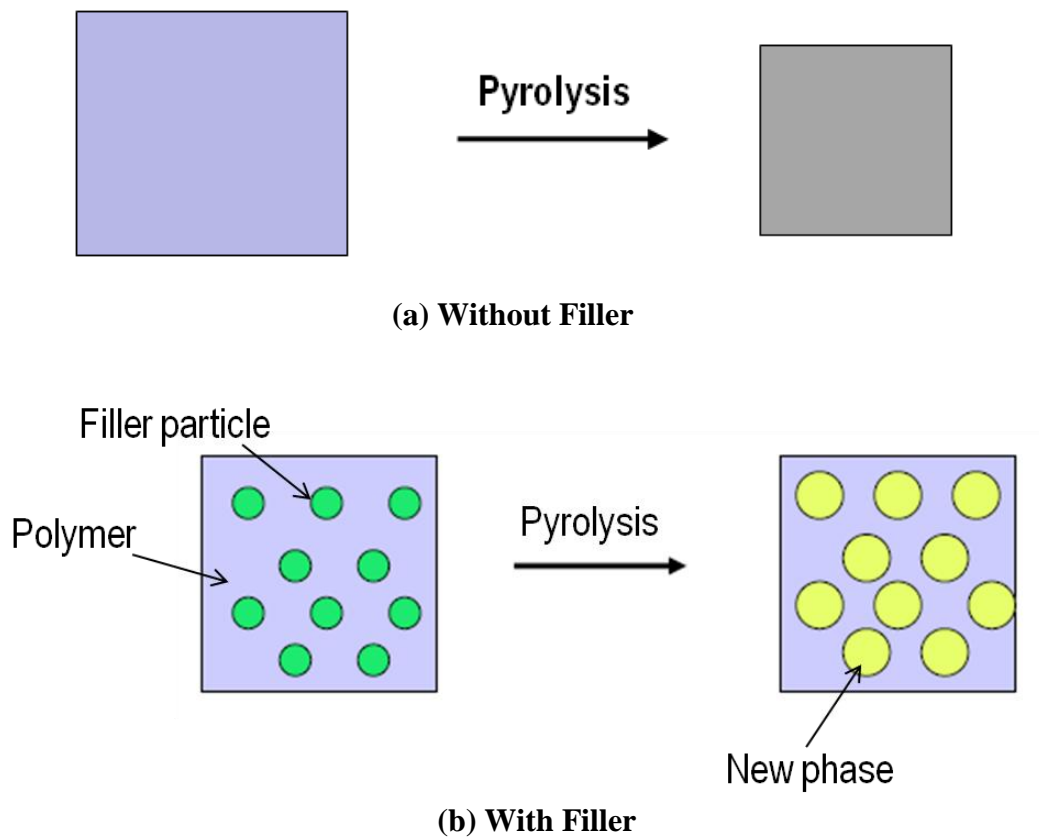


**Figure 4.2 Process of expansion of filler particle**

Therefore, numerous studies on this method have been conducted using various active fillers and processing conditions [43], [45], [48]. However, in most cases, a SiCN composite ceramic did not serve as a final ceramic in those studies. Even though there

were some studies treating SiCN composite ceramics [49], [51], their focus was not on reducing the shrinkage rate.

Our goal in this chapter is to make a PDC RTD sensor array on a substrate wafer using a SiCN-based composite ceramic and obtaining the resistance dependency of each sensor at increasing temperatures for actual RTD application. To reach the goal, two major challenges need to be overcome. First, because of about 30% of shrinkage of the SiCN polymer during heat treatment, a final SiCN ceramic generally cannot survive on certain substrates after heat treatment. Active filler controlled pyrolysis has been employed to overcome this issue. In our work, a shrinkage test has been performed to choose a suitable filler material out of several possible filler materials. Al and  $TiB_2$  powders were finally selected as the active filler. The second challenge is to make a desired pattern on a substrate. Screen printing and photo-lithography techniques have been combined to develop the clear rectangular shaped RTD sensor instead of etching. The measurement was done using a data acquisition system to find the relation between temperature and resistance for the resulting ceramic RTDs on a substrate.

## **4.2. Finding filler material**

### **4.2.1. Precursor preparation**

In general, the filler material can be categorized into two, which are passive and active fillers. As a passive filler, silicon carbide powder (Sigma-Aldrich) has been selected and it has a diameter of less than 30nm and 99% purity. As is well known, a passive filler does not react with the atmosphere and matrix material during the pyrolysis,

so there will be just filling effect during the process. And significant shrinkage reduction is not expected from SiC filler material.

An active filler reacts with the atmosphere or a polymer matrix. Two types of active filler materials were tested. One is elemental filler and the other is binary filler. Among possible binary filler materials such as TiB<sub>2</sub>, TiSi<sub>2</sub>, CrB<sub>2</sub>, ZrSi<sub>2</sub>, ZrB<sub>2</sub>, TiB<sub>2</sub> was selected. According to previous study, [44], under the nitrogen atmosphere, TiB<sub>2</sub> showed the largest volume expansion as shown in Table 4.1.

**Table 4.1 Volume expansion coefficient over the filler materials under Nitrogen  
(Source: Stackpoole et al [44])**

Filler		$\kappa\beta$	New phase
Elemental	Ti	1.08	TiN
	Cr	1.50	CrN
	Si	1.13	Si <sub>3</sub> N <sub>4</sub>
Binary	TiB <sub>2</sub>	2.14	TiN, BN
	TiSi <sub>2</sub>	1.53	Tin, Si <sub>3</sub> N <sub>4</sub>

In table 4.1,  $\kappa = \frac{\text{mass of reaction product}}{\text{mass of unreacted filler}}$  and

$$\beta = \frac{\text{density of filler}}{\text{density of reaction product}}.$$

The specific volume change of filler after reaction is expressed as follows,

$$\frac{\Delta V}{V_o} = \kappa\beta - 1 \quad (4.1)$$

where  $V_o$  is the original volume of filler, therefore  $\kappa\beta = 1$  for passive filler material since  $\Delta V = 0$  and  $\kappa\beta$  has to be larger than 1 for the filler with volume expansion. As shown in table 4.1,  $\text{TiB}_2$  has the largest expansion among elemental and binary filler materials.

As an elemental filler, Al powder was selected. According to previous study [43], Al powder reacted with Nitrogen during pyrolysis and it was found that almost zero percent of shrinkage rate occurred when Al powder was mixed with Polycarbosilane (PCS). At that time the volume ratio between Al and PCS was 56%.

In short, three filler materials were selected as candidates for our polyureasilazane polymer, which were SiC,  $\text{TiB}_2$  and Al. Titanium boride powder (Sigma-Aldrich) with an average particle size of 10um also was chosen. Al powder (Sigma-Aldrich) with a diameter of less than 75um and 99.95% of purity was used. They were all synthesized with a polysilazane pre-ceramic polymer, CERASET<sup>®</sup> (Polysilazane 20, KiON Defense Technologies, PA, USA) and 5% of photo-initiator (Irgacure 651, Aldrich Chemical, WI, USA). For the SiC filler, two precursor samples were made with the 10 and 25 wt% of SiC. For  $\text{TiB}_2$ , four precursor samples were prepared with 10, 40, 60 and 80% and for Al filler, three precursor samples were synthesized with 10, 40 and 60 wt%. So a total of 9 separate precursors were prepared for comparison of shrinkage rates. The weight ratios of filler to CERASET<sup>®</sup> for each precursor sample were tabulated in table 4.2. Those filler powders were dispersed and stirred magnetically for about 5 hours at 60°C. The liquid precursors were then placed in a vacuum for 2 hours to remove gas from the precursor.

**Table 4.2 The ratios of filler material to CERASET® for each precursor sample**

Fillers	Precursor 1	Precursor 2	Precursor 3	Precursor 4
SiC	10wt%	25wt%	•	•
TiB <sub>2</sub>	10wt%	40wt%	60wt%	80wt%
Al	10wt%	40wt%	60wt%	•

#### **4.2.2. Analysis of shrinkage rate**

##### **4.2.2.1. Sample preparation**

From 9 different precursors, free standing polymer structures were fabricated. As described in chapter 2, the Teflon film was used to make the free standing structures. The shape of the free standing polymer structures is rectangular so that the dimension of the structures can be measured by a digital micrometer (Carrera precision, USA). Three polymer structures were prepared for 9 separate precursors. Then all the polymer structures were placed into a high temperature furnace for heat treatment where crosslinking at 400°C and pyrolysis at 1100°C were conducted. After finishing the heat treatment, all resulting composite ceramics were taken out of the furnace and their dimension was measured again using the same digital micro meter. The data for the three samples were collected and the average value of each precursor was calculated and compared to one another.

#### 4.2.2.2. *Results*

Of the three different filler materials, SiC powder showed very poor results in reducing shrinkage rates as was expected. For the two precursor samples with 10wt% and 25wt% of SiC, there was no noticeable reduction in shrinkage rate. Shown in Figure 4.3, their shrinkage rates were almost the same as those of the original CERASET<sup>®</sup> polymer which is about 30% ~ 35%. It seems that because of the inertness of the SiC filler, there was no reaction with the polymer matrix or flowing gas resulting in no volume expansion during pyrolysis. However, with the precursor with 25 wt% of SiC powder, it seems that the filling effect of SiC powder into the polymer matrix decreases the shrinkage rate. But the reduction was too little to have much of an effect.

In the case of TiB<sub>2</sub> as a binary filler, there was a distinct decrease in shrinkage rate as the amount of weight percent increases. The precursor with 60wt% of TiB<sub>2</sub>, showed 14.95% of shrinkage rate and the one with 80 wt% of TiB<sub>2</sub> reached 4.8% shrinkage, which means that the precursor can possibly allow the RTD array to survive on the quartz wafer. Therefore, 80 wt% of TiB<sub>2</sub> was selected for further fabrication.

On the other hand, as an active filler material, Al also exhibited reasonable results in reducing the shrinkage rate of the final ceramic product. As shown in Figure 4.3, by increasing the amount of Al, the shrinkage rate decreased significantly. For the precursor sample of 60wt% of Al powder, the shrinkage rate reached about 5%, which means the Al powder is a suitable filler material for making a sensor array on a quartz wafer as well. As shown in Figure 4.3, 60wt% of Al precursor resulted in a successful SiCN/Al composite ceramic on the quartz wafer after heat treatment.

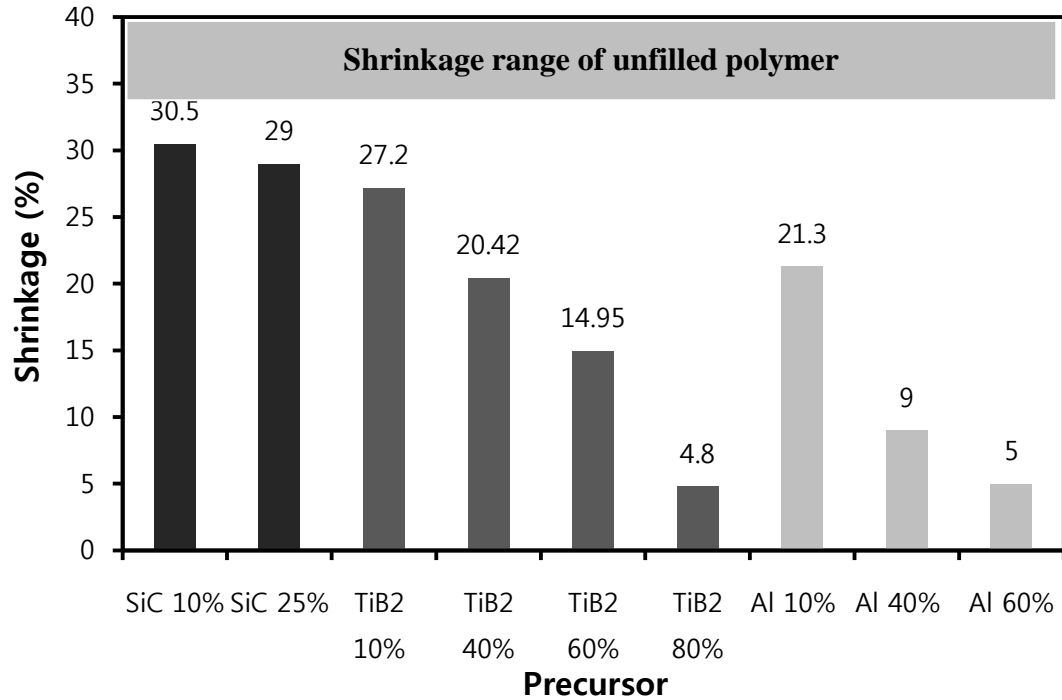


**Figure 4.3 Comparison of shrinkage rate with different filler materials**

Finally, based on our analysis of shrinkage rates using three filler materials, TiB<sub>2</sub> and Aluminum powder were tested to make the PDC RTD array on a substrate wafer. In Figure 4.3, 80 wt% of TiB<sub>2</sub> and 60 wt% of Al were mixed with polysilazane with a photo-initiator of 5 wt%. And then it was determined that those two precursors resulted in a successful SiCN/Al and SiCN/ TiB<sub>2</sub> composite ceramic on the quartz wafer.

### **4.3. Fabrication of a PDC RTD sensor array on quartz wafer**

#### **4.3.1. Screen printing technique**

The screen printing technique is a well known industrial technique to make some type of pattern on the surface of material. Recently, many applications in the field of fuel

cell and patterning of various sensors and devices on desired substrates have been accomplished by using screen printing technique [52], [53], [54], [55], [56].

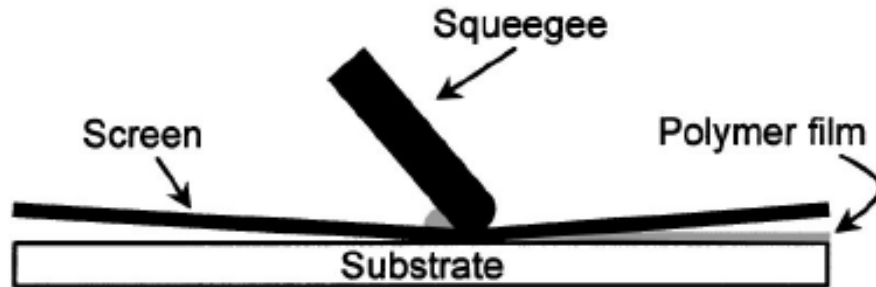


**Figure 4.4 Illustration of screen printing technique (Source : Shaheen et al [53])**

The screen printing technique is one of easiest surface pattern making methods. It is also a versatile design, very simple and very cost-effective compared to expensive vacuum technology. Furthermore, it can be applied to any type of surface such as ceramics, glasses, windshields, etc. The screen printing technique is already used in fabricating micro-scale patterning (less than 60um) for the multilayer interconnection in integrated circuits. However, the deposition of a thin film of under 100nm of thickness is believed to be inappropriate for screen printing. The estimated thickness of our sensor is in the range of between approximately 100um and 200um. Therefore, for the deposition of our pre-ceramic polymer with  $TiB_2$  and Al fillers into a substrate, it is suitable to use the screen printing technique.

#### **4.3.2. Fabrication of a PDC RTD array using cut-out plastic sticker**

An important part of the screen printing technique is the fabrication of a cut-out plastic sticker. A 3x3 and 4x4 rectangular shape of RTD designs is first drawn by

AutoCAD program and then a cut-out plastic sticker is printed by a digital die sticker printer. The designs of the RTD array are shown in Figure 4.5.

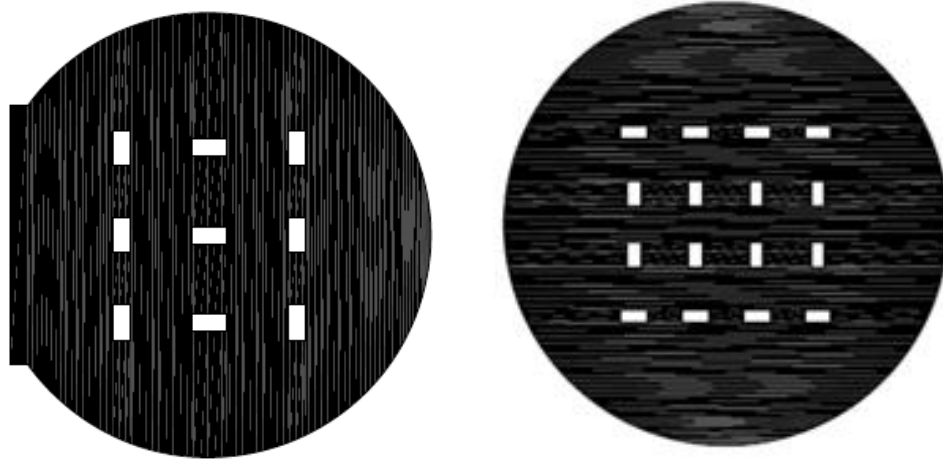


**Figure 4.5 Designs of RTD array drawn by AutoCAD**

The process of making RTD patterns on a substrate is shown in Figure 4.6. First, a cut-out plastic sticker (stencil) is attached to a quartz wafer to form a mold. Next, the prepared polymer precursor is dropped on the mold and screened by the squeegee. The next step is to make the pre-ceramic precursor firm in the sticker mold. There are two ways to do this. One is to expose the wafer to UV light from the bottom of the photomask, which causes the precursor to solidify in the mold. A second way is to put the whole wafer with the sticker mold on a hot plate, since the CERASET (polysilazane 20) is readily thermoset to a solid by heating up to  $180^{\circ}\text{C} \sim 200^{\circ}\text{C}$ . After etching out the precursor residue on top of the stencil mold using acetone, the cut-out plastic stencil is removed from the quartz wafer. Finally the desired RTD array of the polymer precursor remains on the quartz wafer as shown in Figure 4.6 (f).

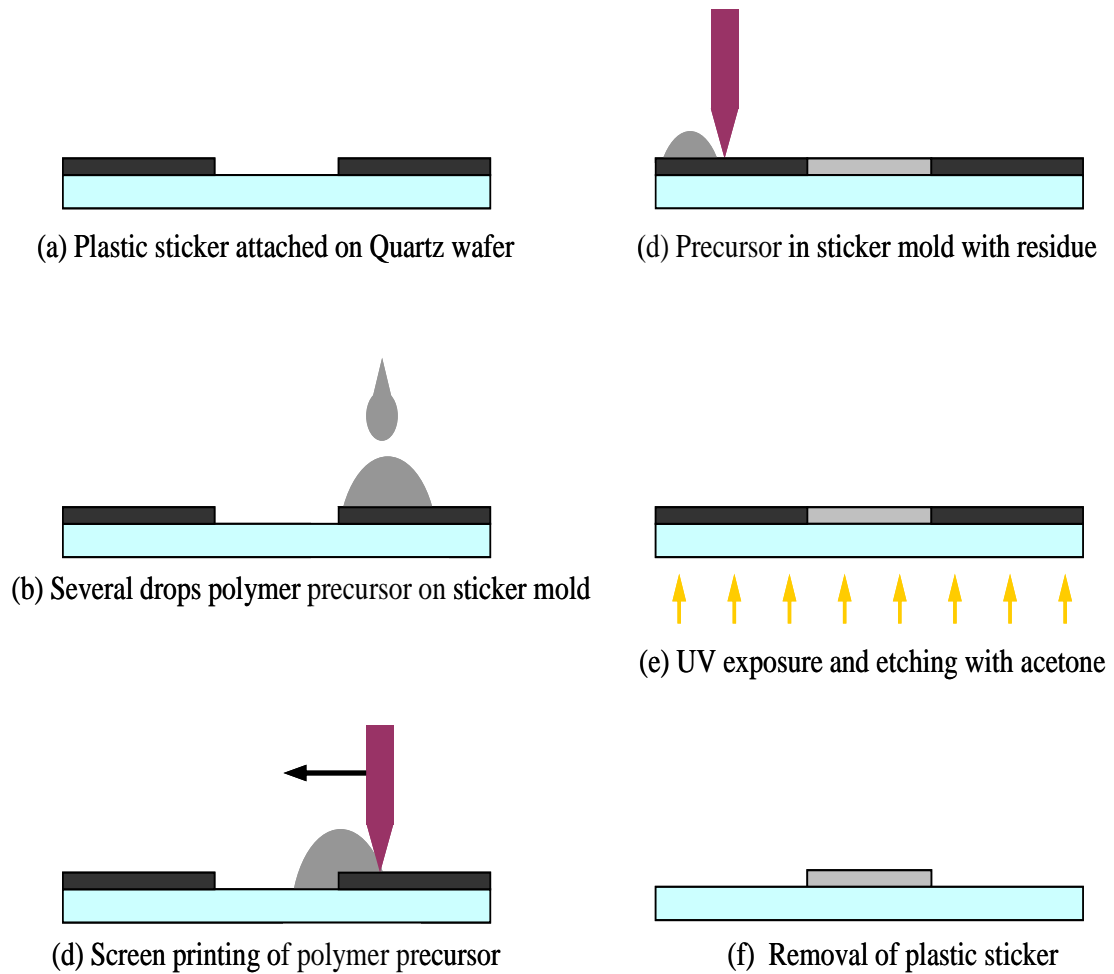


**Figure 4.6 Process of printing screen for patterning pre-ceramic precursor on quartz wafer**

Figure 4.7 shows the array of the cross-linked pre-ceramic polymer. The size of the polymer pattern is 1.5mm x 3mm for a 3x3 array and 1mm x 2mm for a 4x4 array. Additionally, the thickness of the RTD is between 200um and 300um. The color of the TiB<sub>2</sub> filler pattern is darker than that of the Al filler pattern. Therefore using the screen printing technique, it was possible to make a pre-ceramic pattern on a substrate not only successfully but also more easily than with photolithography.

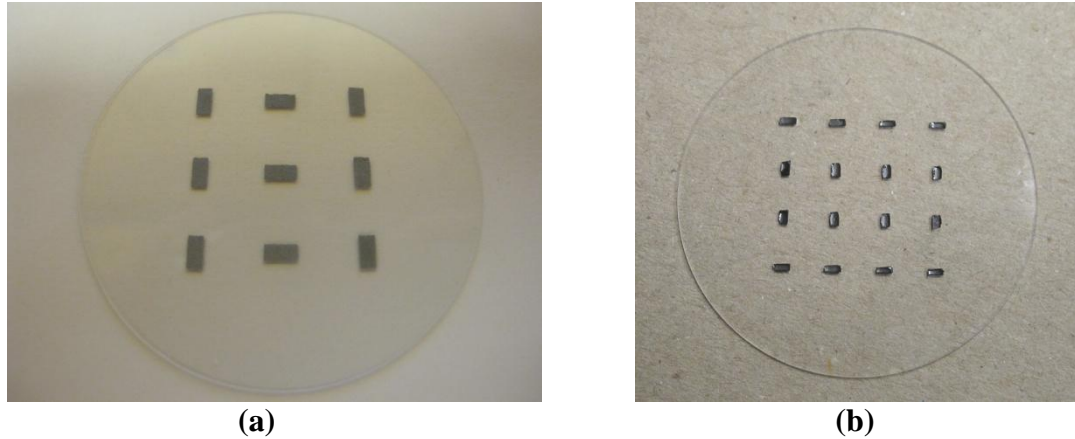


**Figure 4.7 Array of pre-ceramic precursor on quartz wafer before heat treatment;  
(a) Al filler precursor, (b)  $\text{TiB}_2$  filler precursor**

Compared to the photo-lithography technique, the screen printing technique yielded several benefits. In terms of the wall definition of the pattern, when using only the photo-lithography, the sample showed relatively poor wall definition whereas the screening printing technique exhibited a very clear boundary of wall as shown in Figure 4.8. When UV light is exposed from the bottom of the quartz substrate, the wall definition of the pattern on substrate was not as good as the wall definition fabricated by our direct contact lithography technique described in chapter 2. It is because that the UV light from the bottom is diffracted and weakened due to the thickness of the quartz substrate, which is about 500 $\mu\text{m}$ . Moreover, UV light is attenuated by the precursor which has dark color due to the addition of filler particles. However, with the screen printing technique, a sharp edge definition was achievable as shown in Figure 4. 8 (b).

Other advantages of the screen printing technique include: 1) unlike other shadow masks, the sticker mask keeps the precursor from infiltrating beneath the mask, a result that ruins the pattern; 2) the technique is very easy and economical in terms of fabrication;

3) this method can furthermore be expanded to include the shadow mask for the sputtering.

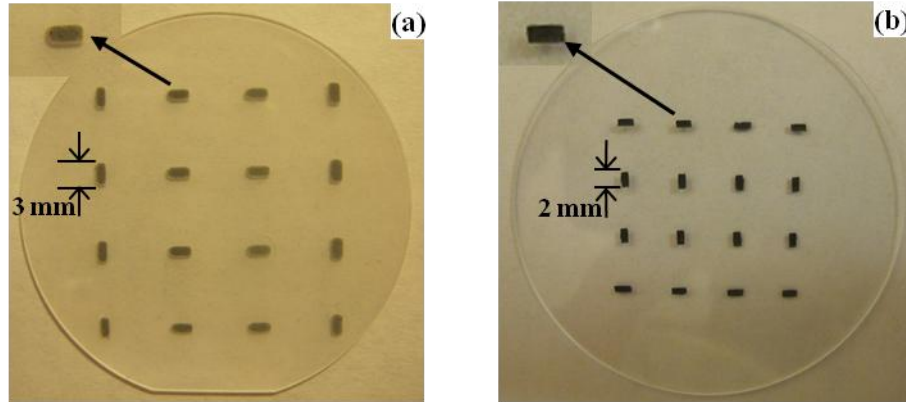


**Figure 4.8 4x4 of filler used PDC RTD on quartz wafer; (a) photo-lithography only, (b) photo-lithography and screen printing**

After making the pre-ceramic polymer pattern on a wafer, the patterned polymers are converted to the composite ceramic by the process of heat treatment. Among the three major factors (temperature, time and atmosphere) shown to affect the property of the resulting ceramic material [16], [21], we primarily control the temperature to obtain the desired electrical conductivity. The heat treatment comprises two steps: cross-linking and pyrolysis. Because of higher electrical conductivity of Al and  $TiB_2$  filled RTD than the RTDs without filler, it was able to reach desired conductivity without undergoing annealing process.

The two processes, cross-linking and pyrolysis, are performed in a GSL1600X Vacuum and Gas Tube Furnace (MTI, USA) with a flow rate of 100 sccm of nitrogen. The wafers with patterned array are placed on an alumina plate and then inserted into the furnace tube. As shown in Figure 4.9, the temperature cycle is first raised at a rate of

2.5°C/min to 400°C and held for 3 hours to perform cross-linking. Then, the temperature is increased at the rate of 2.5°C/min to 1100°C and held for 3 hours for pyrolysis, followed by same rate of cooling down to room temperature.

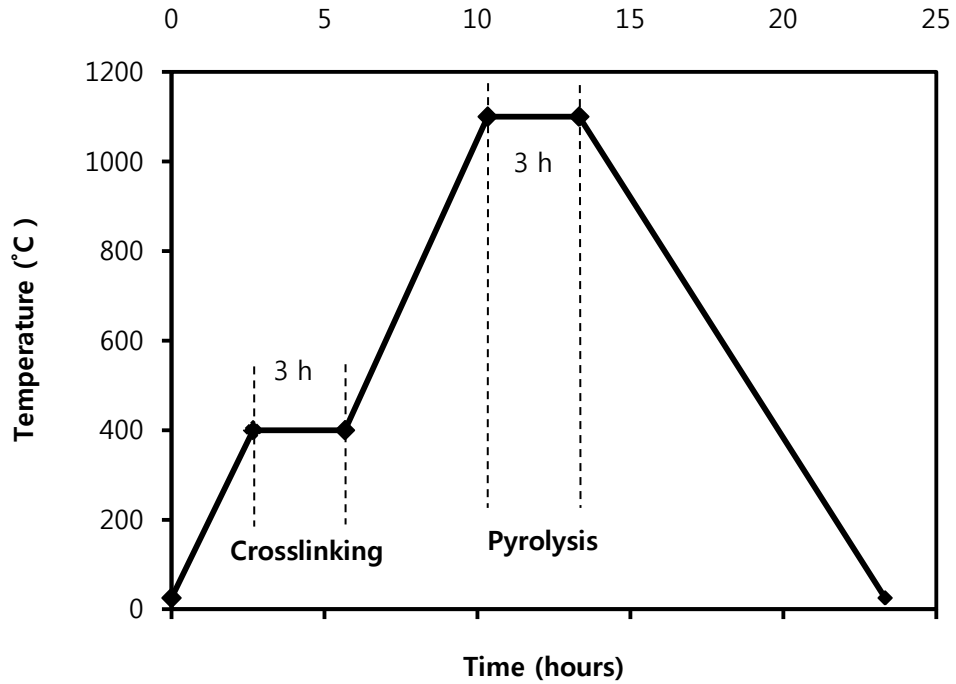


**Figure 4.9 Process of heat treatment**

Photographs of  $4 \times 4$  RTD arrays are also shown in Figure 4.10 before and after heat treatment. In spite of about 5 % of shrinkage rate during shrinkage rate analysis in Figure 4.3, the polymer patterns fabricated by screen printing technique successfully survived on the quartz wafer, unlike the results depicted in Figure 4.1 (b). Therefore, from our Active Filler Controlled Pyrolysis (AFCOP) fabrication process, it was possible to obtain the PDC pattern with near zero shrinkage rates on the substrate and the PDC RTDs with no cracks or breaking on the wafer after pyrolysis.

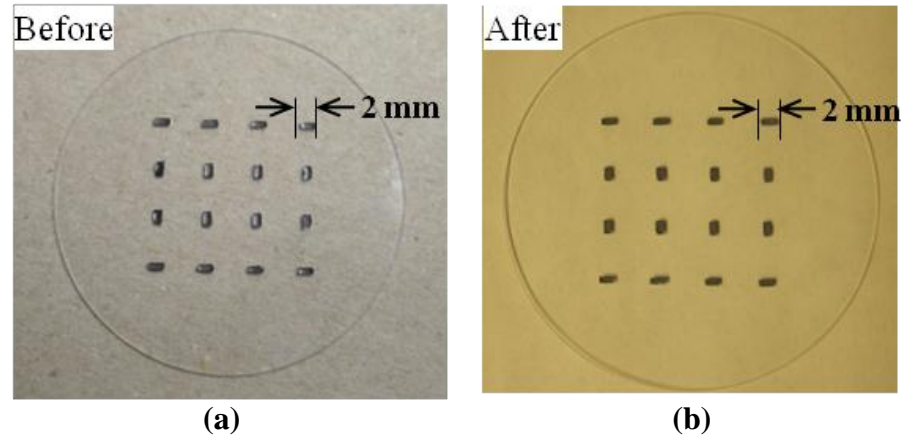


**Figure 4.10** The picture of resulting PDC RTD array on quartz wafer: (a) before, (b) after

#### **4.4. Patterning electrode for electric connection**

For the RTD sensor, electrode patterns are made on a quartz wafer using the same method as for the sensor array fabrication. A shadow mask has been fabricated using the same cut-out plastic sticker technique as the one used in the RTD pattern array. Figure 4.11 (b) shows the plastic sticker mask which is attached to the quartz wafer with the PDC RTD array. The shape of the electrode is designed by AutoCAD before printing. To deposit the conductive material, RF sputtering method is employed. RF sputtering of Au is conducted on the wafer with the thickness of 150nm after applying the sticker mask with the proper electrode shape attached to the wafer. After removing the sticker mask, the desired electrode pattern is obtained on the quartz wafer. The processes are illustrated in Figure 4.7 (a). The lower picture of Figure 4.7 (b) shows the completed SiCN/Al composite ceramic RTD array. Therefore the PDC RTD array is ready to be connected to the data acquisition system to measure the electrical property such as conductivity.

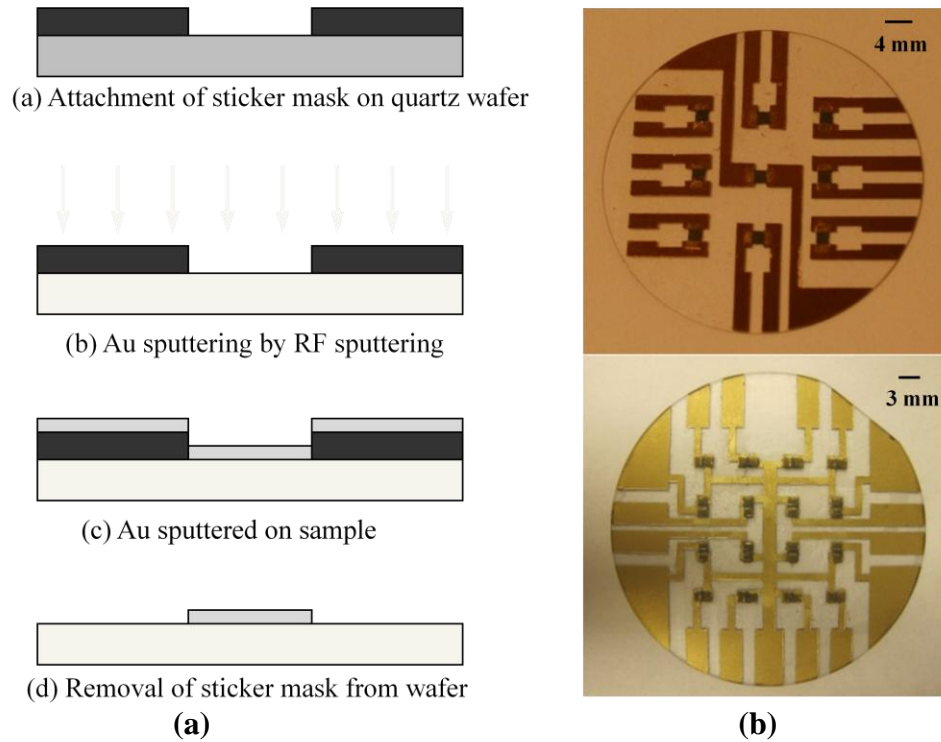


**Figure 4.11 Electrode patterning by RF sputtering using the shadow mask method**

## 4.5. Measurement of Resistance with varying temperature

### 4.5.1. Measurement of PDC RTD with Al filler

Before measuring the electrical resistance for all SiCN/Al RTDs simultaneously, the measurement of a single SiCN/Al PDC was conducted first using the measurement setup shown in Figure 3.9 of Chapter 3. Instead of the gold electrodes, discussed in the previous section, copper electrodes are used. A high temperature conducting paste (Pyroduct 597-C, Aremco Inc., USA) was used as a connection material between the electrode and copper wire. A multimeter (Fluke 8845A/8846A, USA) was also used to measure the resistance, and a thermocouple was placed right next to the RTD sensor to obtain the

temperature value. Both the RTD sensor and thermocouple are placed on the hot plate and subjected to high temperature in the open air. The measured data are transmitted to the Labview program in PC.

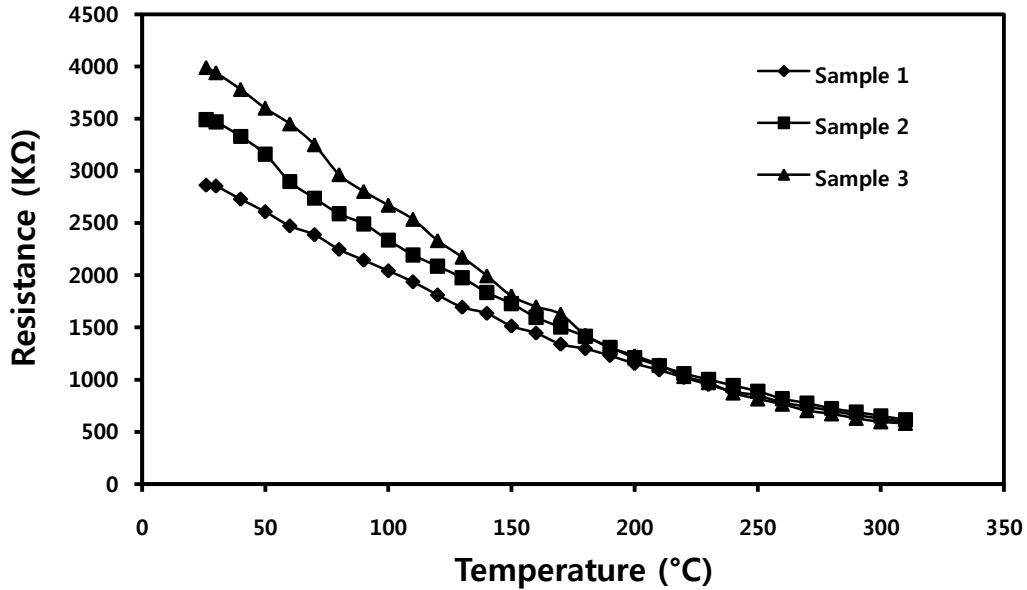


**Figure 4.12 Three Resistance measurements out of RTD array**

Figure 4.12 shows the temperature dependency of the resistances of three SiCN/Al composite ceramic RTD sensors selected randomly from the 3x3 arrayed sensors. Basically as in the original SiCN ceramic material, it was found that our resulting ceramics also had a negative coefficient for the temperature dependency. Furthermore, their drop-down pattern was smooth and reasonably reliable to be used as an RTD sensor even though their starting resistance values at room temperature were different, which is a similar property of the original SiCN ceramics. In conclusion, the pattern of the negative temperature coefficient of the resulting composite ceramic is very similar to that of the original SiCN ceramics. It is believed our resulting PDC of SiCN/Al

composite can be used as an RTD sensor. The range of temperature for this measurement is between room temperature and about 320°C.

For further measurement, 4 X 4 Al filled PDC RTD array and Au electrodes shown in Figure 4.13 (a) were made. To measure the resistance of all 16 RTDs at the same time, a new data acquisition system has been developed as shown Figure 4.13 (b). According to our circuit configuration, as the resistance goes down with elevated temperature, measured output voltage by data acquisition system is also decreasing. First, the resistance of all 16 RTDs at room temperature was measured. Basically their measured resistances over 16 RTDs were widely distributed. The RTDs in the array have resistances ranging from 150 K $\Omega$  ~ 20 M $\Omega$  at room temperature.

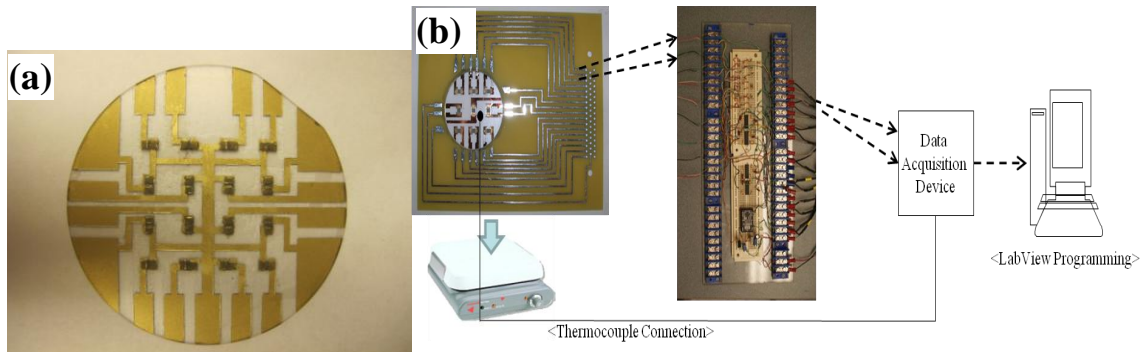
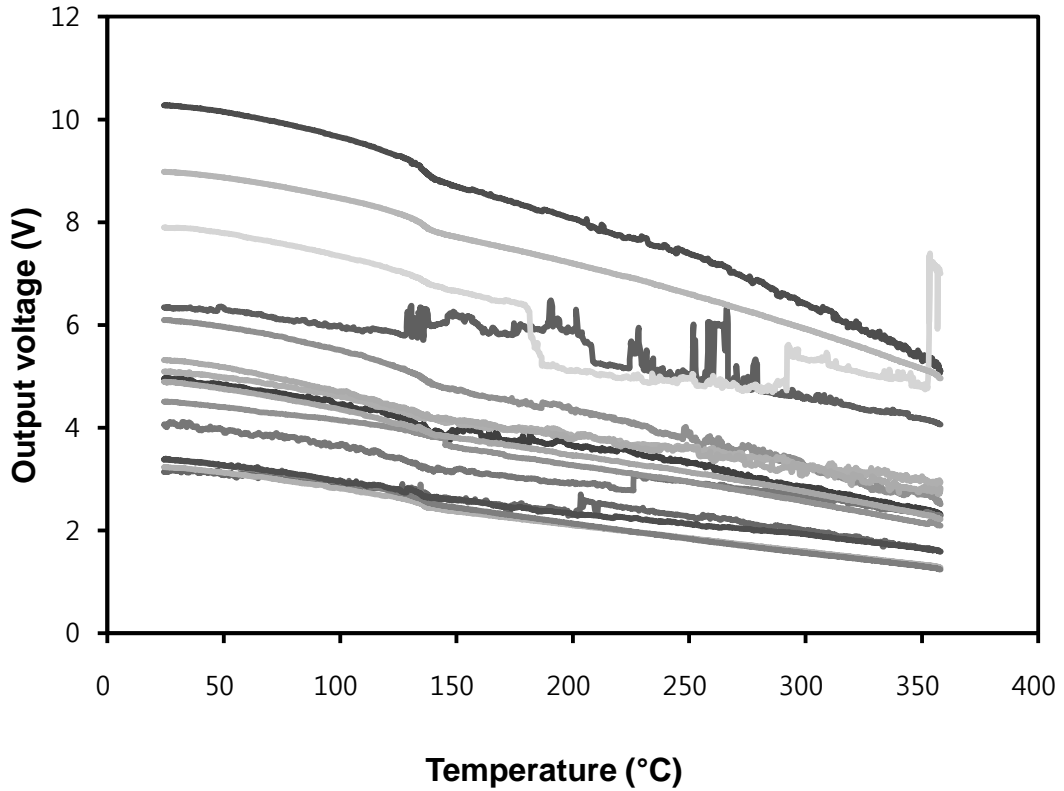


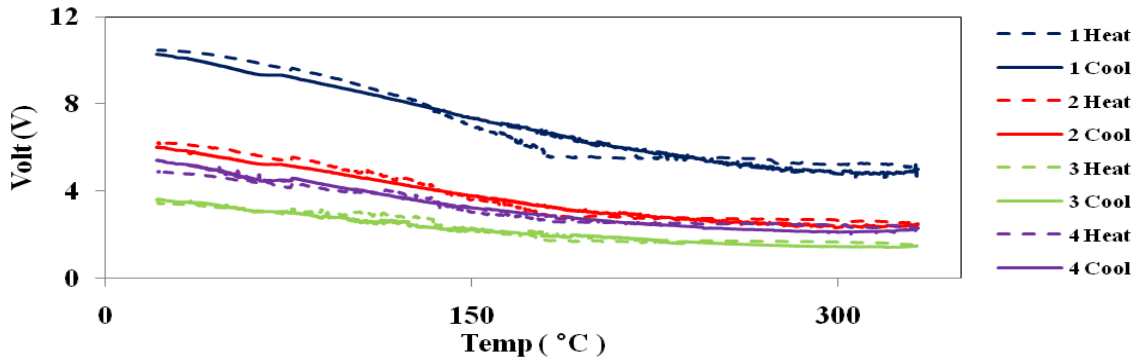
**Figure 4.13 Picture of 4 X 4 Al filled PDC RTD array with Au electrode**

The measurement result for the 16 RTDs are shown in Figure 4.14 (a). The temperature range of this measurement was between room temperature and about 350°C. In general, smooth curves were obtained with the negative temperature coefficient. As the temperature moved beyond about 120°C, several noises and malfunctions of circuits were noted for the three RTDs. In Figure 4.14 (b), the curves can be examined in detail by looking at the 4 sensors in one graph and investigating the repeatability when they are

cooled down. Additional curves of cooling down were added by dotted lines. In general they showed good repeatability, that is, there is not a large difference of resistance between heating up and cooling down.



(a)



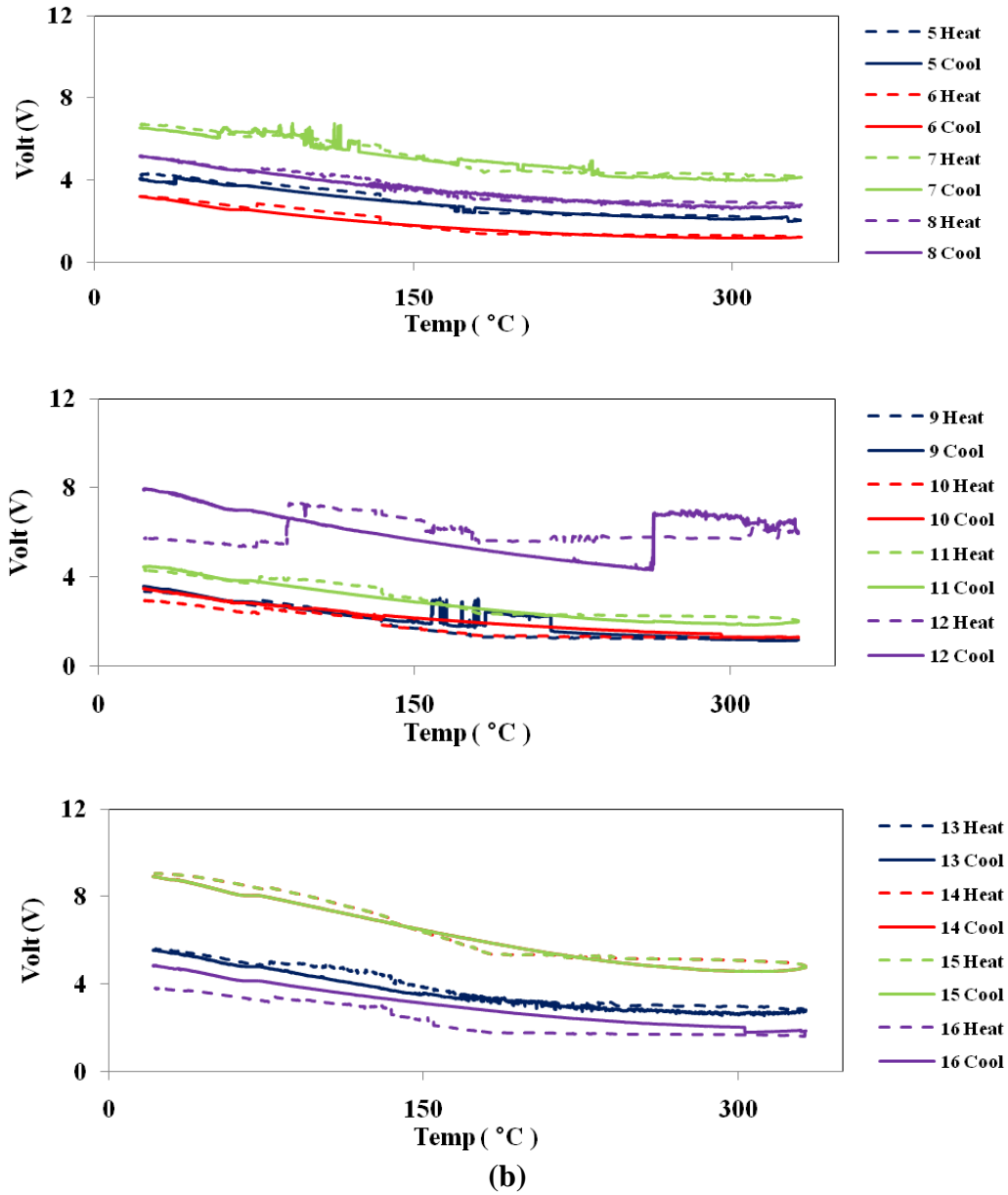


**Figure 4.14 The output voltages as a functions of temperature in 4 groups**

In addition, Figure 4.15 shows the voltage difference between heating up and cooling down for the 10 selected RTDs out of 16 RTDs after removing the malfunctioning RTDs. In the temperature range of 250°C ~ 290°C, they have almost the same results for output voltage.

In conclusion, the Al filled PDC RTDs work well from the measurement readings in Figure 4.14 even though some malfunctioning RTDs were found. Also they showed good repeatability for cooling down. However, the malfunctioning problem needs to be fixed, a problem which could be caused by the electrical connection between the electrode and the data acquisition system.

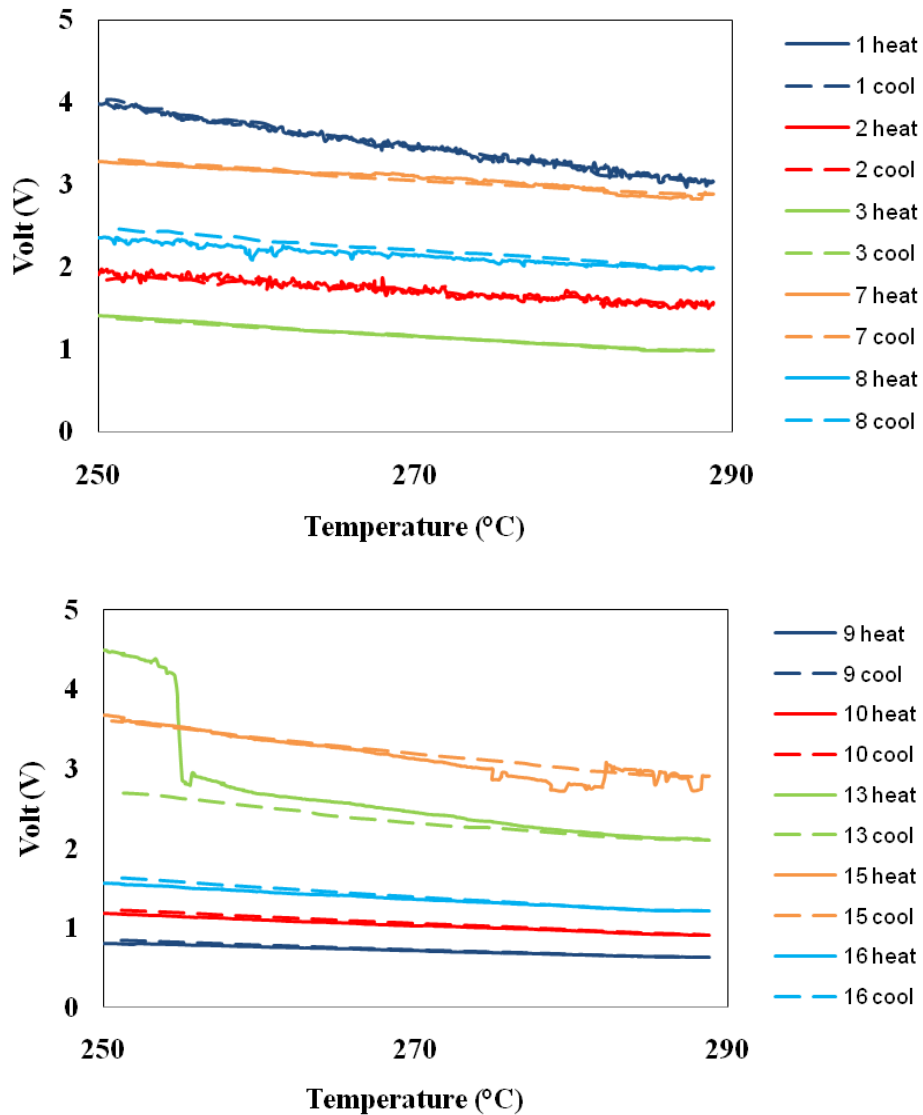


**Figure 4.15 Comparisons of output voltages during heating up and cooling down for temperature between 250 and 290°C**

#### 4.5.2. Measurement of PDC RTD with TiB<sub>2</sub> filler

The electrical resistance change of the TiB<sub>2</sub> filled RTD also has been measured after the 4 X 4 array was fabricated followed by the electrode sputtering process. The measurement result is shown in Figure 4.16. The resistance decreases with a rise in temperature in Al filled PDC RTDs. The highest temperature for this measurement is about 300°C. It was found that the pattern of the curves showed a nice relation between output voltage and temperature, even though it has some abnormal fluctuation for a few sensors. Based on this measurement, it is believed TiB<sub>2</sub> filled PDC material also can be used as an RTD.

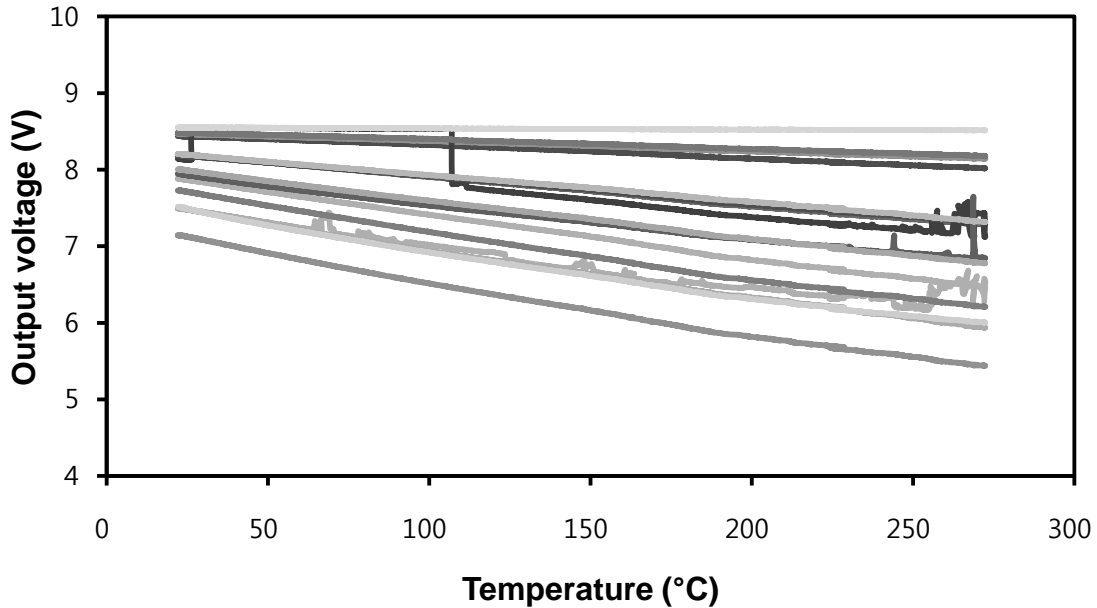


**Figure 4.16** Plot of resistance change of TiB<sub>2</sub> filled PDC with temperature

It was noted that there are several differences in the RTD curve between the Al and TiB<sub>2</sub> filled RTD. First, regarding the resistance range of RTDs on array at room

temperature, the  $\text{TiB}_2$  filled RTD has the range of  $300\Omega \sim 10\text{k}\Omega$ , which is very low compared to the Al filled RTD. The lower range of electrical resistance allowed for an easier circuit configuration for output voltage. Second, as shown in Figure 4.17, the voltage-temperature curve has less noise than that of the Al filled RTD. The  $\text{TiB}_2$  filled RTD has a smoother curve shape than Al filled RTDs, a result which is a much better feature for an RTD sensor. The temperature range for this comparison is restricted from  $50^\circ\text{C}$  to  $100^\circ\text{C}$  and 3 data are collected per 1 second. In addition, the same heating rate of about  $10^\circ\text{C}$  per minute is used for both measurements.

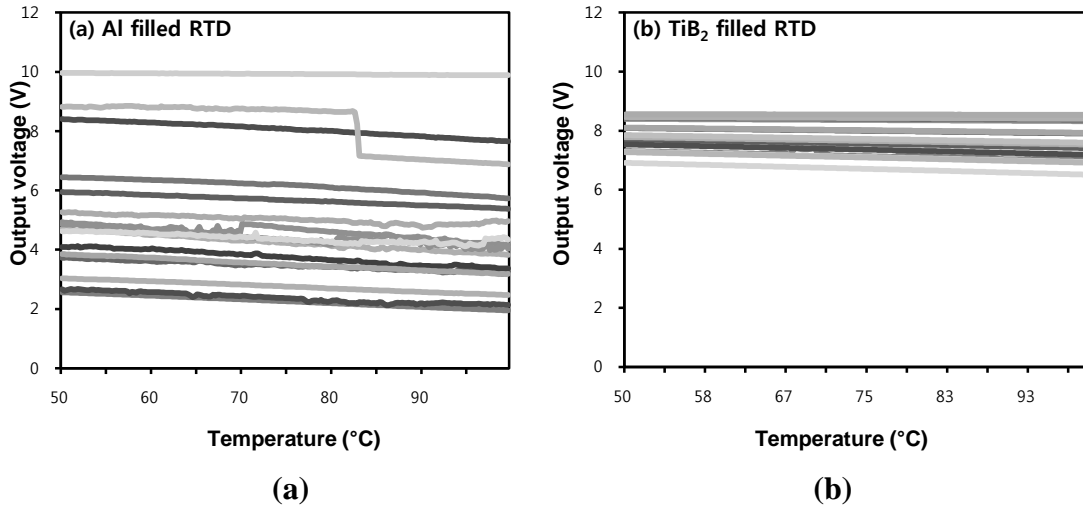


**Figure 4.17 Comparison of curve smoothness between Al filled and  $\text{TiB}_2$  filled RTDs: (a) Al filled RTD (b)  $\text{TiB}_2$  filled RTD**

We also note that the Al filled RTD showed a much wider range due to the wider range of electrical resistance, which is  $150\text{K}\Omega \sim 20\text{M}\Omega$ . The output voltage range of the Al filled RTD, shown in Figure 4.17 (a), is about from  $2.5\text{V} \sim 10\text{V}$ , while that of the  $\text{TiB}_2$  filled RTD is narrower, from about  $6.9\text{V}$  to  $8.5\text{V}$  as shown in Figure 4.17 (b).

## **4.6. Characterization of PDC RTDs with filler material**

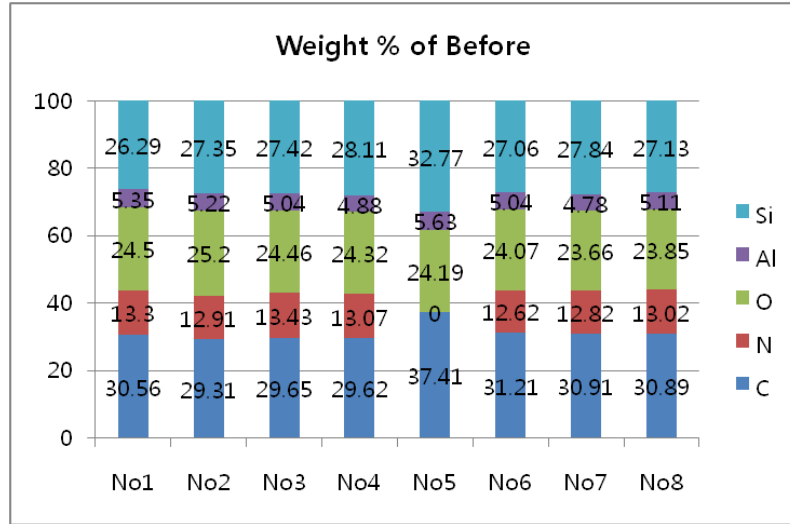
Further characterization studies for both filler RTDs have been conducted. The SEM/EDS method is used to undergo the elemental analysis of RTDs for before and after pyrolysis. Also the effect of RTD size on the surface condition and electrical conductivity is investigated as well as effect of annealing temperature on conductivity. XRD is employed to examine if any types of crystals are formed on the RTD during heat treatment after the application of AFCOP to our PDC system.

### **4.6.1. Characterization of Al filled RTD**

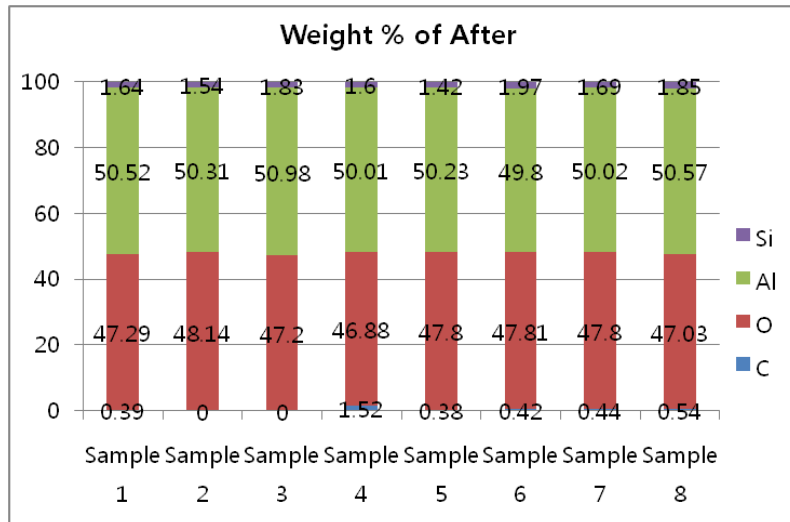
#### ***4.6.1.1. Elements analysis of Al filled RTDs***

To investigate the elemental difference of the Al filled RTD before and after heat treatment, EDS analysis was used. Eight RTDs were selected out of 16 RTDs for testing and types and weight % of elements were detected by EDS. After heat treatment, EDS analysis is executed for the same RTDs.

Figure 4.18 shows the results. Before heat treatment, as expected, all elements, Si, C, N, Al originating from the precursor (CERASET, Photo initiator, Al powder) are detected. Remarkably, the amount of oxygen was higher than expected. This is likely because aluminum reacts with oxygen as soon as it is exposed to the air. After the heat treatment, it was found that there was a significant change in the ratio of element as shown in Figure 4.18 (b). The material becomes a Si-Al-O-C system material and the amount of silicon and carbon decreases significantly. However, all 8 RTDs showed almost the same ratio of elements.



(a)



(b)

**Figure 4.18 EDS result for 8 RTDs in array; (a) before, (b) after heat treatment**

#### 4.6.1.2. Effect of annealing temperature on conductivity

As reported in chapter 3, the annealing temperature of the PDC affected significantly the electrical conductivity of our PDC. In the case of filler used RTDs, different results were expected and we tried different pyrolysis temperatures such as 1200°C, 800°C. However, the measurement result showed no consistency in resistance

change with different temperatures. The resistance of Al filled RTDs at room temperature was in the range of about  $150\text{ K}\Omega \sim 20\text{ M}\Omega$  when the pyrolysis temperature was  $1100^\circ\text{C}$ . As mentioned, the range of resistance of this RTD is very wide so that the measurement results of the Al filled RTDs with different pyrolysis temperatures such as  $800^\circ\text{C}$  and  $1200^\circ\text{C}$  were also within that same resistance area. No discrete relation between pyrolysis temperature and electrical conductivity was found in our Al filled RTDs. And this is the reason we choose the  $800^\circ\text{C}$  for our pyrolysis temperature.

#### 4.6.1.3. *Effect of RTD size on surface condition*

The SEM pictures of various sizes of filler used RTDs were taken for the surface. In most cases that the size of RTD is more than  $2 \times 4\text{mm}$ , it was found that there was micro-sized thickness of cracks on surface of RTD.

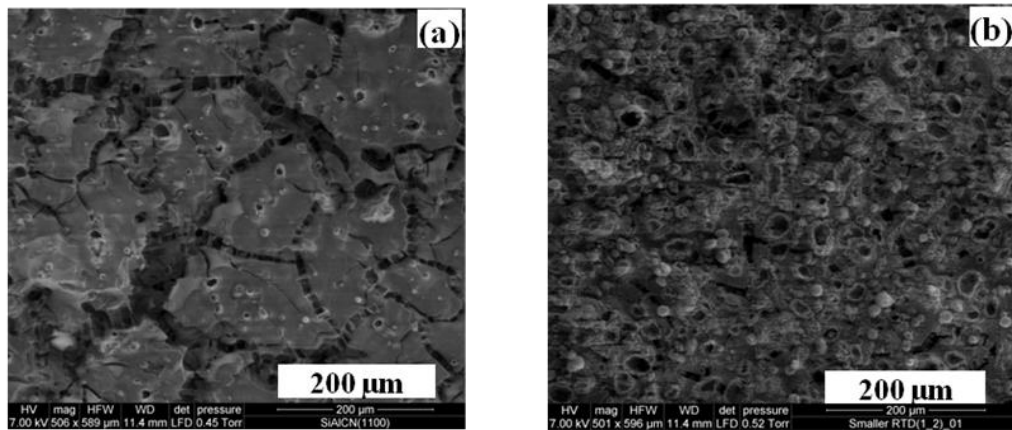


**Figure 4.19 SEM images of RTDs' surface (a) 2 X 4mm size (b) 1 X 2 mm size**

Figure 19 shows the SEM picture of surface of Al filled RTD for the two sizes, which are  $2 \times 4\text{mm}$  and  $1 \times 2\text{mm}$ . As mentioned, noticeable micro cracks are found in  $2 \times 4\text{mm}$  sized Al filled RTD in Figure 4.19 (a) while it is very hard to find cracks in the

smaller sized RTD of 1 x 2 mm as shown in Figure 19 (b). It is believed that the smaller size of RTD is, the fewer cracks is found on the surface of RTD. In our filler used RTDs, there are almost no cracks under 1 x 2 mm size and the shrinkage rate of preceramic precursor significantly depends on the size of polymer pattern

In case of  $\text{TiB}_2$  filled RTD, it was found that there is much less micro cracks in the 1 X 2 mm size RTDs. As shown in Figure 4.20 (a), much smoother surface than Al filled RTD was examined with same magnification of SEM. However, obviously there was some micro cracks found in the bottom-left of the picture. Figure 4.20 (b) shows the SEM picture with 2 times magnification of Figure 4.20 (a). These results are coincident with the previous work that the cracks likely arise due to enhanced stress in the larger features [57]. This fact would be crucial when deciding the size of RTD.

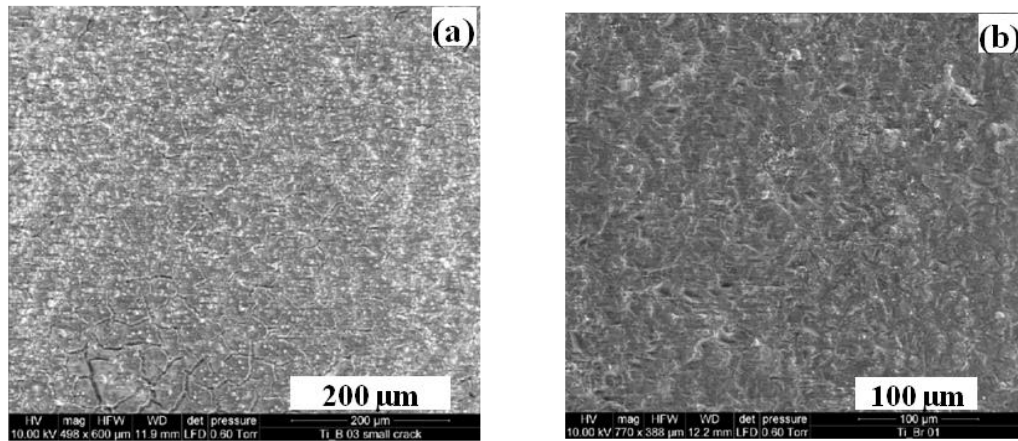


**Figure 4.20 SEM images of the surface of  $\text{TiB}_2$  filled RTDs of 1 X 2 mm size**

#### **4.6.1.4. XRD analysis of Al filled RTD**

The PDC RTDs without filler showed an amorphous material state almost up to 1400°C as shown in Figure 3.2, from which it was seen that crystallization started from

about 1400°C annealing temperature. Likewise, an XRD test for PDC RTD with filler Aluminum was carried out to investigate if the final ceramic had any types of crystals after the reaction between Al filler and the matrix or atmosphere during pyrolysis.

Two Al filled RTD samples were prepared: one had the pyrolysis temperature of 800°C and the other had 1100°C. The reason for different pyrolysis temperatures is to see if there is any effect of the pyrolysis temperature on crystal types in the final PDC. Figure 4.21 (a) shows the XRD (X'Pert Pro Multipurpose Diffractometer, PANalytical) analysis result for the Al filled RTD with an 800°C pyrolysis temperature. It is noticed that both silicon and aluminum were detected as well as the compounds AlN and Al<sub>2</sub>O<sub>3</sub>. Also it was found that the active filler Al reacted with the nitrogen gas used as an atmosphere and resulted in aluminum nitride (AlN), which is quite consistent with the results found in the study of Xie et al [43]. Also the aluminum reacted with oxygen in the matrix of the RTD and ended up with crystallization of Al<sub>2</sub>O<sub>3</sub> in the final PDC RTD. Based on these results, the active filler Al reacts during pyrolysis and the accompanying volume expansion enables the RTDs to survive heat treatment on the substrate.

Figure 4.21 (b) shows the XRD results of Al filled RTD with a 1100°C pyrolysis temperature. As pyrolysis temperature increases, it can be noticed that many more crystals are found in the RTD by a glance at Figure 4.21 (b). Besides Si, AlN, Al<sub>2</sub>O<sub>3</sub> which are found in the RTD with 800°C, a new compound of 4 was found, which means that the filler material Al reacted with Si during pyrolysis. Therefore, it turned out that the active filler, Al, reacted during heat treatment as expected from the AFCOP method and the emergence of the new phases caused volume expansion and allowed the RTD to survive on substrate.

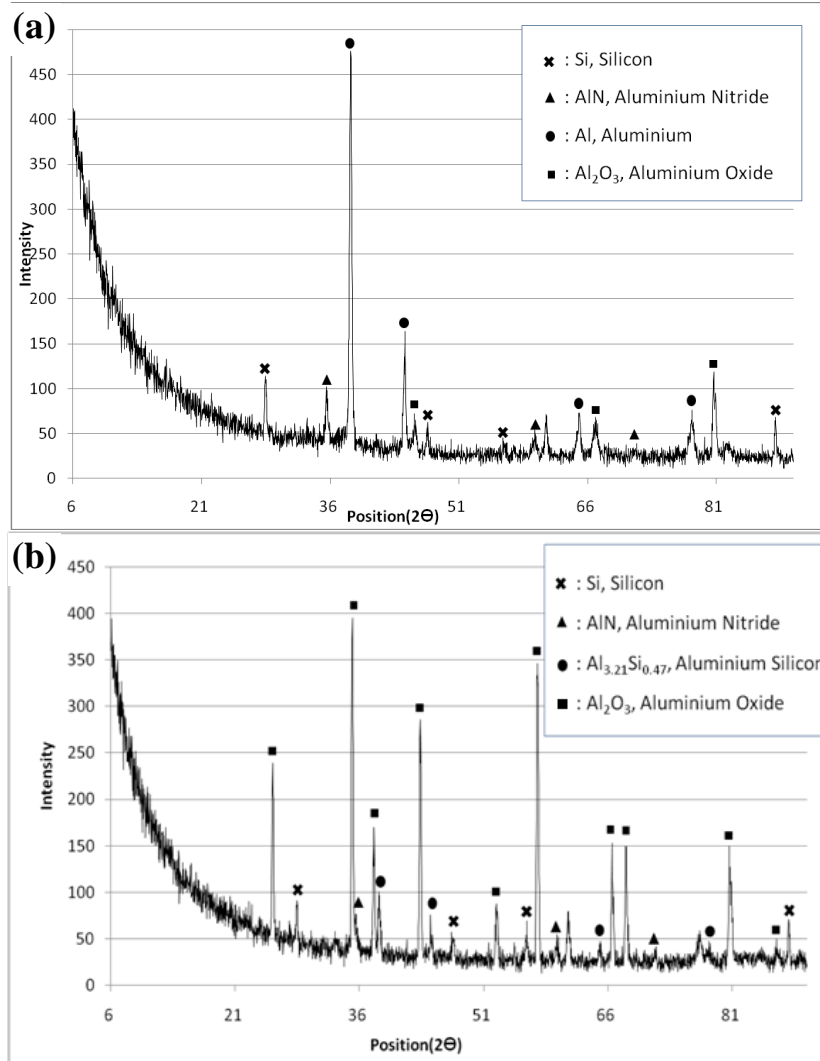


Figure 4.21 XRD results of Al filled RTDs pyrolyzed at : (a) 800°C, (b) 1100°C

## 4.6.2. Characterization of TiB<sub>2</sub> filled RTD

### 4.6.2.1. Elements analysis of TiB<sub>2</sub> filled RTDs

Figure 4.22 shows the result of EDS analysis on TiB<sub>2</sub> filled RTDs. Two different types of samples, which are before and after pyrolysis, are prepared, from same precursor to compare the elemental change in RTD after heat treatment.

For the result of RTD before heat treatment shown in Figure 4.22 (a), over 7 different patterns, they appear to have almost similar ratio of element. Si element has

highest weight percent and the nitrogen has lowest. Besides the elements, Si, N, C, Ti from filler ( $\text{TiB}_2$ ) and CERASET, oxygen was also found likewise in Al filled RTDs. It is believed that the oxygen is from air or the photo-initiator during patterning process.

Figure 4.22 (b) shows the EDS result for over 11 different RTDs after heat treatment. It was found that ratio of weight percent for Ti and Si remains almost same as before heat treatment. However, the amount of oxygen increased to about 50 wt% and the ratio of carbon decreased dramatically to nearly zero percent. It is thought that final ceramic product from  $\text{TiB}_2$  filler makes Si-Ti-O-C dominant material from our experiment.

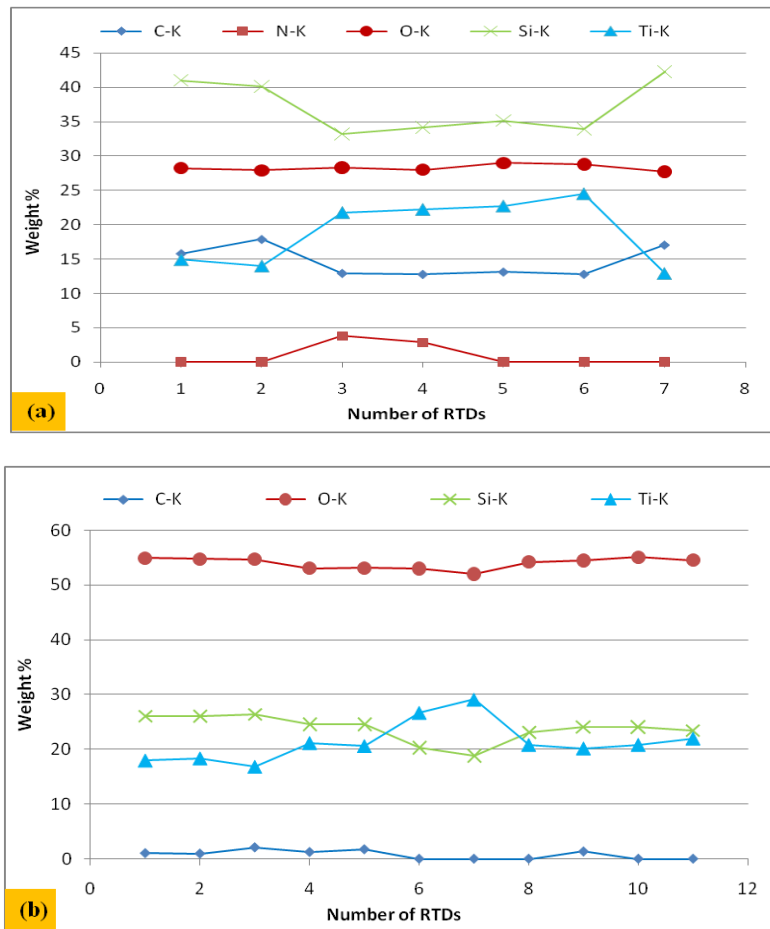
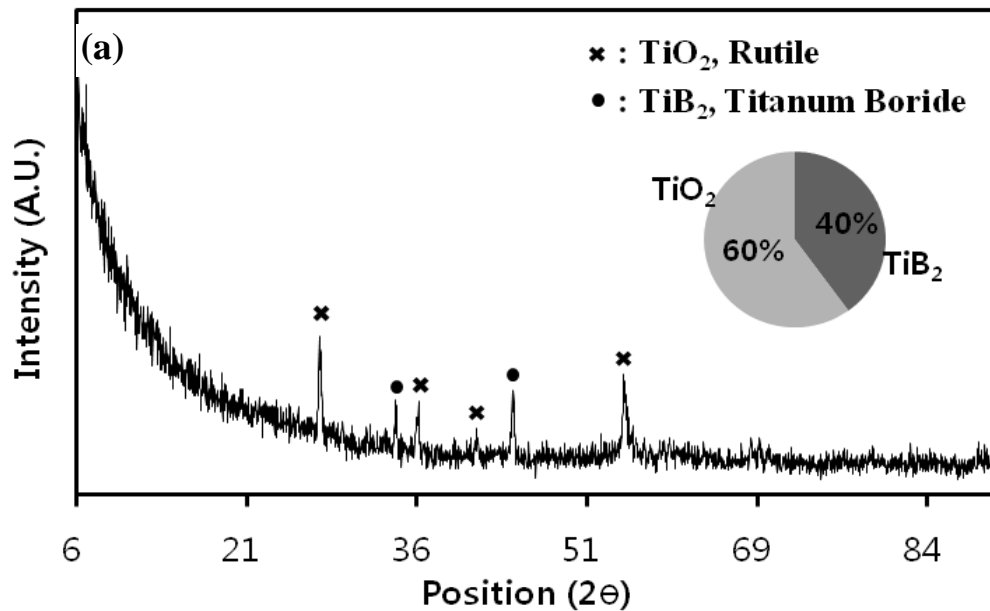


Figure 4.22 EDS results on  $\text{TiB}_2$  filled RTDs: (a) before and (b) after pyrolyzing

#### 4.6.2.2. XRD analysis of $TiB_2$ filled RTD

In a similar manner of the Al filled RTD, two different  $TiB_2$  filled RTDs were prepared: one is at 800°C pyrolysis temperature and the other at 1100°C. Figure 4.22 (a) shows the XRD results of the  $TiB_2$  filled RTD with 800°C. The oxygen in the polymer matrix reacted with the element Ti in the active filler  $TiB_2$  and resulted in a new phase of  $TiO_2$ , called Rutile. The filler,  $TiB_2$  was also detected. It is thought that the detection of  $TiB_2$  is because some  $TiB_2$  still remains in the RTD due to the high melting temperature (3230°C).

In the case of the 1100°C pyrolysis temperature shown in Figure 4.22 (b), no additional phase was found. Instead, more crystallization took place as was the case for the Al filled RTD. In addition, a stronger intensity of  $TiO_2$  was detected because of more reaction between Ti and oxygen due to the higher pyrolysis temperature. The ratio of  $TiO_2$  increased from 60% to 81% when the pyrolysis temperature increased to 1100°C as shown in the pie chart in Figure 4.22 (b).



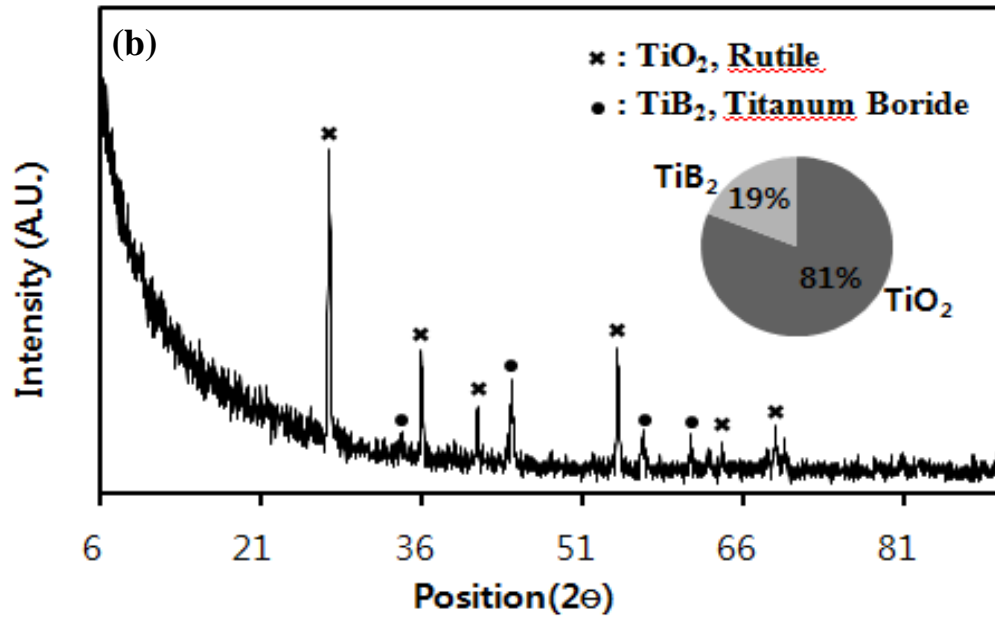


Figure 4.23 XRD results of  $\text{TiB}_2$  filled RTDs: (a) pyrolyzed at  $800^\circ\text{C}$ ; (b) at  $1100^\circ\text{C}$

#### 4.7. Summary and conclusion

In this chapter, we successfully fabricated Al and  $\text{TiB}_2$  filled RTDs on a quartz wafer. An active filler controlled pyrolysis method was employed to overcome the shrinkage problem of the Polyureasilazane polymer, CERASET. After testing three different kinds of filler materials, which are SiC,  $\text{TiB}_2$  and Al, in terms of the linear shrinkage rate, it turned out that SiC particle has almost no effect on reducing shrinkage rate but the 60 wt% of Al and 80 wt% of  $\text{TiB}_2$  filler has achieved about 5% shrinkage rate. After the heat treatment, a final ceramic film RTDs remained on the quartz wafer without any crack or damage.

A new approach of fabricating a pattern on a wafer was applied. Using a combination of screen printing and UV exposure technique, it was possible to make a

higher resolution pattern on the wafer more easily and economically. Electrical resistance over the increasing temperature range was also investigated for the final Al and TiB<sub>2</sub> filled RTDs. It was found that the resulting ceramic had a very good temperature dependency of resistance for use as an RTD sensor.

From EDS and XRD analysis on Al and TiB<sub>2</sub> RTDs, it revealed that the filler materials reacted with the elements in preceramic polymer and atmosphere nitrogen resulting in new phase such as AlN, Al<sub>2</sub>O<sub>3</sub>, Al<sub>3.21</sub>Si<sub>0.47</sub>, TiO<sub>2</sub>. It is believed that the new phase after heat treatment leads to compensation of volume loss in preceramic polymer and finally makes the RTDs survive on wafer.

## **Chapter 5**

# **FABRICATION AND MEASUREMENT OF HEAT FLUX SENSOR (HFS)**

### **5.1. Introduction**

In this chapter, fabrication of prototype of Heat Flux Sensor (HFS) and measurement of heat flux based on developed Data Acquisition System (DAQ) are introduced. As mentioned in introduction chapter, two types of Heat Flux sensor are fabricated depending on the types of RTD: one is from free standing SiCN RTD and the other is from filler used RTD. The process of fabricating the two types of HFS and the setup for measuring temperature gradient of two RTDs are described. Some results of measurement are presented.

### **5.2. HFS made of free standing SiCN PDC**

The process of fabrication is shown in Figure 5.1 and can be described as follows: First, two free standing SiCN RTDs are prepared. For the electric connection, copper wires are fastened at the end of RTD and followed by putting silver pasting on connected part. For the middle layer, OMEGABOND 400 is employed. OMEGABOND has high thermal conductivity (11 btu-in/ft<sup>2</sup>-hr-°F) and relatively easy curing (18 ~ 24hrs in air drying or 4hrs in 82°C oven). For sure, the operating temperature of OMEGABOND is about 1425°C, which means it has reasonable properties for middle layer of HFS. Also

OMEGABOND has electrically insulated and adhesive property after it is mixed with water. Therefore, prepared two RTDs are attached to middle layer of OMEGABOND followed by proper thermal curing. Fabricated HFS are attached on test coupon that plays a role of heat source after heated by other heat source such as hot plate, laser, etc.

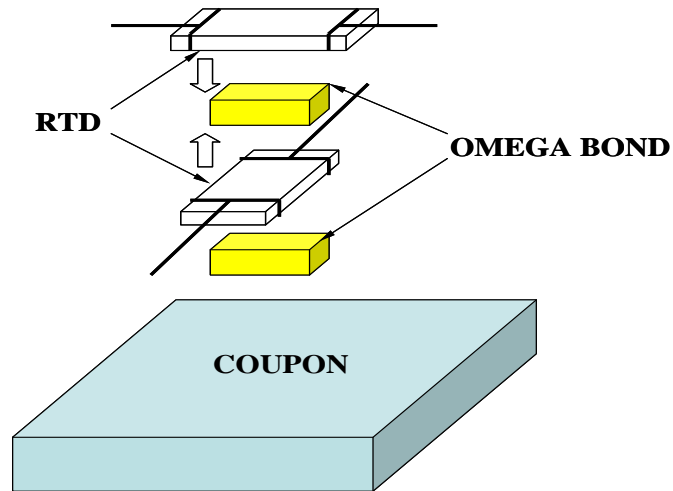


**Figure 5.1 Process of fabrication of HFS and attaching on coupon**

Figure 5.2 shows the pictures of HFS made by free standing SiCN RTDs on metal coupon. The copper wires are going out from the ends of SiCN RTDs and light yellow colored OMEGABOND are seen after thermal curing.

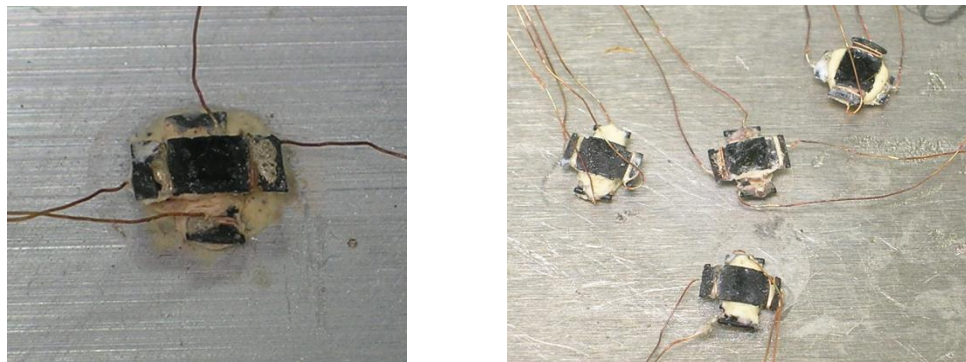


**Figure 5.2 Picture of HFS made by free standing SiCN RTDs**

### 5.2.1. DAQ configuration for Heat Flux measurement

Wheatstone bridge is used to obtain the temperature gradient between two RTD with a small spatial separation, which is middle layer. As shown in Figure 5.3, two RTDs are connected to Wheatstone bridge configuration where fixed resistor and potentiometer is also placed. According to working principle of Wheatstone bridge circuit, when the ratio of  $R_f$  to resistance of RTD1 is equal to the ratio of P to resistance of RTD2, the output voltage between 1 and 2 is zero. For sure, when two RTDs are connected to Wheatstone bridge first, they are not balanced and show some output voltage. Hence for the initial balance of circuit, potentiometer P is adjusted making zero voltage between point 1 and 2.

After making balance of circuit, heat is applied to HFS and the resistances of RTDs change accordingly. Those resistances difference makes certain amount of output voltage with temperature difference of two RTDs. The output voltages are detected by data acquisition equipment.

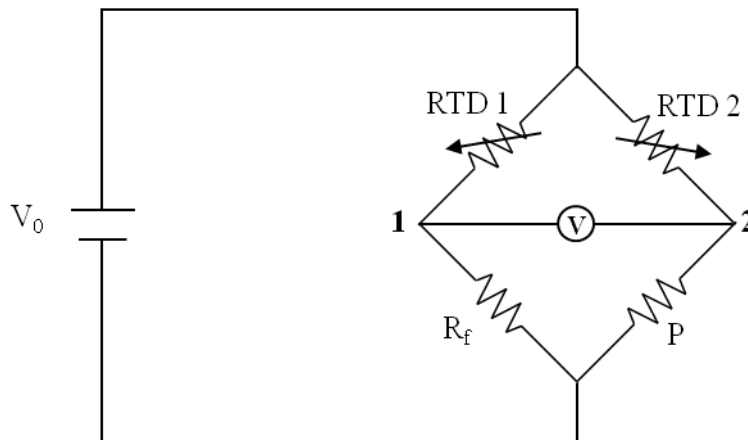
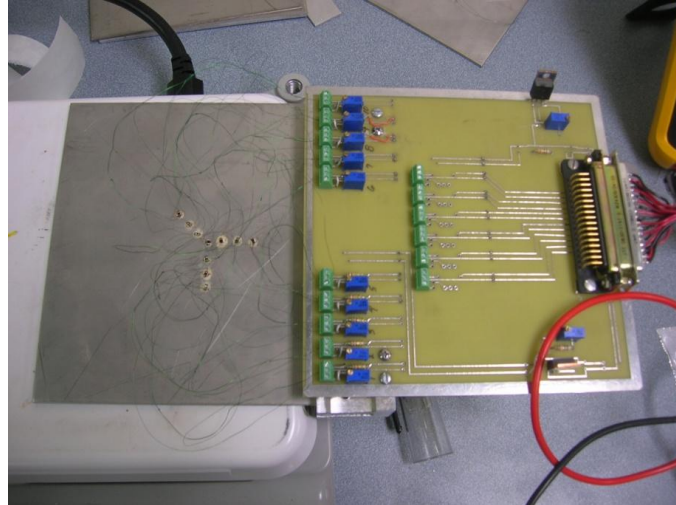


Figure 5.3 Circuit diagram of Wheatstone bridge for free standing SiCN HFS

Figure 5.4 shows the mounted HFSs on stainless steel sample and the circuit board for Wheatstone bridge where numbers of Wheatstone bridge circuits are integrated. The board is connected to data acquisition equipment that transports the output voltage data to the Labview program in PC.



**Figure 5.4 Picture of Mounted HFS on sample and wheatstone bridge circuit board**

### **5.2.2. Measurement result**

After mounting the circuit board to stainless steel sample, the stainless steel sample was placed on the hot plate to simultaneously calibrate multi-HFSs. 4 HFSs are selected and tested up to about 100°C. As shown in Figure 5.5, in general, the output voltage, other words temperature gradient between two RTDs are increasing with temperature rising. Also it is examined that the output voltage is not quite stable with time changes showing significant noises. It seems that more accurate electrical connection between RTDs and wire and noise control are required for better use as a HFS. However, the

obtained output voltage showed reasonable pattern to be used as a HFS after calibration with commercial HFS.

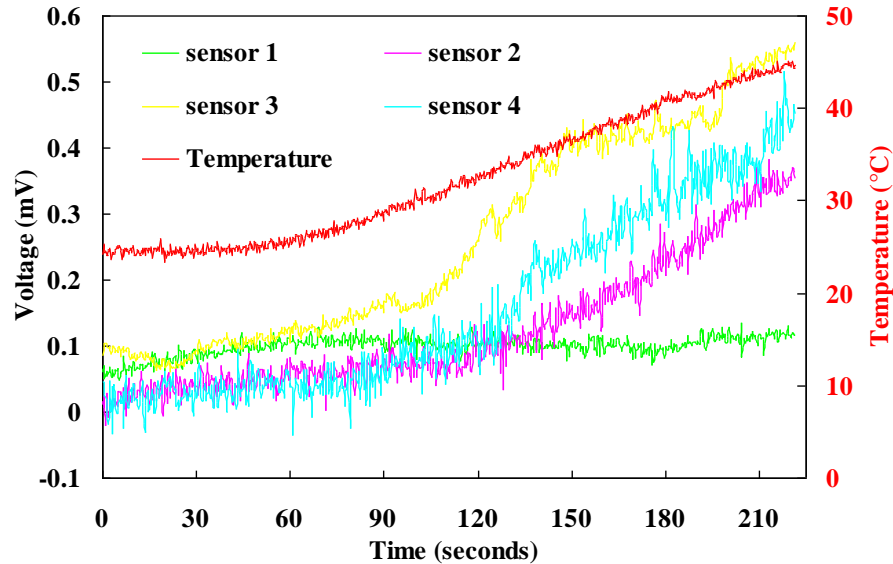
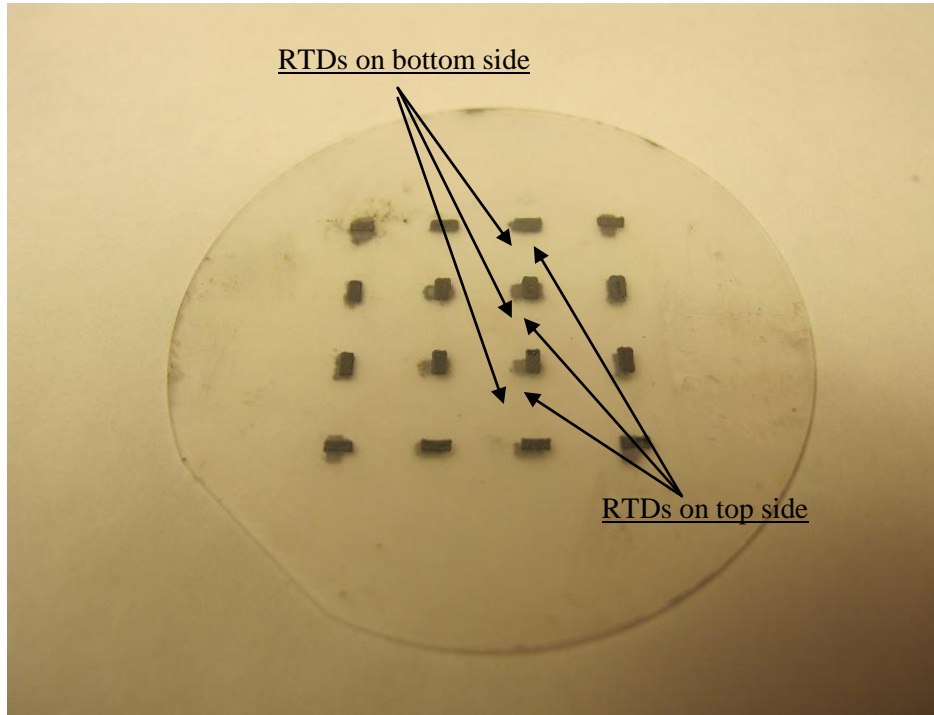


Figure 5.5 Output voltage measurement result for 4 HFSs

### 5.3. HFS made of filler used PDC RTDs

In chapter 4, RTD array of 3 X 3 and 4 X 4 has been fabricated using Al and TiB<sub>2</sub> filler material. In order to make HFS, another RTD array is required to be patterned on the other side of sapphire wafer. Figure 5.6 shows the picture of completed 4 X 4 HFS array with sapphire wafer as middle layer. We have fabricated 4 X 4 RTD pattern on both side of sapphire wafer. The RTD arrays are patterned first on both sides of wafer using plastic sticker mold and then place it into the furnace followed by heat treatment under 800°C pyrolysis temperature. After heat treatment, the RTD arrays are successfully come out from furnace. Therefore, two RTDs in same position on wafer compose of one HFS

resulting in 16 HFSs. After electrodes by gold sputtering are deposited, resistance difference of two RTDs in same position is used to derive the amount of heat flux.



**Figure 5.6 Picture of RTD arrays on two sides of substrate**

### **5.3.1. DAQ configuration for HFS array**

First issue for making the DAQ configuration for HFS array is to connect electrodes of RTDs on wafer to DAQ. However, making electric connection, for example, for  $3 \times 3$  RTDs on wafer is not an easy work since total of 18 wires need to go out of wafer, which causes unexpected contact of wires and confusion of original location of wires. To prevent this problem, first a PCB board that has same number of electrodes at the same place as electrodes in array wafer is fabricated as shown figure 5.7. It has a hole in the middle so that the wafer can be attached to the edge of hole making electric

connection with the electrodes in PCB Board and array wafer. And silver paint is employed to make electric connections between electrodes of wafer and PCB. Then, 18 printed electrodes on PCB are connected to the circuit shown in Figure 5.7(a). Figure 5.7(b) shows the back side of PCB board after the RTD array wafer is attached to PCB board using silver conductive paint.

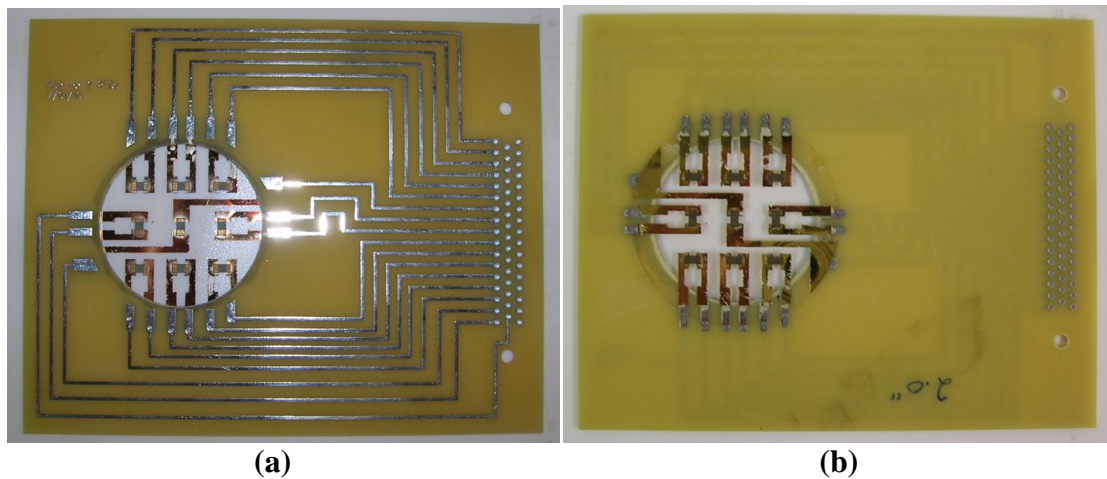


**Figure 5.7 Pictures of PCB attached with wafers; (a) front, (b) back**

The printed electrodes on PCB board are connected to the circuit board where same numbers of voltage divider configuration as that of RTDs on wafer are located. Hence, 9 voltage divider configurations are placed for  $3 \times 3$  RTD array. In the voltage divider configuration, as shown in Figure 5.8(a), a regulated power source is supplied as a voltage source and fixed resistance  $R_f$  is located in series with RTD. While the electrical resistance of RTD changes due to the temperature rising from the heating source, the output voltage  $V$  is also altered according to the equation (5.1) derived by Ohm's law under the constant voltage supply.

$$V = \frac{R}{R + R_f} V_0 \quad (5.1)$$

Hence, after calculation, measured voltage from our RTD can be converted to the resistance at corresponding temperature. 9 separate voltage divider networks are prepared as shown in Figure 5.8 (b) and the wires from each network are connected to the data acquisition device (NI instrument). Therefore, final output voltage from the circuit can be recorded in labview program.

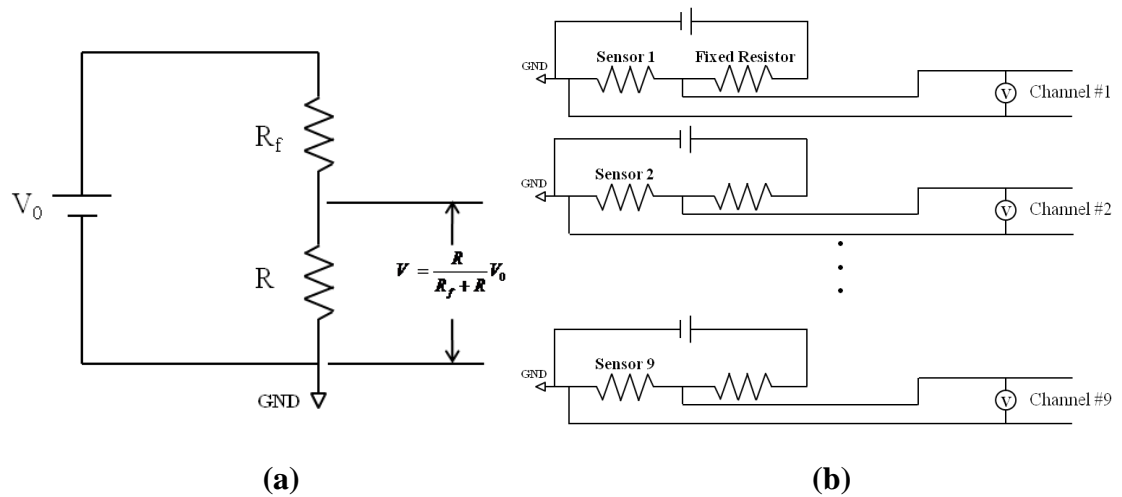


**Figure 5.8 Circuit configuration of voltage divider network**

Figure 5.9 shows the overall view of final data acquisition system for  $3 \times 3$  RTD array after employing the remodeled circuit board and PCB. The PCB board with RTD array is placed on the hot plate. And then thermocouple is attached on the top surface of wafer of RTD array using OMEGABOND 400 (OMEGA, USA) for the temperature measurement. And the PCB board and circuit board are connected with electric wires. The output voltage from circuit board and temperature from thermocouple are put

together in data acquisition device and finally the labview program shows and stores the data into a file.

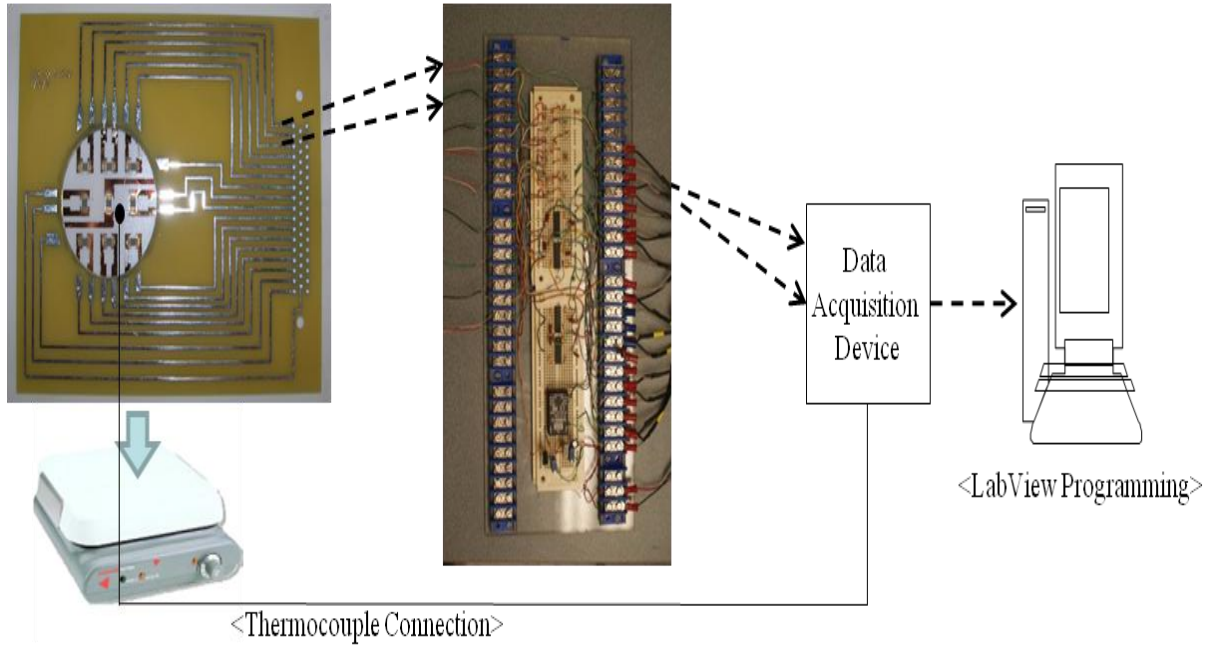


**Figure 5.9 Configuration of data acquisition system**

The measurement configuration for HFS is nearly same as that for RTD except connection of electrodes of wafer to PCB board. Since another RTD array exists on the other side of wafer, twice number of electrodes for PCB board is needed. And for the connection, silver conductive paste is also employed. For the Heat Flux measurement, output voltages data for each RTD are obtained by the Labview program. Temperature difference of RTDs can be used to calculate the heat flux by using Fourier's Law below,

$$Q = -k\nabla u = -k \frac{\Delta T}{\Delta x} \quad (5.2)$$

where  $k$  and  $\Delta x$  are thermal conductivity and thickness of substrate respectively.

### 5.3.2. Measurement of output voltage of 4 HFSs

To avoid the complex electrode deposition, 4 HFSs are tested instead of 16 HFSs shown in Figure 5.6. Front side of quartz wafer has 16 TiB<sub>2</sub> filler RTDs prepared and the other side has just 4 RTDs, which makes 4 HFSs. Figure 5.10 (a) shows the locations of 4 HFSs and numbering of 20 RTDs. Prepared wafer is connected to the DAQ system shown in Figure 5. 11

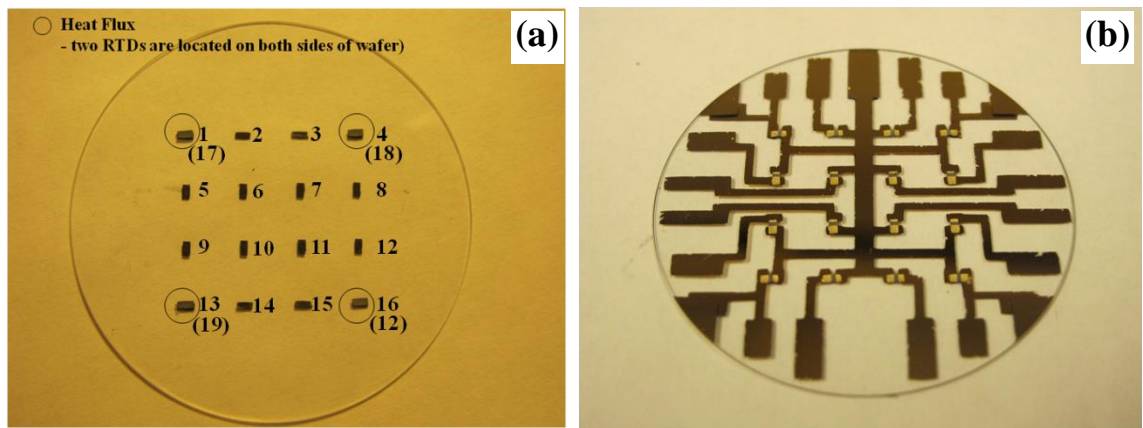


Figure 5.10 (a) Locations of HFSs, (b) After gold electrodes are deposited

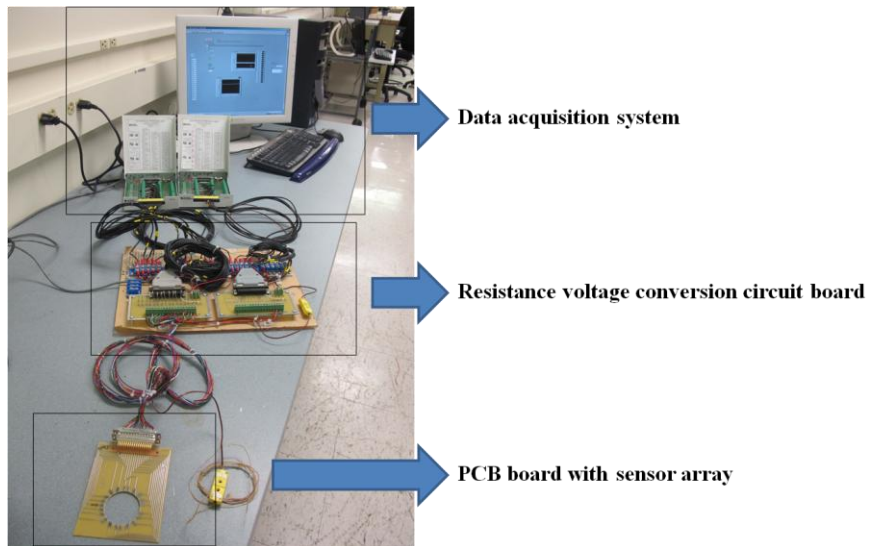
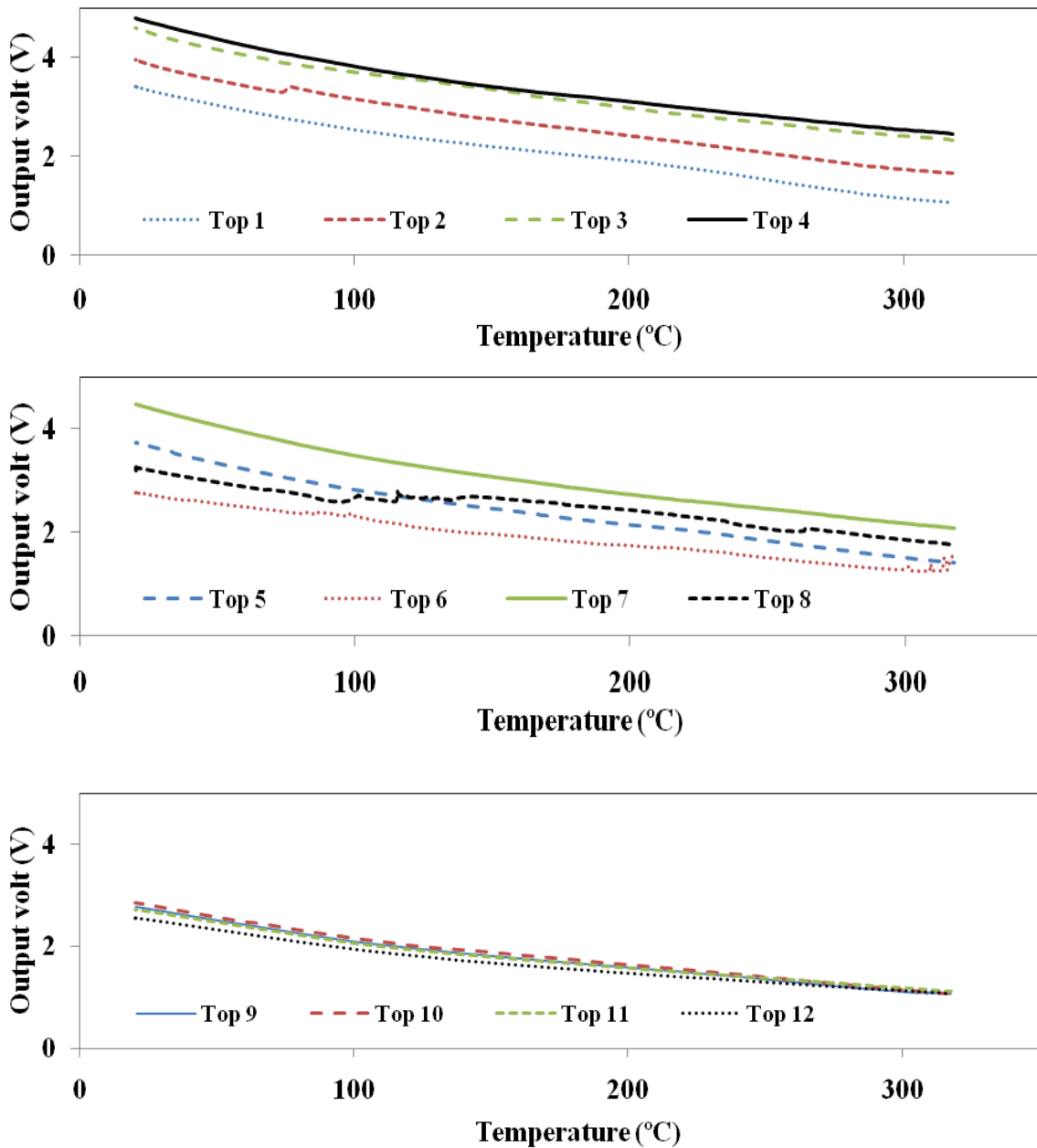
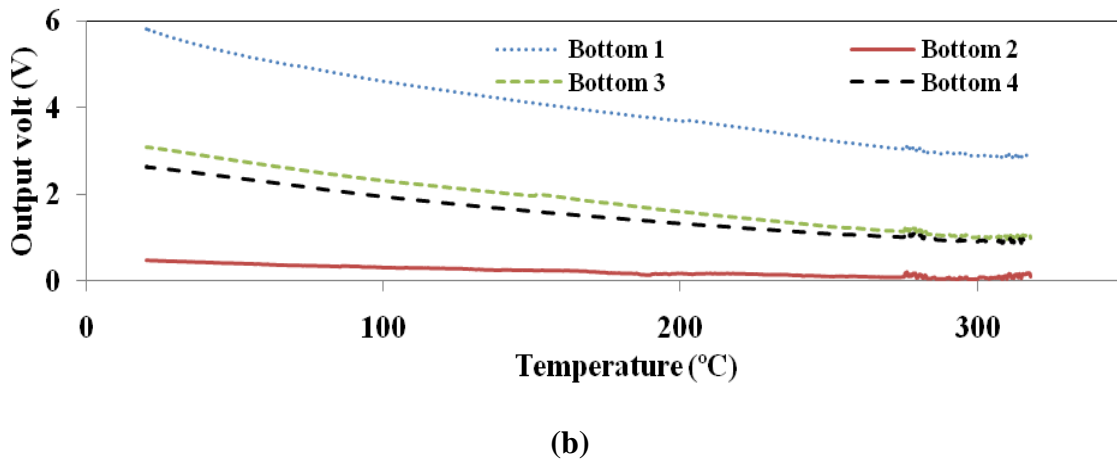
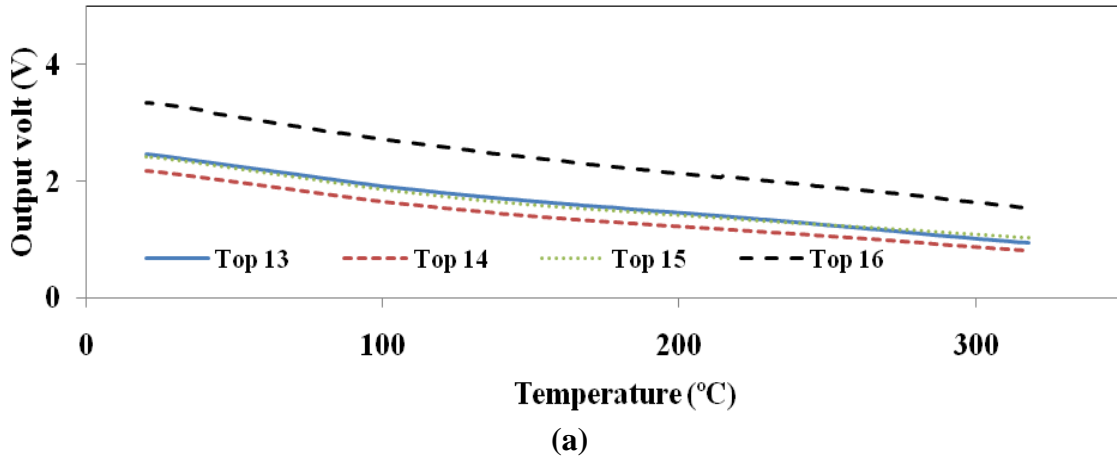


Figure 5.11 Picture of DAQ system for output voltage measurement from RTDs

Figure 5.12 (a) shows the results of measurement of output voltage. All 16 output voltages are divided into 4 plots and as shown up to about 300°C, smooth curves are obtained except 2 curves. From those curves, the relation of temperature and output voltage of each RTD can be obtained, which shows the possibility our PDC ceramics can be used as RTD and HFS sensor.





**Figure 5.12 Output voltage measurement results (a) from top RTDs, (b) from bottom RTDs**

Also, the Figure 5.12 (b) shows the output voltage from 4 RTDs of bottom side of quartz wafer. Four smooth curves are obtained as well. In the Figure 5.13, output voltage-temperature relation of total of 8 RTDs comprising 4 HFSs can be seen. Two RTDs of number 1 and 17 makes first HFS and same way for the other three HFS. In case of two HFSs which are combination of RTD 4, RTD 18 and RTD 16, RTD 20, the output voltage of bottom RTD is lower than that of top RTD. And the other two pairs of RTDs show that the output voltage of bottom is larger than those of top. After we know these

relations between output voltage and temperature of RTDs, it is possible to measure temperature difference between two RTDs, which can be used in calculation of the amount of heat flux.

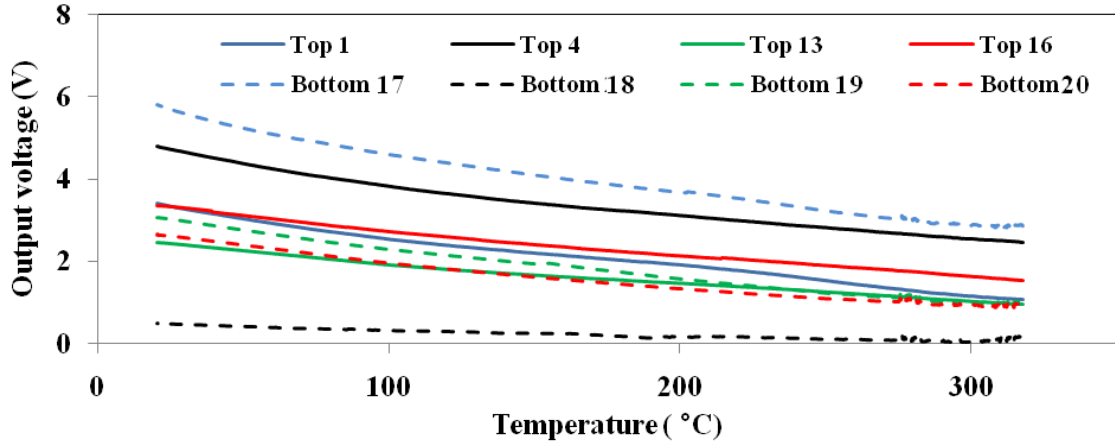
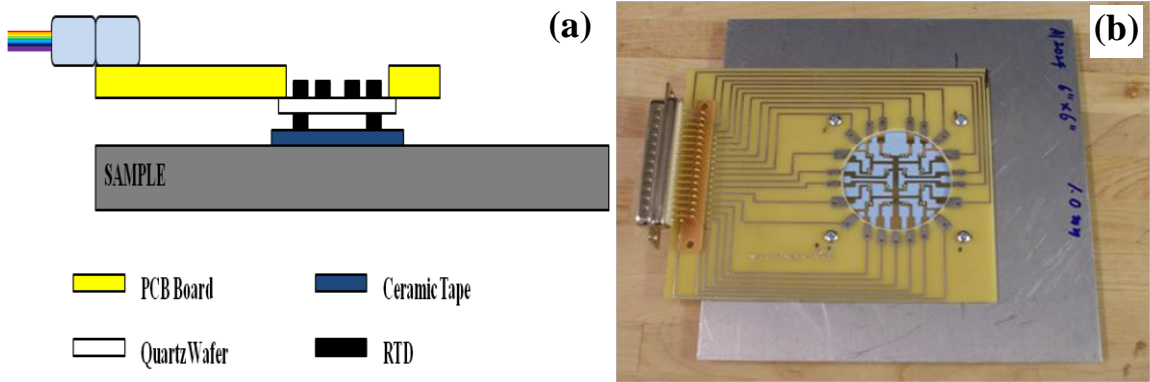


**Figure 5.13 Comparison of output voltage of RTDs at HFS locations**

### 5.3.3. Measurement of Temperature and Heat Flux of 4 HFSs

In this section, as a further work with HFS fabricated previous section 5.3.2, the procedures on obtaining the amount of heat flux for the 4 heat flux sensors on HFS array made in previous section are described. The measurement of output voltage of each RTD is used to find the amount of heat flux after normalization and additional measurement. Instead of hot plate, heat source from laser beam was employed and TiB<sub>2</sub> filled RTDs are used for this experiment. Experiment setup is different from what is shown in previous section. As shown in Figure 5.14 (a), which has the schematic of completed RTD array assembly, a thin aluminum plate (1.02mm) was used as laser target transferring heat to RTD array. And ceramic tape was placed between thin aluminum plate and RTD array to prevent electrical contact each other. Four volts and nuts are used to hold these parts:

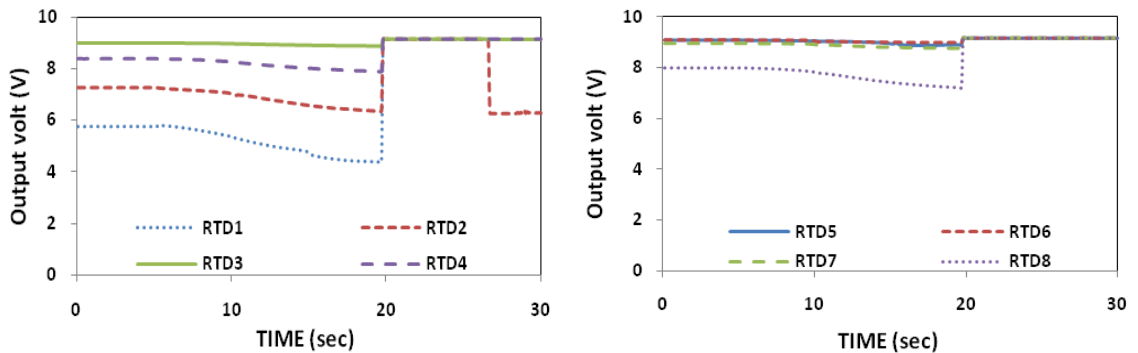
PCB board, RTD array, ceramic tape, thin aluminum plate. Figure 5.14 (b) shows actual picture of completed RTD array assembly.



**Figure 5.14 The schematic of completed RTD array assembly (a) cross-sectional view with constituents, (b) completed RTD array assembly**

### 5.3.3.1. Output voltage result of 20 RTDs

With same DAQ used in section 5.3.2, we can get output voltage results with respect to time for 20 RTD sensors shown in Figure 5.15 (a). And in Figure 5.15 (b), output voltages from 8 RTDs making up of 4 heat flux sensors are shown and the two curves with same color means that they are located on both sides of wafer at same position comprising a heat flux sensor.



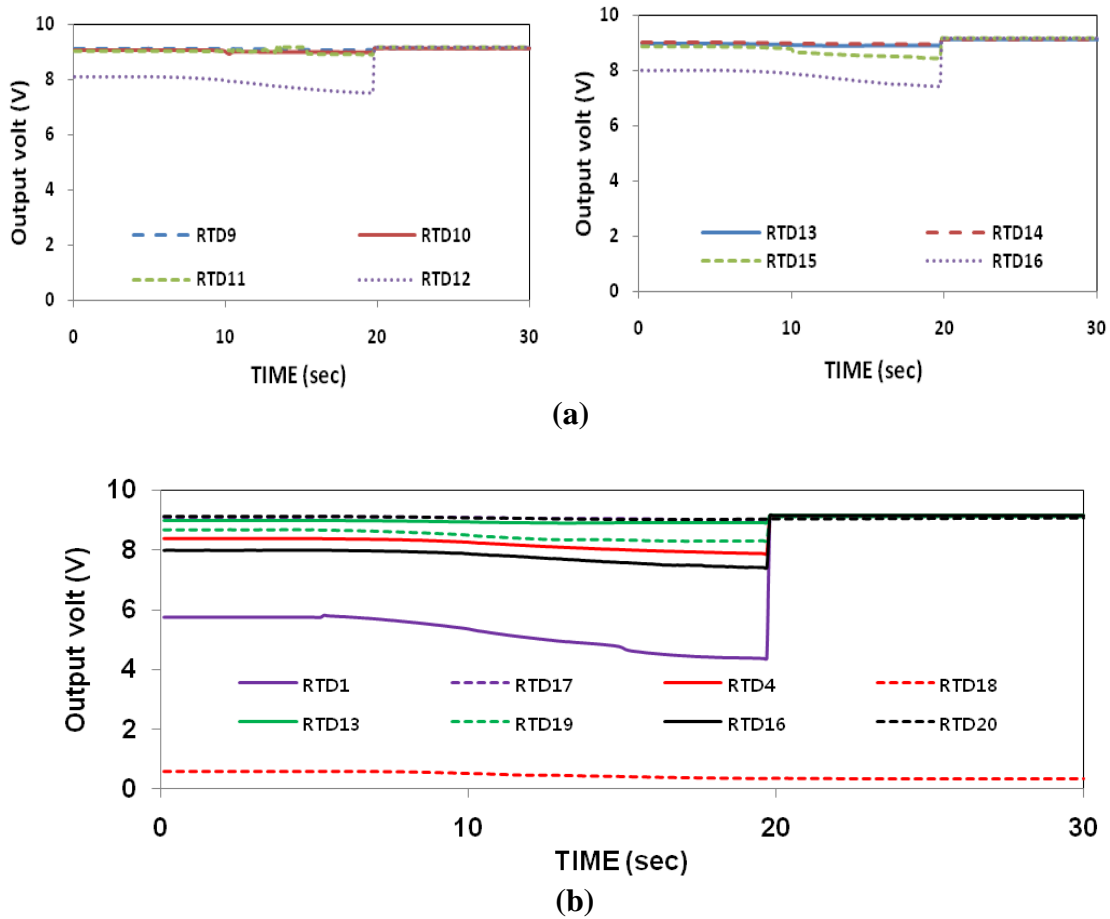


**Figure 5.15 Output voltage results of 20 RTDs (a) RTD 1~16 and (b) output voltage results of paired RTDs (1 and 17, 4 and 18, 13 and 18, 16 and 20) for heat flux measurements**

### 5.3.3.2. Normalization of output voltage

The output voltages from 20 RTDs on the wafer reveals different values at room temperature, which means resistance from 20 RTDs are not same but within some range. With about 9.16 V of excitation voltage, the range of output voltages was significantly different as shown in Figure 5.15. Therefore output voltage is normalized to compare one another more easily. The process for normalization is as follows.

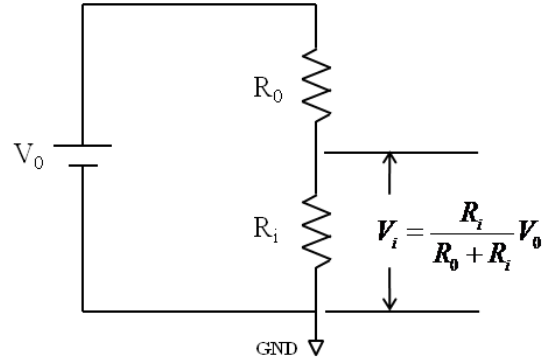


**Figure 5.16 Circuit diagram of voltage divider configuration**

In our voltage divider configuration, the equation for output voltage  $V_i$  can be derived using ohm's law as shown in Figure 5.16. And it is assumed that  $R_i = \alpha_i \rho$  where  $\alpha_i$  is constant for given sensor geometry and  $\rho$  is resistivity of RTD and dependant on temperature. Therefore the output voltage  $V_i$  can be expressed as;

$$V_i = \frac{\alpha_i \rho}{R_0 + \alpha_i \rho} V_0 \quad (5.3)$$

At room temperature, we have the known value  $V_i^o$  in that;

$$V_i^o = V_0 \frac{\alpha_i \rho_0}{R_0 + \alpha_i \rho_0} \quad (5.4)$$

where  $\rho_0$  is resistivity of RTD at room temperature and we can solve equation 5.4 to obtain

$$\alpha_i \rho_0 = \tilde{V}_i^o \frac{R_0}{1 - \tilde{V}_i^o} \quad \text{where} \quad \tilde{V}_i^o = \frac{V_i^o}{V_0} \quad \text{and} \quad \frac{1}{\alpha_i} = \rho_0 \frac{1 - \tilde{V}_i^o}{R_0 \tilde{V}_i^o} \quad (5.5)$$

Then after we solve equation 5.3 for  $\rho$  and substitute equation 5.5 into it, we get following result.

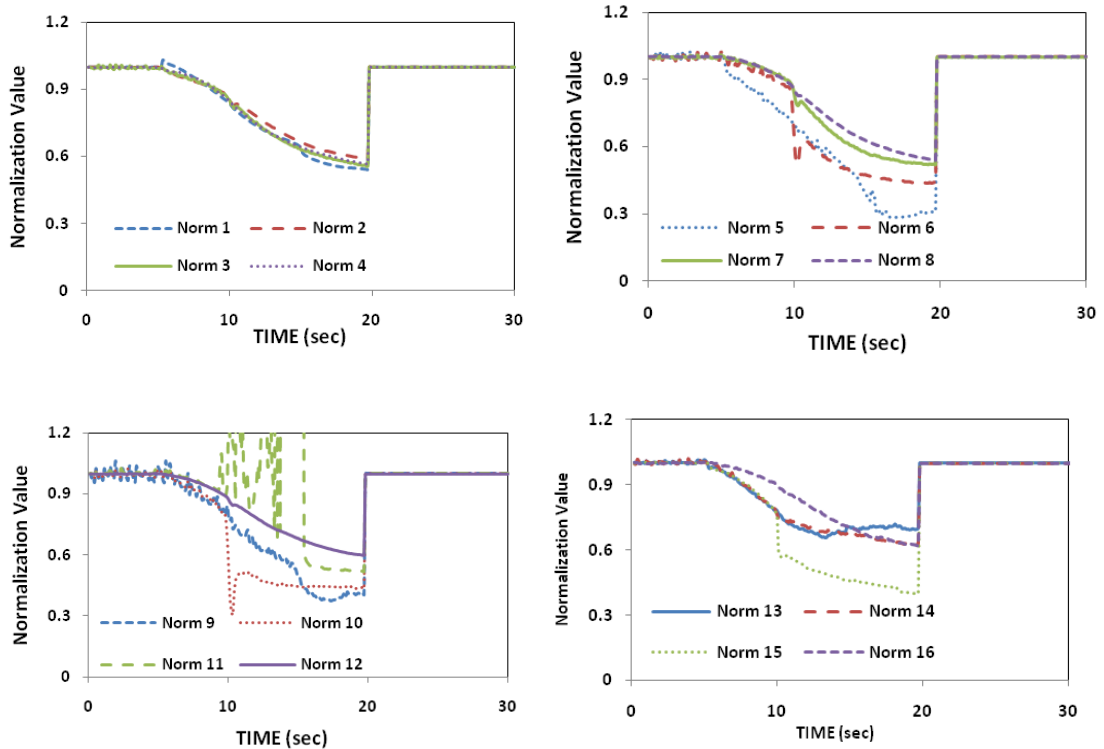
$$\rho = \frac{R_0 \tilde{V}_i}{\alpha_i (1 - \tilde{V}_i)} = \rho_0 \frac{R_0 \tilde{V}_i}{(1 - \tilde{V}_i)} \frac{(1 - \tilde{V}_i^0)}{R_0 \tilde{V}_i^0} = \rho_0 \frac{\tilde{V}_i}{\tilde{V}_i^0} \frac{V_0 - V_i^0}{V_0 - V_i} \quad \text{where } \tilde{V}_i = \frac{V_i}{V_0} \quad (5.6)$$

Finally the output voltage is normalized from equation 5.6 as following;

$$\frac{\rho}{\rho_0} = \frac{V_i}{V_i^0} \frac{V_0 - V_i^0}{V_0 - V_i} \quad (5.7)$$

Every curve for output voltage starts from 1 and as the output voltage decreases the normalized value  $\frac{\rho}{\rho_0}$  is also decreases. Therefore, using normalization equation 5.7,

the output voltages  $V_i$  are inserted into equation 5.7, and then we can get normalization results as shown in Figure 3.



(a)

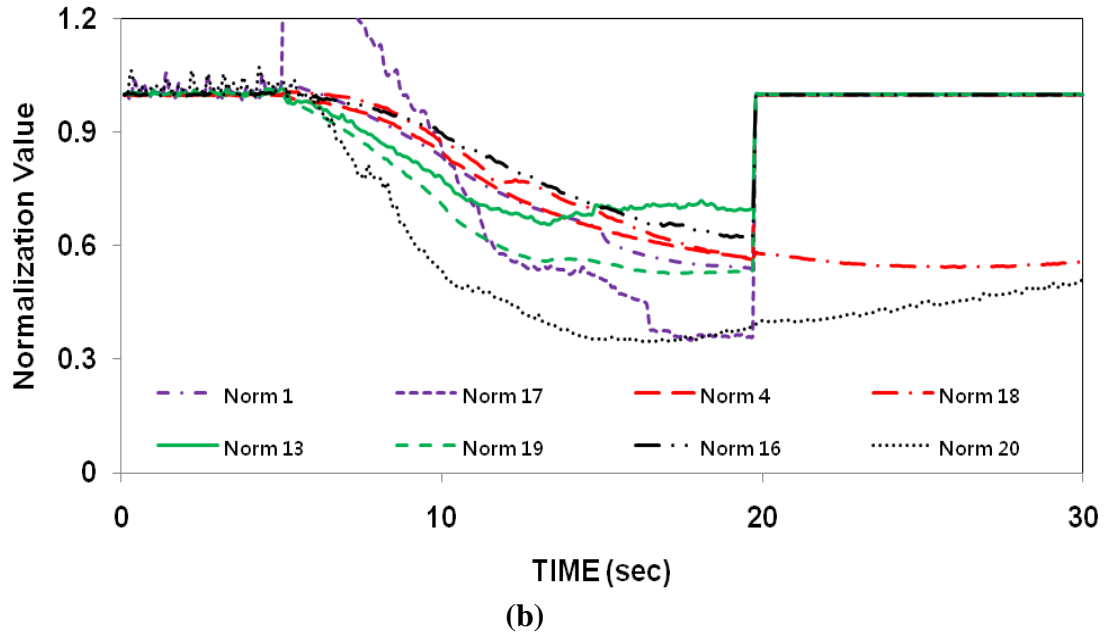
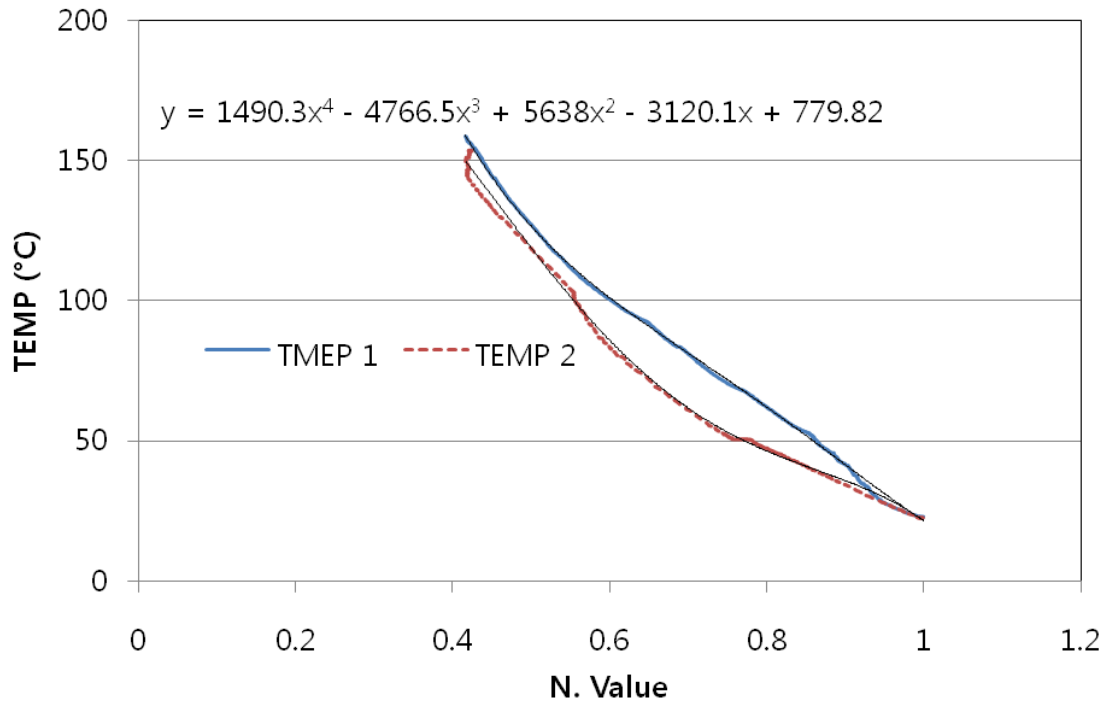


**Figure 5.17 Normalization results: (a) RTD 1~16 and (b) output voltage results of paired RTDs (1 and 17, 4 and 18, 13 and 18, 16 and 20) for heat flux measurements**

### 5.3.3.3. Calibration of temperature using normalization value

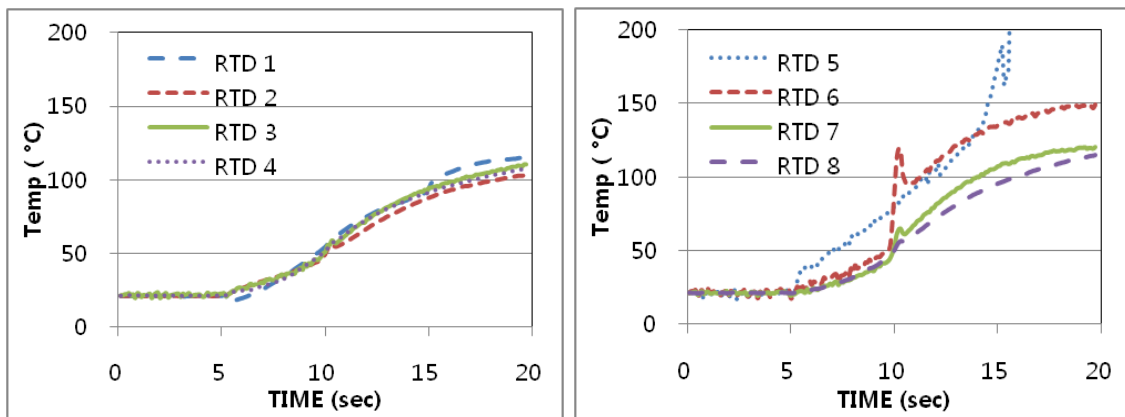
As next step, the relation between temperature and normalization value need to be obtained to use the temperature to calculate the heat flux. So additional experiment was performed. Two different  $TiB_2$  filled RTDs are selected from HFSA and two thermocouples are connected to right next to those two sensors individually. And after heating the HFSA to about 200C, the relation of temperatures and output voltages can be obtained. Since we want to know the relation between temperature and normalized value, those output voltages are converted to normalized value by using equation 5.7. Finally, the temperature-normalized value relation is obtained as shown in Figure 5.18. The equation can be estimated after fitting two curves in Figure 5.18 into one equation as shown below. The final estimated polynomial is

$$T(N) = 1490.3N^4 - 4766.5N^3 + 5638N^2 - 3120.1N + 779.82 \quad (5.8)$$



**Figure 5.18 Relationship between normalized value and temperature**

Figure 5.19 show the calibrated temperature results using equation 5.8. We can calculate the related temperature using equation 5.8.



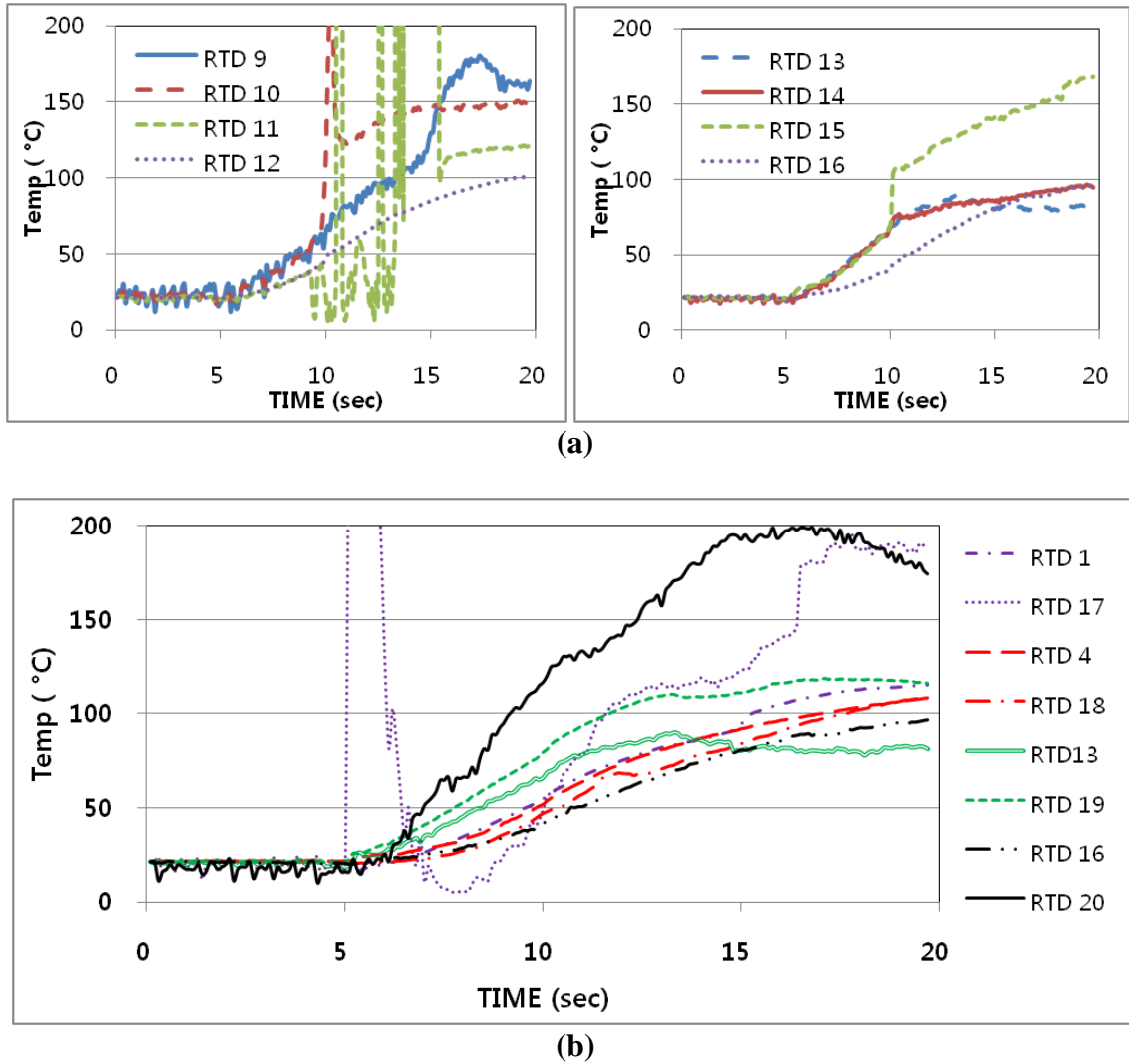


**Figure 5.19** Calibrated temperature of 20 RTDs (a) RTD 1~16 and (b) results of paired RTDs (1 and 17, 4 and 18, 13 and 18, 16 and 20 ) for heat flux measurements

#### 5.3.3.4. Heat flux calculation using calibrated temperature

Since the temperatures of each RTD are known as in Figure 5.19 and the heat flux amount of 4 heat flux sensors can be calculated using Fourier's Law with the assumptions ; One dimensional, steady state system and quartz is isotropic material.

$$Q = -k\nabla u = -k \frac{\Delta T}{\Delta x} \quad (5.9)$$

where the thermal conductivity  $K(T) = 0.000002T^2 + 0.0007T + 1.3722$ .(W/mK)

In equation 5.9, the temperature difference can be drawn from Figure 5.19 and the thickness of quartz wafer is 500um. Also since the conductivity of quartz wafer changes with the temperature, from the quartz wafer datasheet, the changing thermal conductivity is applied in the equation 5.9. And then the heat flux amount with time is obtained as shown in Figure 5.20. However, due to some electrical connection problem between wafer and DAQ system, heat flux value for RTD 1-17 are not acceptable therefore, the other 3 HFSs were presented in Figure 5.20.

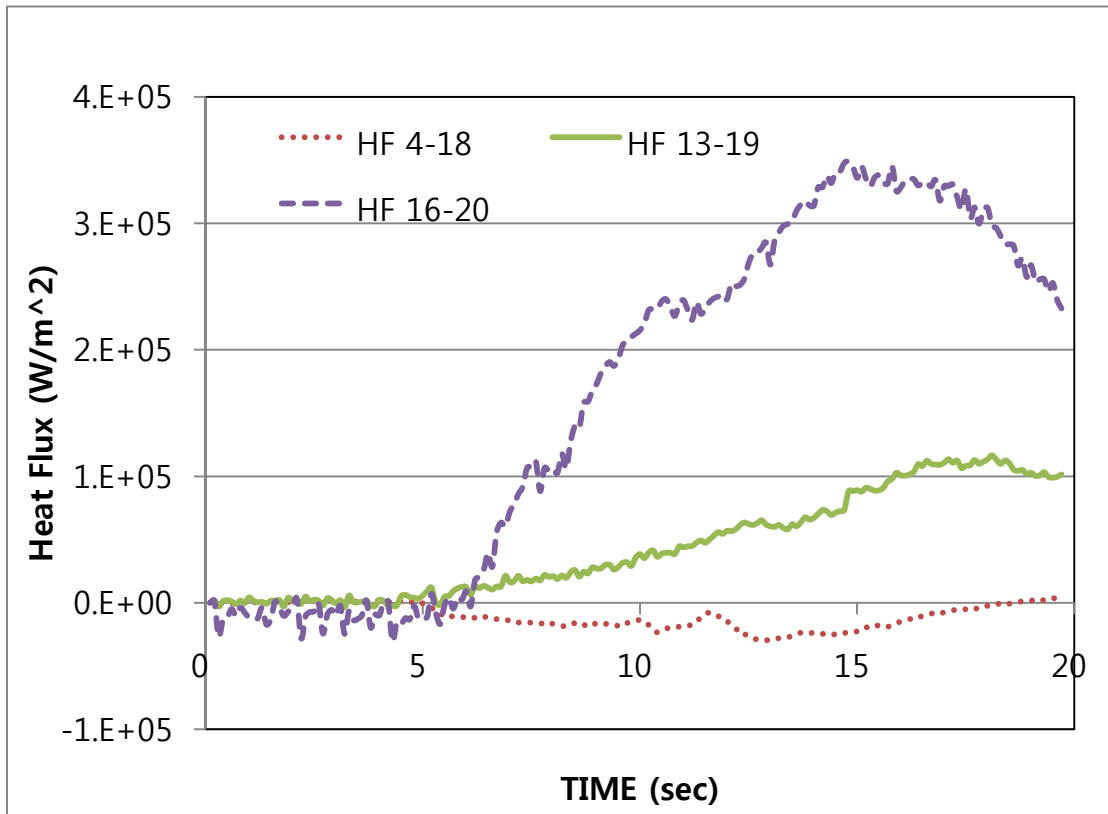


**Figure 5.20 Heat flux results using calibrated temperature**

## 5.4. Summary and Conclusion

From our free standing PDC SiCN RTDs, it was possible to fabricate the prototype of HFS. As a middle thermal barrier, material of OMEGABOND was used. Half Wheatstone bridge circuit was employed in order to measure the output voltage caused by the resistance difference of two RTDs in Wheatstone bridge circuit. After 4 HFSs are tested, it was found that the output voltage increases with the rise of temperature of RTDs even though some significant amount of noise is detected. It seems that more delicate fabrication of HFS and electrical connection are required for better measurement. After calibration of output voltage to commercial HFS, it is possible that our HFS made by two free standing RTDs can be used as HFS.

When it comes to the HFS made by filler used RTDs, patterning of RTDs on both sides of quartz wafer was achieved successfully resulting in available HFS. The PCB board and voltage divider circuit were prepared and employed for the more convenient and precise measurement. The results revealed that with RTD made from  $TiB_2$  filler shows very acceptable smooth shape of curve without significant amount of noise in curve.

And also HFS array was attached to thin aluminum plate that is heated by laser beam as heat source. The output voltage values are normalized to compare RTDs easily and followed by obtaining the relation of temperature and normalization value. After knowing the relation, it is possible to calculate the amount of heat flux using Fourier's law.

## Chapter 6

### DISCUSSION AND FUTURE WORK

#### 6.1. Discussions

##### 6.1.1. Electric connections

Previous study on the measurement of the electrical property of PDC SiCN briefly mentioned the electrical connection between sensor and electrode. Haluschka et al [16] used silver suspension and Liew et al [21] used electrically conductive probes. Since that connection is very closely related to the accuracy of the RTD from the viewpoint of the sensor, it needs to be handled carefully. For our connection, many well known techniques for electrical interconnection between the RTD and electrode have been applied and investigated such as silver paste, high temperature conductive paste (Pyro-duct 597-C, Aremco Inc., USA), brazing, wire bonding, etc.

However, it was found that each method has a problem for our RTD sensor. With wire bonding, even though the gold wire has a very good property for the high temperature (up to about 1000°C), reliable contact with the electrode was difficult; also, when we mounted our sample on the wire bonding machine, it was not stable enough. For Brazing is a famous technique used to make a solid contact between ceramic material and an electrode. But our sensor was too small to use the brazing technique since heating up the brazing material to a very high temperature (usually more than 1000°C) caused our RTD to be heated up also, which may result in changes to the electrical property.

Furthermore, melted brazing material smears onto the whole RTD easily unless one takes intensive precautions.

With the high temperature conductive paste, it was able to get relatively reliable data compared to the previous two methods. But the problem with this method was the repeatability of the obtained data. Additional measurements showed that the resistance at room temperature also increased as shown in Figure 6.1. It seems that some sort of oxidation happens during heating up when one uses conductive paste.

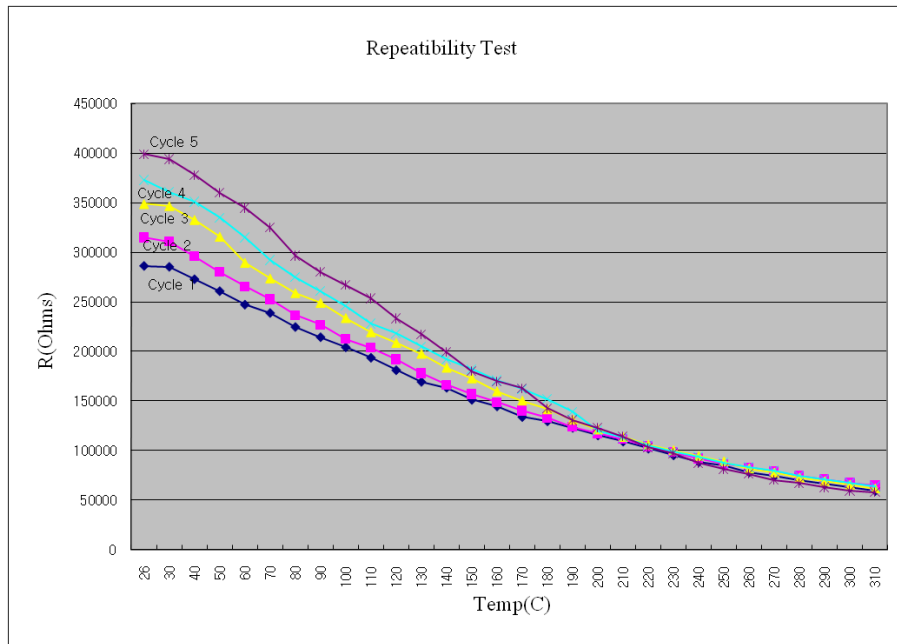


**Figure 6.1 Resistance rise at room temperature when using high temperature paste**

The most reliable electrical connection method is using silver paste or suspension unless our RTD is placed in a high temperature condition. Considering that the melting temperature of silver is 961°C, the choice of silver paste as an electrical connection method is not a good one. However, from our measurements, silver paste (SPI Conductive Silver Paste) showed the most reliable and repeatable data up to about 400°C.

Therefore, it seems that the choice of silver paste is quite suitable and preferable to platinum paste, which is more expensive than silver paste by the twice in the price

### 6.1.2. DAQ configuration for high resistance RTDs

In case of Al filled RTDs, The resistance values at room temperature for  $4 \times 4$  array have the range of  $300\text{K}\Omega \sim 20\text{M}\Omega$ . During the test of DAQ configuration before actual measurement, unexpected problem was faced. Whenever we change the resistance value of one RTD out of RTD array, those of adjacent RTDs were also changed, as shown in Figure 6.2 (a), which is called cross coupling effect. Obviously, accurate measurement was affected by that effect. As a reason, it can be thought that because of high impedance of RTD that makes the impedance of DAQ relatively low, most current flows not into the RTD but into the acquisition system as shown in Figure 6.2 (b).

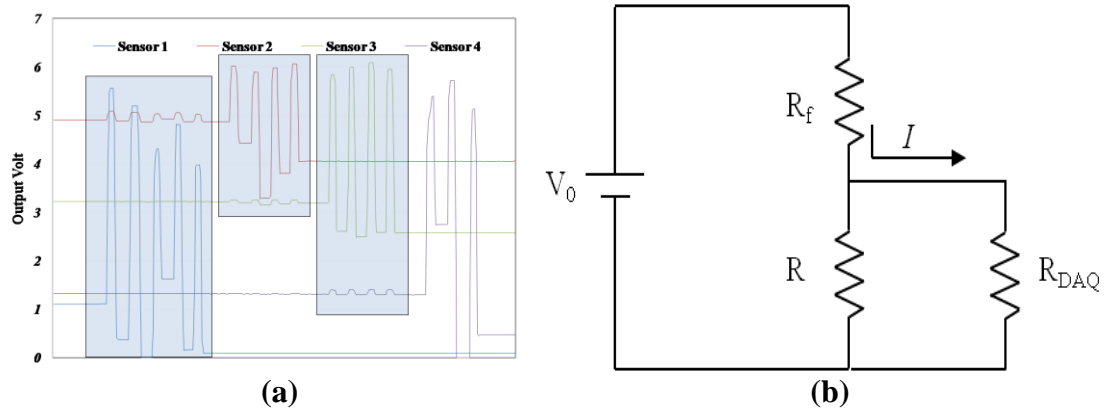


**Figure 6.2 Schematic of influence of RTD resistance on other RTDs**

To prevent this cross coupling effect, a voltage follower has been used shown in Figure 6.3 (a). It minimizes the impedance from DAQ equipment in remodeled circuit, which resulted in successful voltage measurement without any cross coupling effect.

Figure 6.3 (b) shows that there is no affection on adjacent RTD sensor even if we change the resistance of one RTD. The other difference is that unlike previous circuit, single power source is connected to all the voltage followers and all resistance sets are placed in parallel to share the power source.

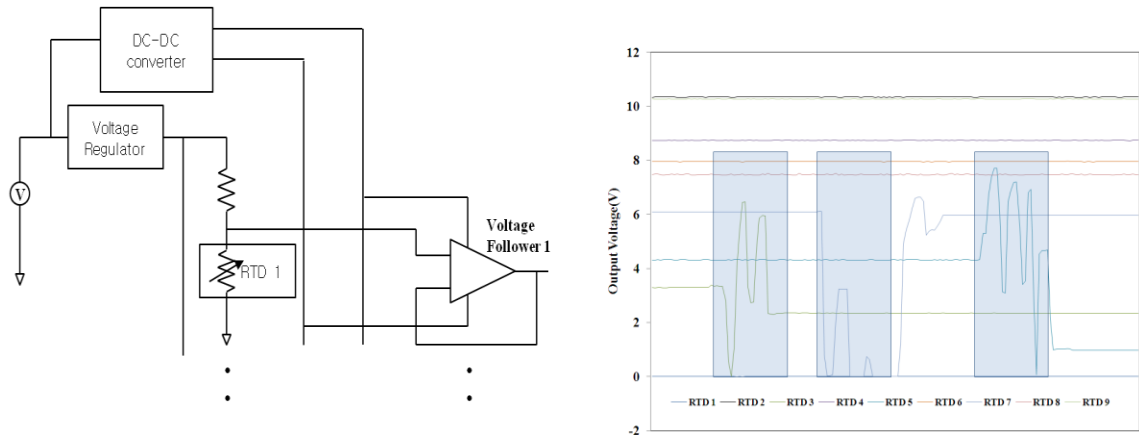


**Figure 6.3 No cross coupling effect after using the voltage follower**

## 6.2. Future works

As shown in discussion, due to conductive adhesive at high temperature, it was very hard to obtain consistent measurement result after iteration. Also in many measurements, there were significant noises in Figure of output voltage-temperature relation. Besides conductive adhesive, other elements in RTD packages, such as Au electrodes, can be affected by high temperature, which means they can be the reason of those noises. More robust electrical connection for high temperature and RTD sensor packaging needs to be accomplished for better measurement results.

From our investigation on electrical conductivity of PDC RTDs, our polysilazane based PDCs turned out to be promising material as RTD sensor. Also our filler used PDC RTDs can be outstanding elemental material for HFS application owing to not having shrinkage problem. Therefore, with further measurement, the calculated heat flux can be compared to the commercial HFS after applying commercial HFS in same experimental setup.

Actually the maximum temperature to measure the relation of temperature and resistance of our RTDs was limited to about 300 ~ 400°C due to the temperature restriction of equipment of data acquisition such as the PCB board, conductive paste. PCB board is able to endure only around 300°C since it is made from epoxy material and in case of conductive paste, it is necessary to find more accurate and advanced high temperature conductive paste for the electric connection between electrodes. Therefore after finding reliable RTD packaging, the measurement at higher temperature needs to be carried out.

When it comes to the electrical conductivity of our PDC RTDs, it is known that the final conductivity depends on the heat treatment time, temperature and atmosphere. However, it seems that the electrical charge transport phenomenon in polysilazane based PDC is not clearly revealed so far. It is thought that once the phenomenon in the atom scale is explained evidently, the electrical conductivity can be controlled more precisely and easily. Then our PDC RTD would become more reliable and confident temperature sensor.

With regard to the shrinkage rate of polysilazane used in this study, we have been consistent with the heating and cooling rate that is 2.5°C/min during entire heat treatment

process to make PDC material in the tube furnace. It is recommended that different heating and cooling rate during the process results in different shrinkage rate for the final product.

Based on other studies on PDC [67], [68], application of our polysilazane PDC can be expanded to other areas such as pressure sensor, coating material, etc. Because of PDC's outstanding properties at high temperature and cost-effectiveness, further studies for PDC on other application area can be continued further.

## REFERENCES

- [1]. Liew, L., W. Zhang, et al. (2000). "Ceramic MEMS." American Ceramic Society Bulletin,[80]: 25–30.
- [2]. P. Colombo, R. R., G. D. Soraru, H. -J. Kleebe (2010). "Polymer Derived Ceramics."
- [3]. Colombow, P. (2010). "Polymer-Derived Ceramics: 40 Years of Research and innovation in advaced ceramics." J. Am. Ceram. Soc. **93**(7): 1805-1837.
- [4]. Raj, R., R. Riedel, et al. (2001). "Introduction to the special topical issue on ultrahigh-temperature polymer-derived ceramics." Journal of the American Ceramic Society **84**(10): 2158-2159.
- [5]. R. Riedel, G. Passing, H. Schoenfelder, R.J. Brook, Synthesis of dense silicon-based ceramics at low temperatures, *Nature*. 355 (1992) 714-717.
- [6]. Shim, H., K. Kim, et al. (1997). "Anomalous photoluminescence from 3C-SiC grown on Si (111) by rapid thermal chemical vapor deposition." *Applied Physics Letters* 70: 1757.
- [7]. Chantrell, P.G. and Poppell, P. eds. *Inorganic Polymers for Ceramics*. Special Ceramics, ed. Poppell, P. 1965, Academic Press: New York.
- [8]. Verbeek, W., *Materials Derived from Homogeneous Mixtures of SiC and Si<sub>3</sub>N<sub>4</sub> and Method of their Production*, 1973, Bayer A G
- [9]. Yajima, S. et al, *SiC Sintered Bodies with Three Dimensional Polycarbosilane as Binder*. *Nature*, 1976. **264**(5583): 238-239
- [10]. Reidel, R. and Dressler, W., "Chemical Formation of Ceramics," *Ceramics International* **22** (1996) 233-239.
- [11]. Bahloul, D., M. Pereira, et al. (1997). "Pyrolysis chemistry of polysilazane precursors to silicon carbonitride." Journal of Materials Chemistry **7**(1): 109-116.
- [12]. Kleebe, H. J., D. Suttor, et al. (1998). "Decomposition-crystallization of polymer-derived Si-CN ceramics." Journal of the American Ceramic Society **81**(11): 2971-2977.

- [13]. C. Van Hoy, A. Barda, M. Griffith, J. W. Halloran, Microfabrication of ceramics by co-extrusion, *J. Amer. Cera. Soc.* 81 (1998) 152-158.
- [14]. Wang, S., J. Li, et al. (1999). "Fabrication of lead zirconate titanate microrods for 1–3 piezocomposites using hot isostatic pressing with silicon molds." *Journal of the American Ceramic Society* **82**(1): 213-215.
- [15]. C. Haluschka, H. Kleebe, R. Franke, R. Riedel, Silicon carbonitride ceramics derived from polysilazanes: Part I. Investigation of compositional and structural properties, *J. Euro. Cer. Soc.* 20 (2000) 1355-1364.
- [16]. C. Haluschka, C. Engel, R. Riedel, Silicon carbonitride ceramics derived from polysilazanes. Part II. Investigation of electrical properties, *J. Euro. Cera. Soc.* 20 (2000) 1365-1374.
- [17]. X. Zhang, X. Jiang and C. Sun, Microstereolithography of polymeric and ceramic microstructures, *Sens. Actuators. A-Phys.* 77 (1999) 149–156.
- [18]. L. A. Liew, W. Zhang, V. M. Bright, L. An, M. L. Dunn, R. Raj, Fabrication of SiCN ceramic MEMS using injectable polymer-precursor technique, *Sens. Actuators. A-Phys.* 89 (2001). 64-70.
- [19]. Z. Y. Liu, N. H. Loh, S. B. Tor, K. A. Khor, Y. Murakoshi, R. Maeda, T. Shimizu, Micro-powder injection molding, *J. Mater. Proc. Tech.* 127 (2002) 165-168.
- [20]. L. A. Liew, Y. Liu, R. Luo, T. Cross, L. An, V.M. Bright, M.L. Dunn, J.W. Daily, R. Raj, Fabrication of SiCN MEMS by photopolymerization of pre-ceramic polymer, *Sens. Actuators. A-Phys.* 95 (2002) 120–134.
- [21]. L. A. Liew, V. M. Bright, M. L. Dunn, J. W. Daily, R. Raj, R. A. Saravanan, Processing and characterization of silicon carbon-nitride ceramics: Application of electrical properties towards MEMS thermal actuators, *Sens. Actuators. A-Phys.* 103 (2003) 171-181.
- [22]. Wang, H., Z. Xie, et al. (2007). "Fabrication of SiCN MEMS by UV Lithography of Polysilazane" *Key Engineering Materials* **336**: 1477-1480.
- [23]. A. Leo, S. Andronenko, I. Stiharu, and R.B. Bhat, Characterization of thick and thin film SiCN for pressure sensing at high temperature, *Sensors*, 10 (2010) 1338-1354.
- [24]. Liu, Y., L. Liew, et al. (2002). "Application of microforging to SiCN MEMS fabrication\* 1." *Sensors and Actuators A: Physical* **95**(2-3): 143-151.

- [25]. Bright, V., R. Raj, et al. (2004). Injectable Ceramic Microcast Silicon Carbonitride (SiCN) Microelectromechanical System (MEMS) for Extreme Temperature Environments with Extension: Micro Packages for Nano-Devices.
- [26]. N. R. Nagaiah, J. S. Kapat, L. An, L. Chow. Novel Polymer Derived Ceramic-High Temperature Heat Flux Sensor for Gas Turbine Environment. *Journal of Physics: Conf. Series* 34 (2006) 458-463.
- [27]. Schulz, M., M. Börner, et al. (2004). "Cross linking behavior of preceramic polymers effected by UV-and synchrotron radiation." *Advanced Engineering Materials* 6(8): 676-680.
- [28]. Schulz, M., M. Börner, et al. (2005). "Polymer derived ceramic microparts from X-ray lithography—cross-linking behavior and process optimization." *Journal of the European Ceramic Society* 25(2-3): 199-204.
- [29]. Wang, H., I. Sung, et al. (2006). "Preparation of patterned SiC and SiCN microstructures." *Science in China Series E: Technological Sciences* 49(2): 164-171.
- [30]. Lee, D., K. Park, et al. (2007). "SiCN ceramic patterns fabricated by soft lithography techniques." *Sensors and Actuators A: Physical* 135(2): 895-901.
- [31]. Lee, H., T. Yoon, et al. (2008). "Nano-sized patterns derived from a SiCN preceramic polymer: Fabrication and their characterization." *Journal of Physics and Chemistry of Solids* 69(8): 2131-2136.
- [32]. Pham, T., D. Kim, et al. (2006). "Three-dimensional SiCN ceramic microstructures via nano-stereolithography of inorganic polymer photoresists." *Advanced Functional Materials* 16(9): 1235-1241.
- [33]. G. S. Chung, Characteristics of SiCN microstructures for harsh environment and high-power MEMS applications, *Microelec. J.* 38 (2007) 888-893.
- [34]. Gregory, O. and T. You (2005). "Ceramic temperature sensors for harsh environments." *IEEE sensors journal* 5(5): 833-838.
- [35]. Fanaei, T., N. Camiré, et al. (2008). "Electrical characterization of amorphous silicon carbide thin films deposited via polymeric source chemical vapor deposition." *Thin Solid Films* 516(12): 3755-3760.

- [36]. Hermann, A., P. Yao-Te Wang, et al. (2001). "Structure and electronic transport properties of Si-(B)-CN ceramics." *Journal of the American Ceramic Society* 84(10): 2260-2264.
- [37]. Wang, Y., L. Zhang, et al. (2008). "Effect of Thermal Initiator Concentration on the Electrical Behavior of Polymer-Derived Amorphous Silicon Carbonitrides." *Journal of the American Ceramic Society* 91(12): 3971-3975.
- [38]. Xu, W., J. Kapat, et al. (2005). The Potential of Electronic High Temperature Devices Based Upon Polymer Derived Ceramics, ASME.
- [39]. Cross, T., L. Liew, et al. (2002). Fabrication process for ultra high aspect ratio polysilazane-derived MEMS.
- [40]. Steinhart, J. and S. Hart (1968). Calibration curves for thermistors, Elsevier.
- [41]. Greil, P. (2005). "Active-filler-controlled pyrolysis of preceramic polymers." *Journal of the American Ceramic Society* **78**(4): 835-848.
- [42]. Greil, P. (1998). "Near net shape manufacturing of polymer derived ceramics." *Journal of the European Ceramic Society* **18**(13): 1905-1914.
- [43]. Xie, Z., S. Wang, et al. (2006). "Active Filler (Aluminum–Aluminum Nitride) Controlled Polycarbosilane Pyrolysis." *Journal of Inorganic and Organometallic Polymers and Materials* **16**(1): 69-81.
- [44]. Stackpoole, M. and R. Bordia (2002). Processing and Properties of Si<sub>3</sub>N<sub>4</sub> Matrix Composites, Coatings and Joints from Filled Pre-Ceramic Polymer Systems, Environmental Barrier Coatings Workshop, Nashville
- [45]. Zhu, Y., Z. Huang, et al. (2006). "Polymer-filler derived ceramics with low shrinkage using PCS/SiC/Al mixture." *physica status solidi (RRL)-Rapid Research Letters* **1**(2): R59-R61.
- [46]. Wang, Y., W. Fei, et al. (2006). "Oxidation/Corrosion of Polymer Derived SiAlCN Ceramics in Water Vapor." *Journal of the American Ceramic Society* **89**(3): 1079-1082.
- [47]. Dhamne, A., W. Xu, et al. (2005). "Polymer–Ceramic Conversion of Liquid Polyaluminasilazanes for SiAlCN Ceramics." *Journal of the American Ceramic Society* **88**(9): 2415-2419.

- [48]. Yu, S., R. Riman, et al. (2005). "Pyrolysis of titanium-metal-filled poly (siloxane) preceramic polymers: effect of atmosphere on pyrolysis product chemistry." Journal of the American Ceramic Society **78**(7): 1818-1824.
- [49]. Zhou, Y., S. Tu, et al. (2007). "Synthesis and Magnetic Properties of Polymer Derived Metal/SiCN Ceramic Composites." Key Engineering Materials **353 - 358**: 1485-1488.
- [50]. Park, S., D. Lee, et al. (2009). "Fabrication of three-dimensional SiC ceramic microstructures with near-zero shrinkage via dual crosslinking induced stereolithography." Chemical Communications **2009**(32): 4880-4882.
- [51]. Saha, A., S. Shah, et al. (2003). "Polymer-derived SiCN composites with magnetic properties." Journal of Materials Research **18**(11): 2549-2551.
- [52]. Pardo, D., G. Jabbour, et al. (2000). "Application of screen printing in the fabrication of organic light-emitting devices." Advanced Materials **12**(17): 1249-1252.
- [53]. Shaheen, S., R. Radspinner, et al. (2009). "Fabrication of bulk heterojunction plastic solar cells by screen printing." Applied Physics Letters **79**(18): 2996-2998.
- [54]. Winther-Jensen, B. and F. Krebs (2006). "High-conductivity large-area semi-transparent electrodes for polymer photovoltaics by silk screen printing and vapour-phase deposition." Solar Energy Materials and Solar Cells **90**(2): 123-132.
- [55]. NagataKenji, R. (1995). "A glucose sensor fabricated by the screen printing technique." Biosensors and Bioelectronics **10**(3-4): 261-267.
- [56]. Ismail, B., M. Abaab, et al. (2001). "Structural and electrical properties of ZnO films prepared by screen printing technique." Thin Solid Films **383**(1-2): 92-94.
- [57]. Schulz, M. (2009). "Polymer derived ceramics in MEMS/NEMS: a review on production processes and application." Advances in applied ceramics **108**(8): 454-460.
- [58]. T.G. Beckwith, R.D. Marangoni, and J.H. Lienhard (2007). "Mechanical Measurements" 6th ed. Pearson Prentice Hall, p638.
- [59]. Volklein, F. and E. Kessler (2002). Thermoelectric microsensor for heat flux measurement, IEEE.

- [60]. Hager, J., S. Simmons, et al. (1991). "Experimental performance of a heat flux microsensor." Journal of Engineering for Gas Turbines and Power **113**: 246.
- [61]. Childs, P. R. N., J. Greenwood, et al. (1999). "Heat flux measurement techniques." Proceedings of the Institution of Mechanical Engineers, Part C: Journal of Mechanical Engineering Science **213**(7): 655-677.
- [62]. Holmberg, D. and T. Diller (1995). "High-frequency heat flux sensor calibration and modeling." Journal of Fluids Engineering **117**: 659.
- [63]. Oh, S., K. Lee, et al. (2001). "Micro heat flux sensor using copper electroplating." Journal of Micromechanics and Microengineering **11**: 221-225.
- [64]. Oh, S., S. Lee, et al. (2006). "Bulk-micromachined circular foil type micro heat-flux sensor." Sensors and Actuators A: Physical **132**(2): 581-586.
- [65]. Snyder, G., J. Lim, et al. (2003). "Thermoelectric microdevice fabricated by a MEMS-like electrochemical process." nature materials **2**(8): 528-531.
- [66]. Wrbanek, J., G. Fralick, et al. (2004). Development of thin film ceramic thermocouples for high temperature environments, cosponsored by the AIAA, ASME, SAE, and ASEE Fort Lauderdale, Florida
- [67]. Leo, A., S. Andronenko, et al. (2010). "Characterization of Thick and Thin Film SiCN for Pressure Sensing at High Temperatures." Sensors **10**(2): 1338-1354.
- [68]. Jedrzejowski, P., J. Cizek, et al. (2004). "Mechanical and optical properties of hard SiCN coatings prepared by PECVD." Thin Solid Films **447**: 201-207.

## **VITA**

SUNGHOON JUNG was born on JULY 25, 1974 at Yeo-Su, Jeon-Nam in Korea. He graduated from Yeo-Su high school in 1993. He studied at Korea Military Academy in Seoul, Korea where he received his B.S. degree with the major of applied physics. After graduating, he served 3 years in Korea Army including a platoon leader in Infantry Company for 12 months. He studied M.S. degree in the Department of Mechanical and Aerospace Engineering at Naval Postgraduate School from 2000 to 2002. After five years' serving in Korea Army including company commander for 18 month, he was selected again for his Ph.D. program. He started his Ph.D. degree at the Department of Mechanical and Aerospace Engineering in University of Missouri-Columbia in 2007 and received a Ph.D. on December 2011.